Master's thesis

NTNU
Norwegian University of Science and Technology
Faculty of Natural Sciences
Department of Physics

Asbjørn Torsvik Krüger

Electrohydrodynamics and particle sintering as methods for production of microporous capsules

Master's thesis in MSPHYS
Supervisor: Jon Otto Fossum
July 2019

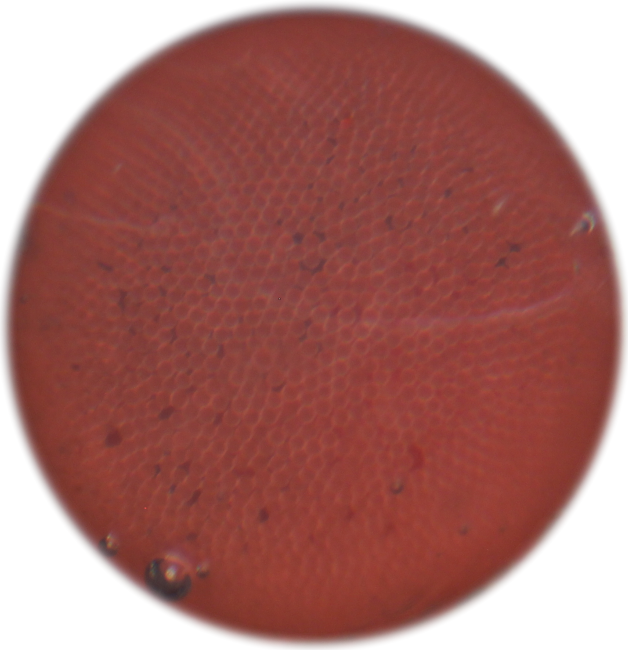

NTNU
Norwegian University of
Science and Technology

Asbjørn Torsvik Krüger

Electrohydrodynamics and particle sintering as methods for production of microporous capsules

Master's thesis in MSPHYS
Supervisor: Jon Otto Fossum
July 2019

Norwegian University of Science and Technology
Faculty of Natural Sciences
Department of Physics

NTNU
Norwegian University of
Science and Technology

Abstract

Capsules of all sizes are used in engineering, scientific and pharmaceutical purposes. They can function as sealed or porous compartments in order to regulate material flow. In this thesis, the fabrication of porous spherical capsules with diameters ranging from 0.4 mm to 1.2 mm is investigated. Soft capsules were fabricated by making silicone oil droplets in castor oil, and covering the droplets with 40 µm polystyrene beads utilising electrohydrodynamic effects. The beads on the droplets were then sintered by heating to the glass transition temperature of polystyrene, successfully fabricating rigid porous capsules encapsulating the silicone oil droplet. The capsules were analysed in micropipette aspiration experiments, where the capsules could be emptied by sucking the encapsulated oil droplet out. The capsules were found to be remarkably rigid. Emptied capsules were analysed in a scanning electron microscope, showing sintering necks with cross sections between 7 µm and 19 µm.

Sammendrag

Kapsler av alle størrelser brukes i både vitenskapelige og medisinske områder. De kan være enten forseglede eller porøse for å regulere materialstrøm. I denne oppgaven blir konstruksjonen av porøse sfæriske kapsler undersøkt, med diametere mellom 0.4 mm til 1.2 mm. Myke kapsler ble lagd ved å lage dråper av silikonolje i kastorolje, for så å dekke dem med 40 µm polystyrenkuler ved hjelp av elektrohydrodynamikk. Kulene på dråpene ble sintret ved å varme opp til glasstransisjonstemperaturen til polystyren, slik at harde porøse kapsler ble lagd. Kapslene ble analysert i eksperimenter med mikropipetteaspirasjon, der kapslene kunne bli tømt ved å suge ut de innkapslede dråpene. Kapslene var overraskende sterke. Tomme kapsler ble analysert i elektronmikroskop, der det ble funnet at de sintrede nakkene mellom polystyrenkulene var mellom 7 µm og 19 µm brede.

Acknowledgements

Although this thesis carries my name, this masters project was a team effort. I would like to thank my supervisor, Jon Otto Fossum, for providing me with this project, and for creating a framework of people at the Complex Materials group at NTNU. For the lab setup, I'm grateful to Ole Tore Buset for helping me get the experimental setup working. I would also like to thank Kristoffer William Bø Hunvik for help on the problems involving wax. Further, I extend my thanks to Paul Dommersnes and Kristofer Paso for answers to questions regarding the theory. Thank you to Per Magnus Walmsness on helping on getting figure 2.4 to look nice, Gert Kluge for proofreading this thesis, Yves Meheust for helping on the fluid flow imaging in figure 3.4, and Geir Helgesen for performing the calorimetry measurements on the polyethylene beads at IFE. I also find it fitting to thank Alexander Mikkelsen, whom I've never met or been in contact with, but whose master thesis, doctoral thesis, and several papers have been very helpful. A special thanks to Gregory Beaune and Jaakko Timonen for letting me come to Aalto University, Finland, and for helping out in performing the measurements on the capsules. Also thank you to Osvaldo Neto for helping out in Finland.

Finally, I would like to extend my deepest gratitude to the one who made all this possible: Ville Valdemar Liljeström. For assisting in every leg of this journey, and without whom this thesis would never reach the state that it is in now. Thank you.

I also want to thank my family. Even though I have the feeling that you didn't understand much, I thank you all for asking, listening, supporting, and for being there for me during my entire life.

And as this thesis marks the end of my five years as a student here in Trondheim, I would like to thank every single person who has smiled to me, talked to me, shared experiences with me, and let me into their lives, either for a second or for five years. It's people like you who make life interesting.

Contents

List of Figures

Chapter 1

Introduction

Soft matter physics and self-assembly are very much hot topics in science at the moment. Soft matter physics is the physics of materials held together by intermolecular forces of various origins, excluding metallic, covalent, and ionic bonds. The field was pioneered by Pierre-Gilles de Gennes, who was awarded the Nobel prize in physics for his contributions in 1991 [1]. Examples of soft matter include polymers, surfactants, liquid crystals, colloidal suspensions, aerosols, emulsions, and foams [2]. The term "self-assembly" could be self-explanatory, but since every natural formations by nature is "self-assembled", a more specific definition is needed. The definitions vary, one being that "self-assembly refers to the spontaneous formation of organised structures through a stochastic process that involves pre-existing components, is reversible, and can be controlled by proper design of the components, the environment, and the driving force" [3]. Both soft matter physics and self-assembly are exciting tools, as they exploit some exotic properties in nature, making the research on the topics very diverse, and the results useful for a wide range of technologies important to daily life [4].

Capsules of all kinds are an integral part of our lives, finding their way into many fields, such as chemical engineering, materials science, and pharmaceutical and life science [5]. To fabricate capsules on a micrometre length scale, one can no longer build them part by part, as the building blocks are too small, and the forces between them too strong. This is where self-assembly comes into the picture. By exploiting the physics of forces between particles in the micrometre world, one can build the capsules by using nature as both the architect and construction worker.

Such capsules can be used in a wide range of applications. Just as any other capsules they can encapsulate materials, for example for drug delivery [6]. The

capsules can also be covered in functionalised materials, such as magnets or environment responsive polymers [7]. As capsules with different properties on different sides can be tailored specifically for a cause, the potential possibilities could be close to limitless [8].

Much work has already been done on making capsules, with numerous scientific papers written on the fabrication of capsules in liquids, using techniques such as double emulsions with a UV curable resin [9, 10], particle assembly with van der Waals forces [11] and glass transition [12], gels [13], and chemical reactions [14, 15]. A common denominator for these publications is that the diameters of the capsules are smaller than approximately 200 µm for capsules fabricated with particle assembly, while double emulsions allow for larger diameters. Many are also completely covered, not allowing fluid flow through the shells, which can result in bursting [16]. One reason for the small sizes for particle assembled capsules is that most of the fabrication methods rely on Brownian motion for the particles to assemble on the surfaces of a droplet, which is only achievable for small length scales if the layer is to assemble during a normal workday. The mean time to diffuse over a distance increases with the square of the distance, and thus what only takes a minute to happen across a micrometre, takes well over a year across a millimetre. Therefore, some form of external influence has to be applied to the system.

This external influence is, in the case of this thesis, an electric field, which is applied across a sample cell, allowing the assembly of the shell to happen in minutes. In the presence of external influences, we now speak of *dynamic* self-assembly [3]. But the definition of self-assembly stated that the process had to be reversible, which for a product like a capsule sounds like a bad idea, as we do not want the capsules to dissolve by themselves at arbitrary times. Therefore, after the particles have assembled on the surface of the droplet, heat is applied to the system, such that the particles can be fused together, forming a rigid, non-reversible, shell. Then the capsules can encapsulate their contents, and be destroyed, releasing what is inside them when we want them to, either by acoustic vibrations, chemical dissolving, external fields, melting, or more [17]. By sintering small microbeads at the glass transition temperature instead of melting them completely, the capsules allow fluid flow through them, without deforming or bursting, and still keeping hold of the contents inside, as long as they are larger than the biggest hole in the capsule, which for perfect hexagonal packing is approximately 0.1547 times the capsule bead size.

Here in this thesis, a way of fabricating millimetre-sized capsules with dynamic self-assembly of particles is presented, using electrohydrodynamics to propel 40 µm polystyrene microparticles from inside a droplet to the surface, where a shell is assembled, and thereafter sintered, utilising the glass transition of polystyrene. The sintered capsules could then be analysed with optical mi-

croscope, emptied for oil and crushed, or dried and analysed with a scanning electron microscope.

The thesis is divided into six chapters, including this one. In the following chapters, the theory behind the capsule fabrication process will be introduced, then the methods used will be explained, followed by a presentation of the results, a chapter for discussing the methods and results, and finally a conclusion with a summery and suggestions for further work.

Chapter 2

Theory

Our universe obliges to some fundamental rules. Here, we will look at some phenomena and models that will be important for interpreting the results of this work. The models differ, as the science has improved through the years, with varying grade of approximations, assumptions, and accuracy.

2.1 The micrometre length scale

The length scales of the universe, and all the matter that it contains, are widely varying. From the diameter of an atomic nucleus (10^{-15} m), to the diameter of the observable universe (10^{27} m), different forces dominate the different length scales. For this thesis, the length scales that will be examined is roughly a micrometre to a millimetre (10^{-6} m to 10^{-3} m). Most of the physics will happen in a sample cell, making the forces interacting between the fluids and solids the most prominent.

The dimensionless Reynolds number

$$\mathrm{Re} = \frac{\rho u L}{\mu} = \frac{uL}{\nu} \tag{2.1}$$

predicts how the flow is going to be, with ρ being the fluid density, u being the characteristic velocity, L the characteristic length, μ the dynamic viscosity (units Pa s), and $\nu = \frac{\mu}{\rho}$ the kinematic viscosity (units $\mathrm{m^2\,s^{-1}}$) [18].

For a droplet with diameter of a millimetre, moving at a velocity of a millimetre per second through a fluid with a kinematic viscosity of $0.001\,\mathrm{m^2\,s^{-1}}$ (1000 cSt), which is the system that is to be examined in this thesis, the Reynolds number

is on the order of $\mathrm{Re} \approx 10^{-3} \ll 1$. With such a low Reynolds number, we are well into what is called the laminar regime, where inertial effects are negligible.

The intermolecular forces, such as the van der Waals forces and native electrostatic forces (as opposed to those from applying an external electric field, as will performed later) do not act above ranges of roughly 100 nm, and thus are only of importance when objects in the sample cell are in contact with each other. For any other situation, the intermolecular forces are negligible [19].

We will here in this thesis encounter several quantities that scale with the length with different powers. Examples are capillary forces (L^1), drag from fluid flow (L^1), diffusion (L^2), and gravity (L^3). As the quantities scale with different powers of the length, different particle sizes will not behave the same way in the sample cell, so while a result is found to be true for one particle size, changing the particle size can lead to a different result, even though the particle size is only halved or doubled.

2.2 Surface tension

The constituents of a liquid, the molecules, are in a condensed state where the molecules attract each other. For a liquid, this attraction is stronger than the thermal agitation [20]. While molecules completely covered by other molecules (i.e. inside the liquid) have equal attraction from all sides, molecules at the surface only get attracted by the molecules beneath (assuming vacuum, air, or another medium with negligible interaction on the other side), as shown in figure 2.1.

The cohesion energy per molecule, which for a covered molecule would be U, is for a molecule at the surface only $U/2$. This energy discrepancy is the source of the surface tension γ, which is on the order of $\gamma \simeq U/(2a^2)$, where a is the molecule size, and thus a^2 is the molecule area. The stronger the molecule interactions, the stronger the surface tension. I.e. one must do more work to overcome the molecule interactions to change the surface area of the liquid [3]. The surface tension is measured in joule per square metre ($\mathrm{J\,m^{-2}}$), or equivalently newton per metre ($\mathrm{N\,m^{-1}}$). The surface tension for many liquids, like oils and water, is typically in the range $10\,\mathrm{mN\,m^{-1}}$ to $100\,\mathrm{mN\,m^{-1}}$ at room temperature [21].

A more formal definition of γ is that the surface tension is the derivative of the Helmholtz free energy $\mathcal{F}$ at the interface, with respect to the interface area $\mathcal{A}$, with constant number of particles N, volume V and temperature T [20,

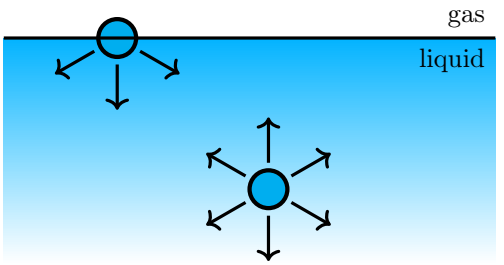

Figure 2.1: A sketch of the origin of the surface tension, showing the attractive interactions of two molecules: one completely inside the liquid, and the other at the surface. Here, the interaction between a fluid molecule and gas molecule is considered negligible. Figure inspired from [20].

22]:

$$\gamma = \left(\frac{\partial \mathcal{F}}{\partial \mathcal{A}}\right)_{N,V,T}. \tag{2.2}$$

When droplets of two non-miscible liquids A and B are in a host medium C, three stable systems can form, depending on the interfacial tensions:

(a) the droplets are separated by the host medium, occurring if

$$\gamma_{\mathrm{AB}} > \gamma_{\mathrm{AC}} + \gamma_{\mathrm{BC}}, \tag{2.3}$$

(b) one liquid can completely engulf the other, occurring if

$$\gamma_{\mathrm{AC}} > \gamma_{\mathrm{BC}} + \gamma_{\mathrm{AB}} \quad \text{or} \quad \gamma_{\mathrm{BC}} > \gamma_{\mathrm{AC}} + \gamma_{\mathrm{AB}}, \tag{2.4}$$

where B covers A in the first case, and A covers B in the second case, or

(c) the droplets form a partial engulfed pair, if none of the inequalities 2.3 and 2.4 are satisfied [23]. These three cases are shown in figures 2.2a, 2.2b, and 2.2c, respectively.

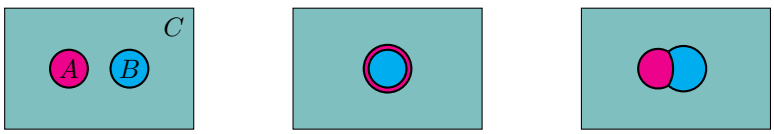

(a) (b) (c)

Figure 2.2: The three possible conditions for three non-miscible liquids A, B, and C. The condition depends on the interfacial tensions.

Such a system of three liquids is described by the contact angle θ_E, which is the angle between the tangents of the fluids A and B at the contact point of A, B, and C, if it exists. The angle θ_E is defined by Young's relation [20]

$$\gamma_{AC} \cos\theta_E = \gamma_{BC} - \gamma_{AB}, \tag{2.5}$$

and can have any value between 0° and 180°. Equation 2.5 is derived from the balancing of the x-components of the interfacial forces from the surface tensions appearing in a three-phase solution, as shown in figure 2.3. If B has an infinitely large surface, like for a droplet A on a solid surface, and C being air, we have a droplet on the surface, and then a contact angle 0° represents total wetting (liquid A forming a thin film on B) and 180° represents a hydrophobic surface B, as A forms an undeformed spherical droplet, resting on B. For any other value in between, the droplet is in a partially wetting situation, as shown in figure 2.3.

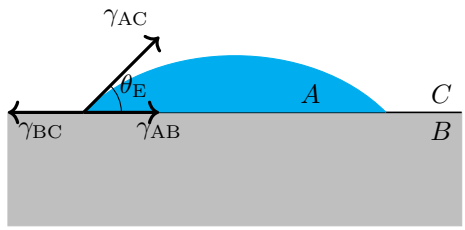

Figure 2.3: A sketch of a droplet of fluid A on a large flat solid surface B, in a host medium C. The arrows show the direction of the interfacial forces, with the contact angle θ_E defined by equation 2.5. Figure inspired from [24].

2.3 The dielectric sphere model

A droplet immersed in a liquid affects the E-field around it, as the droplet becomes polarised. To calculate the polarisation of droplets of an insulating oil when embedded in another insulating host fluid, we first start with finding the E-field for a solid dielectric sphere in a dielectric medium. This derivation is inspired from David J. Griffith's "*Introduction to electrodynamics*" [25].

When the applied E-field is homogeneous, the potential V is related to the electric field $\mathbf{E}$ by the equation

$$\mathbf{E} = -\boldsymbol{\nabla} V. \tag{2.6}$$

Gauss' law, also known as Maxwell's first law, states the relation between the E-field, electric charge distribution ρ, and vacuum permittivity ϵ_0, as

$$\boldsymbol{\nabla} \cdot \mathbf{E} = \frac{\rho}{\epsilon_0}. \tag{2.7}$$

As there are no free charges on the surface of a dielectric sphere ($\rho = 0$), we get that

$$\nabla^2 V = 0, \tag{2.8}$$

which is known as Laplace's equation.

With boundary conditions given by continuity at the boundaries, for a sphere with radius R and applied external electric field $\mathbf{E}_0$, the boundary condition equations for the system become

$$V_{\text{in}} = V_{\text{out}}, \qquad \text{at } r = R, \tag{2.9a}$$

$$\epsilon_{\text{in}} \frac{\partial V_{\text{in}}}{\partial r} = \epsilon_{\text{out}} \frac{\partial V_{\text{out}}}{\partial r}, \qquad \text{at } r = R, \tag{2.9b}$$

$$V_{\text{out}} \to -|\mathbf{E}_0| r \cos\theta, \qquad \text{for } r \gg R, \tag{2.9c}$$

where r and θ are the polar coordinates, with r being the distance from the centre, and θ being the angle between the position vector and the direction of the electric field $\mathbf{E}_0$.

We define $\epsilon_{\text{r}} = \epsilon_{\text{in}}/\epsilon_{\text{out}}$, i.e. the ratio between the permittivities inside the sphere and in the host medium. Here, ϵ_{in} and ϵ_{out} are absolute permittivites with units $\text{F}\,\text{m}^{-1}$, as opposed to the often used dimensionless relative permittivites, which are defined by the ratio of the absolute permittivity to the vacuum permittivity. As we are here just using the ratio between the permittivities, it does not matter if we have the factor ϵ_0 or not in our permittivities, but we will later encounter equations where it absolutely *does* matter.

Using the previously defined ϵ_{r} and the boundary conditions from equation set 2.9, the solution for the electric field inside the sphere becomes

$$\mathbf{E}_{\text{in}} = \frac{3\mathbf{E}_0}{\epsilon_{\text{r}} + 2}. \tag{2.10}$$

In other words, the field inside the sphere is uniform. Further, the potential outside can be found to be

$$V_{\text{out}}(r, \theta) = -E_0 r \cos\theta + \frac{\epsilon_{\text{r}} - 1}{\epsilon_{\text{r}} + 2} \cdot \frac{E_0 R^3 \cos\theta}{r^2}, \tag{2.11}$$

and is the superposition of the potential from the external field and the induced dipole potential. From equation 2.6, we then get the electric field outside to be

$$\begin{aligned} \mathbf{E}_{\text{out}} = &\left(E_0 \cos\theta + 2\frac{\epsilon_{\text{r}} - 1}{\epsilon_{\text{r}} + 2} R^3 E_0 \frac{\cos\theta}{r^3} \right) \hat{\mathbf{r}} \\ &+ \left(-E_0 \sin\theta + \frac{\epsilon_{\text{r}} - 1}{\epsilon_{\text{r}} + 2} R^3 E_0 \frac{\cos\theta}{r^3} \right) \hat{\theta}. \end{aligned} \tag{2.12}$$

In total, the electric field in and around the dielectric sphere as described from the equations 2.10 and 2.12 is shown in figure 2.4.

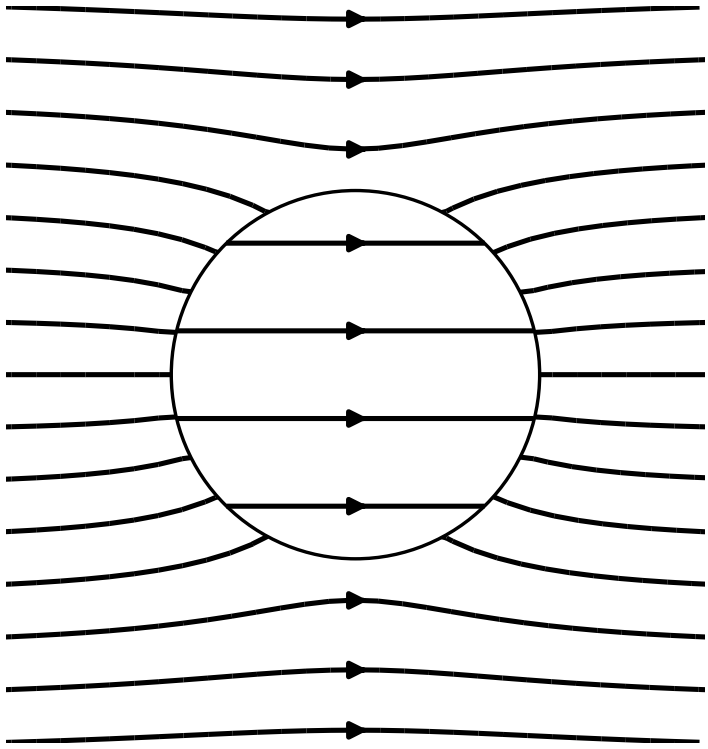

Figure 2.4: Electric field in and around a dielectric sphere in a homogeneous external field, as described by equations 2.10 and 2.12, with $\epsilon_\mathrm{r} = 3$ in this example. The electric field is directed from left to right.

The polarisation charge on the sphere surface is given by the induced potential part of equation 2.11. The dipole moment $\mathbf{p}$ for a general dipole field is found in the equation

$$V = \frac{|\mathbf{p}| \cos\theta}{4\pi\epsilon_0 r^2}, \tag{2.13}$$

and thus, we get that

$$\mathbf{p} = 4\pi\epsilon_0 \frac{\epsilon_\mathrm{r} - 1}{\epsilon_\mathrm{r} + 2} R^3 \mathbf{E}_0. \tag{2.14}$$

Since the total polarisation $\mathbf{P}$ for the sphere is given by the density of the dipole moment, we have

$$\mathbf{P} = \frac{\mathbf{p}}{\frac{3}{4}\pi R^3} = 3\epsilon_0 \frac{\epsilon_\mathrm{r} - 1}{\epsilon_\mathrm{r} + 2} \mathbf{E}_0, \tag{2.15}$$

and as $\mathbf{P}$ and $\mathbf{E}_0$ are parallel, we get a surface charge on the sphere as $q_\mathrm{b} = \mathbf{P} \cdot \hat{\mathbf{n}}$, and further $q_\mathrm{b} = |\mathbf{P}| \cos\theta$, or in its expanded form [26]:

$$q_\mathrm{b} = 3\epsilon_0 \frac{\epsilon_\mathrm{r} - 1}{\epsilon_\mathrm{r} + 2} E_0 \cos\theta. \tag{2.16}$$

The subscript in q_b denotes that these are bound charges. The polarisation comes from the small displacement of the positive and negative charges in the atom from the electric field, creating a small dipole moment in each atom, which in total becomes the polarisation $\mathbf{P}$. The charges do not escape from the atom (unless the electric field is strong enough to ionize the atoms), but all the charges are slightly shifted in the material, so that a surface charge equal to q_b appears.[1]

2.4 The perfect dielectric model

While the results from section 2.3 are simple in their form, they are only for a solid dielectric material with only electrostatic interactions with the dielectric host medium. The dielectric model is based on Gauss's law (2.7), which was first formulated in the 18$^{\mathrm{th}}$ century.

Much later, in 1953, the perfect dielectric model was developed by O'Konski and Thacher, predicting the fact that droplets would deform under an electric field [27]. They derived an equation for the distortion for liquid aerosol droplets under an electric field, valid for static fields in insulating media when the droplet eccentricity (and thus deformation) is small. The equation,

$$e = 3E_0 |\epsilon_\mathrm{in} - \epsilon_\mathrm{out}| \frac{\sqrt{\epsilon_\mathrm{out} R/\gamma}}{2\left(\epsilon_\mathrm{out} + 2\epsilon_\mathrm{in}\right)}, \tag{2.17}$$

gives the droplet eccentricity e as a function of the field strength E_0, permittivities ϵ_in and ϵ_out, radius R of the un-deformed droplet (when $e = 0$), and the interfacial tension between the droplet and the medium γ. The droplet is then always elongated in the direction of the field (i.e. with the semi-major axis a along the electric field direction and semi-minor axis b normal to the field), as long as the host fluid can be regarded as a perfect dielectric, whether the droplet permittivity is greater or less than the host fluid permittivity. Figure 2.5 shows this situation. Note that the eccentricity is exaggerated.

The eccentricity is here defined as

$$e = \sqrt{1 - \frac{b^2}{a^2}} \tag{2.18}$$

[1] For more on this topic, see chapters 4.2.1 and 4.2.2 of [25].

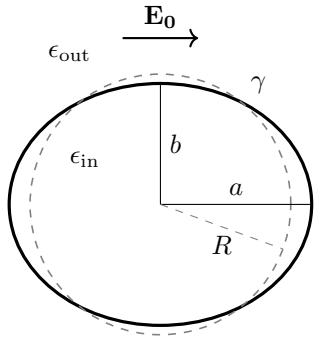

Figure 2.5: Schematics of a deformed drop, with the applied E-field parallel to the semi-major axis a, and thus normal to the semi-minor axis b. The eccentricity e is defined according to equation 2.18, and $R = a^{1/3}b^{2/3}$ for a prolate spheroid. In this figure the eccentricity is greatly exaggerated, as it is 0.6 in this image; far out of the "small e" regime assumed for the derivation of equation 2.17.

for $b < a$, by the definition of the semi-minor and semi-major axes. Another often used parameter for the droplet oblateness is the droplet deformation parameter D, defined as

$$D = \frac{d_{\parallel} - d_{\perp}}{d_{\parallel} + d_{\perp}}, \tag{2.19}$$

with $d_{\parallel}$ and $d_{\perp}$ being the lengths of the droplet, parallel and perpendicular to the electric field respectively. As the semi-major axis a and semi-minor axis b are half that of $d_{\parallel}$ and $d_{\perp}$ for a prolate drop (that is, when $d_{\parallel} > d_{\perp}$, as opposed to an oblate drop for when $d_{\parallel} > d_{\perp}$), we can find the relation between the eccentricity and drop deformation to be

$$D = \frac{1 - \sqrt{1 - e^2}}{1 + \sqrt{1 - e^2}}, \tag{2.20}$$

or reversibly,

$$e = \sqrt{1 - \left(\frac{1 - D}{1 + D}\right)^2}. \tag{2.21}$$

For the small e limitation, we can approximate D to be $D \simeq \frac{1}{4}e^2$, and thus, from equation 2.17, get the expression for the droplet deformation parameter for small deformations as

$$D = \frac{9}{16}\frac{\epsilon_{\text{out}} R E_0^2 \left(\epsilon_{\text{r}} - 1\right)^2}{\gamma \left(\epsilon_{\text{r}} + 2\right)^2}. \tag{2.22}$$

An understanding of why the droplet is deformed, as described in both equation 2.17 and equation 2.22, comes from the surface charge described in equation

2.16. The applied electric field E_0 pulls the charges, and thus the droplet itself is slightly deformed. The positive charges move in the direction of the electric field, and the negative charges move in the opposite direction.

The theoretical results of the perfect dielectric model were experimentally verified by O'Konski and Gunther in 1955, by suspending $\sim 0.5\,\mathrm{mm}$ water droplets in air and measuring the eccentricity from analysing photographs [28]. Water is a very good conductor, and air is an insulator, so they could set ϵ_{in} equal to infinity, and got experimental results within 1 % deviation from the theory for even rather large eccentricities ($e = 0.6$).

But other experimental results showed that droplets could also become oblate (stretching normal to the electric field) [29], something that is not explained by equation 2.22, as an oblate shape has negative deformation D, which equation 2.22 does not allow. O'Konski together with Harris tried to derive a theory that allowed oblate droplets by introducing electric conductivity in both fluids [30], as compared to the previous theory for an insulating host fluid [27]. The new results predicted a droplet deformation of

$$D = \frac{9}{64}\frac{\epsilon_{\mathrm{out}} R E_0^2}{\pi\gamma}\frac{(\sigma_{\mathrm{r}}-1)\left(\sigma_{\mathrm{r}}^2+7\sigma_{\mathrm{r}}-2-6\epsilon_{\mathrm{r}}\right)}{(\sigma_{\mathrm{r}}+2)^3}, \tag{2.23}$$

where $\sigma_{\mathrm{r}} = \sigma_{\mathrm{in}}/\sigma_{\mathrm{out}}$ is the ratio between electric conductivities σ of the fluids, which would give an oblate droplet for

$$\sigma_{\mathrm{r}} > 1 \quad \text{and} \quad \sigma_{\mathrm{r}}^2 + 7\sigma_{\mathrm{r}} - 2 < 6\epsilon_{\mathrm{r}} \tag{2.24a}$$

or

$$\sigma_{\mathrm{r}} < 1 \quad \text{and} \quad \sigma_{\mathrm{r}}^2 + 7\sigma_{\mathrm{r}} - 2 > 6\epsilon_{\mathrm{r}}. \tag{2.24b}$$

But experimental results did not support the model in equations 2.24, and thus the leaky-dielectric model was created [31].

2.5 The leaky dielectric model

Sir Geoffrey I. Taylor is the creator of the leaky dielectric model, a work which was published in 1966 [32]. Today, the model holds the full name of "Taylor-Melcher leaky dielectric model", named after Taylor and James R. Melcher, who together with Taylor published a review of electrohydrodynamics (EHD) [33], and who used the leaky dielectric model extensively to develop the field of EHD. Even though the Taylor-Melcher model uses several approximations, it is still in use today, and has support in most of the experimental studies today [34].

Taylor realised that there must be a surface charge, also after the system reaching a steady state [32]. For a spherical droplet in an electric field at equilibrium, there must be a balance between electric stresses and variable pressure difference at the drop surface, which can only occur if the fluids both inside and outside the drop are in motion. Taylor discovered that there was fluid flow in the droplet, something that had not been considered in the earlier models previously described [27, 30, 31].

The leaky dielectric model only considers cases where the stress due to inertia is small compared to that due to viscosity, i.e. for small Reynolds numbers ($\mathrm{Re} \ll 1$). The stresses on the interface from the electric field must be balanced by the viscous stresses from hydrodynamic currents. The stream function ψ from fluid mechanics describes the fluid motion, where lines of constant ψ are streamlines of the flow [18], with velocity components u and v in polar coordinates defined as

$$u = \frac{1}{r^2 \sin\theta} \frac{\partial \psi}{\partial \theta} \quad \text{and} \quad v = \frac{-1}{r \sin\theta} \frac{\partial \psi}{\partial r}. \tag{2.25}$$

The stream function must satisfy the condition [32]

$$\mathrm{D}^4 \psi = 0, \tag{2.26}$$

where the operator D^2 is [35]

$$\mathrm{D}^2 = \frac{\partial^2}{\partial r^2} + \frac{\sin\theta}{r^2} \frac{\partial}{\partial \theta} \left(\frac{1}{\sin\theta} \frac{\partial}{\partial \theta} \right). \tag{2.27}$$

The solution for a droplet with radius R is then given by [32]

$$\psi_{\mathrm{in}} = v_{\max} \left(\frac{r^3}{R} - \frac{r^5}{R^3} \right) \sin^2\theta \cos\theta \tag{2.28a}$$

$$\psi_{\mathrm{out}} = v_{\max} \left(\frac{R^4}{r^2} - R^2 \right) \sin^2\theta \cos\theta, \tag{2.28b}$$

where ψ_{in} is the stream function inside, and ψ_{out} is the stream function outside. The factor $v_{\max}$ is the maximum velocity of the flow, which occurs at the interface ($r = R$) at $\theta = \left\{ \frac{\pi}{4}, \frac{3\pi}{4}, \frac{5\pi}{4}, \frac{7\pi}{4} \right\}$, and is given by

$$v_{\max} = -\frac{9 \epsilon_{\mathrm{out}} R E_0^2}{8\pi \left(2 + \sigma_{\mathrm{r}}\right)^2} \cdot \frac{\sigma_{\mathrm{r}} - \epsilon_{\mathrm{r}}}{5 \left(\mu_{\mathrm{in}} + \mu_{\mathrm{out}}\right)}, \tag{2.29}$$

where we as before have the number $\sigma_{\mathrm{r}} = \sigma_{\mathrm{in}}/\sigma_{\mathrm{out}}$ (the ratio between the electric conductivity of the fluids inside and outside), and where μ_{in} is the dynamic viscosity of the droplet fluid, and μ_{out} similarly is the dynamic viscosity of the host fluid. The fluid motion in and around the droplet due to the electric field can be seen in figure 2.6.

The flow direction is dependent on the value of $v_{\max}$ from equation 2.29, and changes direction when $v_{\max}$ switches sign. The flow direction in the drop is

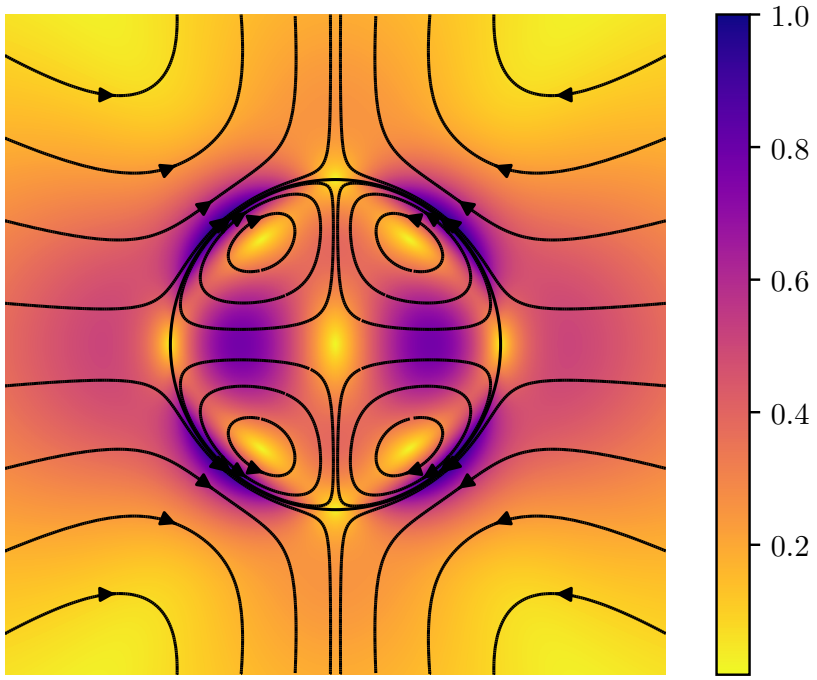

Figure 2.6: Schematics of the flow inside and around a droplet induced from the electric field. The flow is described by the equations 2.28 and 2.29. If $v_{\max}$ from equation 2.29 is positive (as in this case), the circulation in the drop is from pole to equator, and if $v_{\max}$ is negative, the circulation is from equator to pole. The colourmap indicates the speed $\sqrt{u^2+v^2}$, with u and v from equation 2.25, and normalised so that the maximum speed is 1.

from the equator to the poles when $v_{\max}$ is positive and thus when $\sigma_{\mathrm{r}} < \epsilon_{\mathrm{r}}$. Reversibly, opposite flow direction occurs when $\epsilon_{\mathrm{r}} < \sigma_{\mathrm{r}}$. When $\epsilon_{\mathrm{r}} = \sigma_{\mathrm{r}}$, no flow is induced.

As for the shape of the droplet, Taylor showed that the droplet is prolate for $\phi > 0$, and oblate when $\phi < 0$, where ϕ is the dimensionless discriminating function [36]

$$\phi\left(\epsilon_{\mathrm{r}}, \sigma_{\mathrm{r}}, \mu_{\mathrm{r}}\right) = \sigma_{\mathrm{r}}^2 + 1 - 2\epsilon_{\mathrm{r}} + \frac{3}{5}\left(\sigma_{\mathrm{r}} - \epsilon_{\mathrm{r}}\right)\frac{3\mu_{\mathrm{r}} + 2}{\mu_{\mathrm{r}} + 1}, \tag{2.30}$$

where $\mu_{\mathrm{r}} = \mu_{\mathrm{in}}/\mu_{\mathrm{out}}$ is the ratio between the viscosity inside and outside the

droplet. The droplet deformation D itself is then [36, 37]

$$D = \frac{9}{16}\frac{\epsilon_{\text{out}} R E_0^2}{\gamma} \cdot \frac{\phi\left(\epsilon_{\text{r}}, \sigma_{\text{r}}, \mu_{\text{r}}\right)}{\left(2+\sigma_{\text{r}}\right)^2}, \tag{2.31}$$

which as before gives prolate deformation for $D > 0$ and oblate deformation for $D < 0$.[2]

The deformation in the electric field is not instantaneous, as the charges on the drop surface need time to build up, which is on a timescale of the Maxwell-Wagner polarisation time t_{MW} [40]

$$t_{\text{MW}} = \frac{\epsilon_{\text{in}} + 2\epsilon_{\text{out}}}{\sigma_{\text{in}} + 2\sigma_{\text{out}}}, \tag{2.32}$$

which is typically in the range 0.1 s to 10 s [39, 40, 42]. The same range is usually the time scale for the flow, which is the time for a particle inside to be moved to the drop surface.

Note that the case of the droplet becoming oblate or prolate is determined by the two fluids permittivities ϵ, conductivities σ and viscosities μ alone, and seems not to be dependent on the field strength E_0. But remember that equation 2.31 was derived for two pure fluids, and with a droplet with small deformations only. It has been shown that the deformation can change sign if the fluid interface is coated with conducting particles, like clay, where the droplets begin as oblate for medium fields ($E_0 = 200\,\text{V}\,\text{mm}^{-1}$), and become prolate for higher fields ($E_0 = 500\,\text{V}\,\text{mm}^{-1}$), as the clay particles short-circuit a droplet of silicone oil in castor oil [42].

This model predicts elongation along the external field direction $\mathbf{E}_0$, or normal to it, and does so well at moderately low stable field strengths ($E_0 \sim 100\,\text{V}\,\text{mm}^{-1}$ to $200\,\text{V}\,\text{mm}^{-1}$) [32, 34, 42, 43]. But at high field strengths (roughly $E_0 > 300\,\text{V}\,\text{mm}^{-1}$), the droplets have been shown to start to tilt at an oblique angle, and to rotate, even though the field itself is stable [37, 40, 41, 44, 45].

2.6 Glass transition of polymers

A polymer is a molecule which is itself built out of a large number of molecular units that, linked together by covalent bonds [46]. Examples of polymers are

[2] There are a lot of different versions of the equations around ϕ and deformation D. The equations from [32, 34, 36, 38] are all different. I have here decided to use the equation of Baygents *et al.*, as it seems to be the consensus for recent publications [26, 37, 39–41].

polyethylene and polystyrene, both organic molecules with long chains of carbon and hydrogen, as shown in the figures 2.7a and 2.7b. The number of monomers in a chain can be on the order of 10^4.

(a) Polyethylene: $(CH_2)_n$ (b) Polystyrene: $(C_8H_8)_n$

Figure 2.7: Chemical structures for polyethylene (PE) and polystyrene (PS).

Due to their large molecule sizes, polymers do not behave like regular low molar mass media. While the latter usually have perfectly elastic solids and only have viscous forces for liquids, polymers have elastic and viscous properties both in fluid and solid states. The contribution of the elasticity and viscosity depend on the temperature, which gives polymers much more temperature sensitivity than regular materials. This gives arise to glass transition temperature, which is a temperature where the state goes from liquid equilibrium to a state where the thermal equilibrium is only partly established [47]. In other words, the glass transition temperature is where the polymer goes from having a defined viscosity (hot, but below the temperature of equilibrium crystallisation transition), to having such a high viscosity that the polymer can no longer flow on an experimental timescale (cold, but above a theoretical infinite viscosity) [48].

As it may be apparent, the exact definition of the glass transition temperature is a matter of convention. Another such definition is that the glass transition temperature is where the dynamic viscosity of the polymer crosses $10^{12}\,\mathrm{Pa\,s}$ [48, 49]. The glass transition temperature for polystyrene is roughly 100 °C, where the transition extends over a temperature range on the order of 10 degrees, and the location of the transition temperature also depends on the rate of temperature change which it is measured over. The melting point for polystyrene is approximately 240 °C, comparatively [50]. The glass transition temperature is usually determined by measuring the expansion coefficient or heat capacity of a sample, both of which change with different rate during the glass transition, compared to the temperatures surrounding it [47].

Chapter 3

Methods

For these experiments the goal was to fabricate capsules of a material, covering a droplet in a host fluid. The result, silicone oil droplets covered by a capsule of sintered polystyrene particles, is the culmination of a yearlong process of different experiments, methods, ideas, and challenges. Here in this chapter, the different attempted capsule materials will be described, together with different methods of fabricating the droplets, and other aspects of performing the experiments.

3.1 Setup for capsule fabrication experiments

The experiments for capsule fabrication were designed and performed at NTNU, with a setup as shown in the flowchart in figure 3.1. Droplets of silicone oil containing particles were made in a sample cell with castor oil. The droplets, ranging from 100 µm to 2000 µm in diameter, were then subject to the electric field, typically in the range of $100\,\mathrm{V\,mm^{-1}}$ to $300\,\mathrm{V\,mm^{-1}}$. This field allowed the particles inside the droplet to move to the droplet surface, where they are trapped by the capillary forces. When all the particles have been located to the drop surface, the electric field was switched off, and external heating was switched on. The contents of the sample cell were heated to $\sim 100\,^{\circ}\mathrm{C}$, and the temperature was kept for approximately 10 min, to allow the particles to merge into a rigid shell. Finally, the sample was cooled back down to room temperature, and the droplets were removed from the cell.

To ensure the safety of the user and surroundings, the heating plate and electric power source were both connected to a safety switch and fuse, so that they both quickly could have been turn off in case of an emergency.

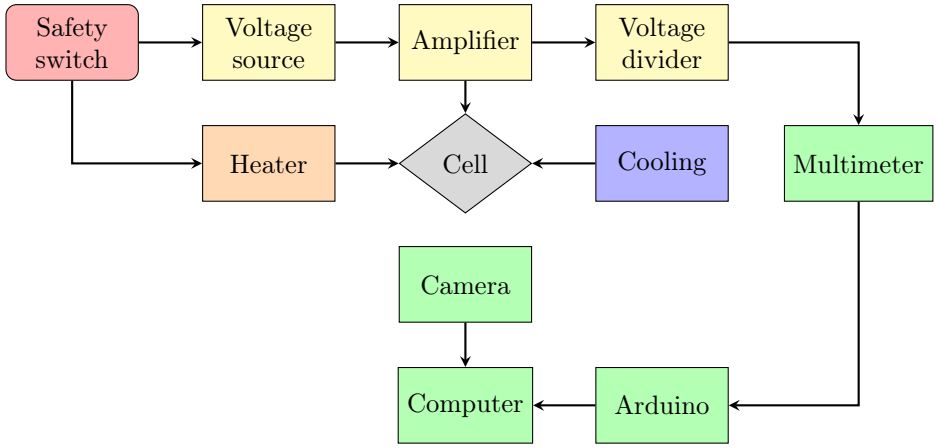

Figure 3.1: Experimental setup for droplet fabrication, encapsulation, and sintering. Yellow colour indicates systems for the electric field, and green colour indicates systems for measurement.

3.2 Electric field apparatus

To achieve fields of several hundreds of volts per millimetre in the sample cell with a width of 15 mm, a voltage in the kilovolt range was needed. The analogue DC power source used was a GW Laboratory DC Power Supply GPS-3030, which allowed a maximum voltage of 30 V. The voltage then had to be amplified, which was performed with a NTNU-built 1000× amplifier. The amplifier gave a non-linear response, so to accurately measure the voltage applied over the sample cell, a NTNU-built down-converter reduced the voltage by a factor 1:1000, which could then be measured by a Fluke 115 Multimeter. The amplified high voltage, typically $\sim 3\,\mathrm{kV}$, was then applied over the sample cell using high voltage rated crocodile clamps, attached to copper electrodes that were put in contact with the sample cell walls. The sample cell itself consisted of a glass base with four walls, two opposing sides of glass and two of indium tin oxide (ITO), which is transparent as glass, but is a good conductor, contrary to glass. The ITO on the inside walls gave a reasonably uniform field across the contents of the cell. The cell had a length and width of 15 mm each, and height of 25 mm (schematics in figure 3.2).

According to the equation for electric field (equation 2.6), if the distance between the two conducting walls is decreased, the maximum field is increased. This was exploited for some AC experiments, because another and weaker amplifier had to be used, which was circumvented by creating a smaller cell with a width of 5 mm. But the decreased width became a challenge when trying to fit in the copper electrodes on each ITO side, without the electrodes touching each other. Also, for an increasing ratio between droplet size and cell width, the droplet

easier attached to the wall, deforming the droplet.

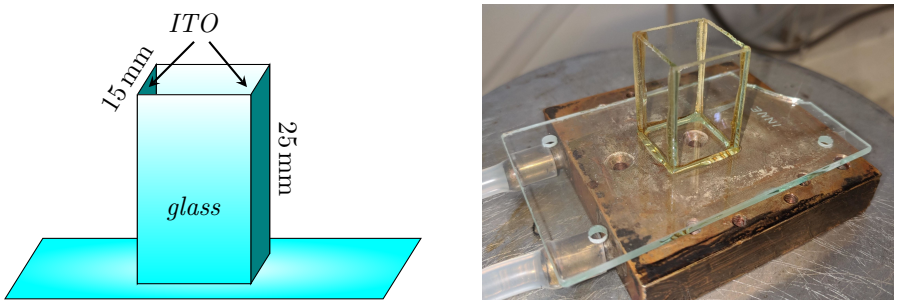

Figure 3.2: Schematics of the sample cell that was used to make droplets in (left), together with a photo of the one that was used in the experiments (right). For the schematics, the glass plates are in shaded cyan and the ITO plates are in teal (with ITO coating on the inside of the cell). As it is apparent in the photo, the true colour and appearance of ITO is indistinguishable to that of glass.

3.3 Heating and cooling of the samples

3.3.1 Temperature control

To fabricate the capsules, different methods of capsule hardening were proposed, like using an UV curable resin to produce double emulsions (droplet of one medium covered by a film of another medium, all in a host fluid, as shown in figure 2.2b), and then curing the resin emulsion. But due to considerations of available time and experience, it was decided to fabricate capsules by sintering particles on the drop surface. For heating, the sample cell was placed on a Heidolph MR 3003 heater, which could be set to a desired temperature of up to 300 °C. A box of plexiglass was placed around the sample cell, both to isolate the system, and as a safety measure to protect the user from high temperatures and high voltages.

To cool down the system afterwards, a copper plate with water pipelines inside was placed under the cell, on top of the heating plate. A Lauda E 300 water pump with water at ambient temperature was attached to the copper plate, which circulated the water when cooling the sample, allowing effective cooling, so that the droplets could be removed from the sample cell afterwards. As the copper plate was between the sample cell and the heating plate, there was some lag in heating up the sample, as shown in figure 3.3. It took roughly 15 min to reach a stable temperature inside the sample cell while heating, and approximately the

same time to cool down when the cooling was engaged.

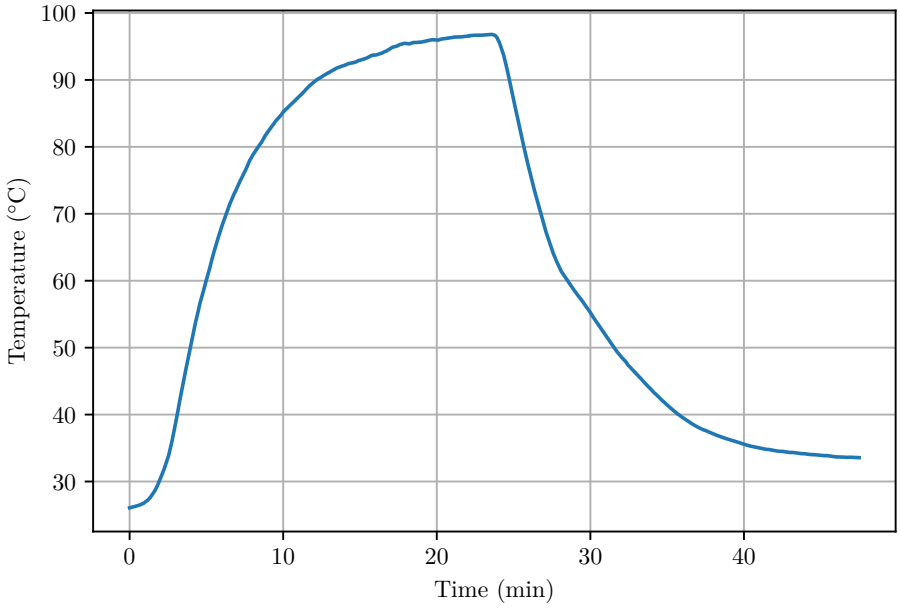

Figure 3.3: Characteristic temperature profile, measured with a thermocouple connected to an Agilent U1253A multimeter. The heating was engaged at 0 s. The heating was shut off 23 min, and cooling immediately engaged, at where the temperature immediately fell. The heating plate was set to a temperature of 150 °C, but the sample cell did not reach that temperature, as maximum temperature was 96.8 °C, just as the heating was turned off.

3.3.2 Heat convection

While heating the droplets in the host fluid, significant heat convection was observed, as the hotter regions of the oil in the bottom of the cell rose, and cooler regions of oil from the top of the cell sank. This proved to be a large problem for producing the capsules, as larger droplets became torn apart by shear stresses from the convection flow, and from droplets rupturing when the droplets got pushed up to the host fluid surface.

Several methods were tried to reduce heat convection. One method was to isolate the sample cell better by covering all holes in the plexiglass box where ambient air could enter, but this had no significant effect. Also reducing the host fluid

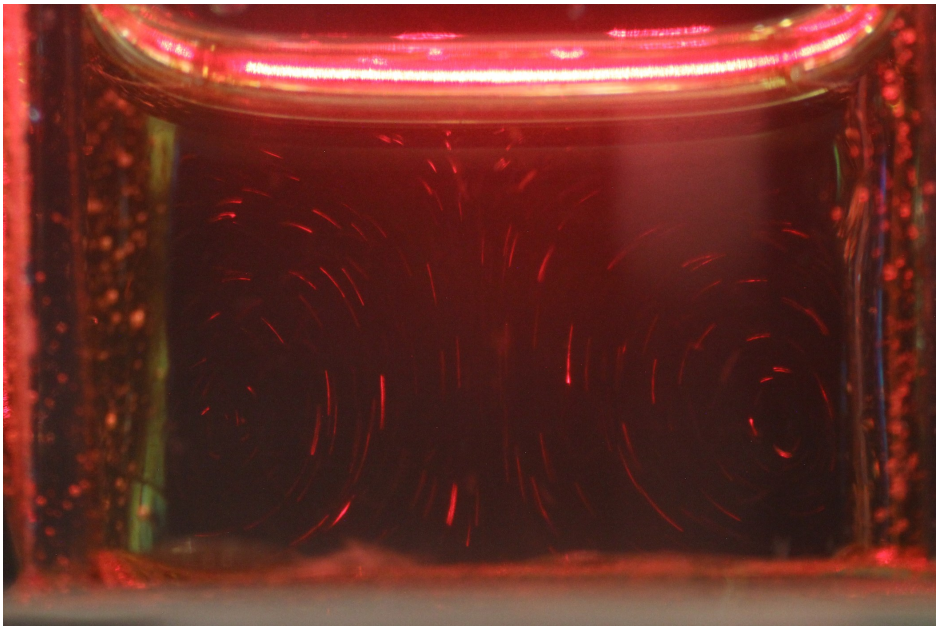

Figure 3.4: Photo of the heat convection in the sample cell. This was a four second exposure, using a laser with polystyrene beads as scattering particles in castor oil, while heating. The cell width was 15 mm, and temperature approximately 70 °C.

volume, so that the depth was reduced, did not show any noticeable improvement, in addition to make it harder to inject the droplets into the oil.

A more effective method was to create a new sample cell with a low viscosity oil bath surrounding the sample cell, so that heat convection would only appear in the outer fluid, making the temperature even around the inner cell with the droplets, so that the inner heat convection would be reduced. This proved to reduce the heat convection significantly, but also increased the heating time drastically, up to approximately 45 min, while impairing the image from the microscope, as there was a thick layer of moving oil around the sample cell.

Finally, to circumvent the problem of drop deformation and destruction from heat convection, it was decided to only produce droplets so small that they would not be noticeably affected by the convection flow, as the surface tension is significantly stronger than the shear stresses for sub-millimetre droplets. This maximum droplet diameter showed to be approximately 1 mm, and thus the capsules fabricated in these experiments do not exceed this size.

3.4 Data logging

Several instruments were used to record the conditions inside the sample cell. For imaging and video recording, a Canon EOS 600D digital camera was used, attached to a Zeiss Stemi 2000-C microscope, which gave a maximum camera resolution of roughly 0.5 µm per pixel with the 18-megapixel camera. In video, with a maximum resolution of full HD (1920 pixels by 1080 pixels), the maximum resolution was 1.3 µm per pixel. This resolution was adequate for looking at the droplet dynamics but did not allow closer inspection of the contact between the particles.

As for voltage measurements, the multimeter did not allow data exportation, so an Arduino UNO R3 microcontroller was used to register the voltage. The Arduino was programmed to measure the voltage from the voltage divider, with the code being available in appendix A.1. Both the resolution and precision of the Arduino measurements were a bit low, consequently, the average of five voltage measurements over 50 ms was recorded. The software GoBetwino[1] was used, as the Arduino microcontroller independently not could export data with timestamps. The GoBetwino software monitored the serial port for data sent from the Arduino and saved it with a time stamp to a text file on the computer. In that way, the voltage in the sample cell could be recorded and saved every second.

A Python script was finally used to import the voltages from the file with voltage measurements to create video subtitles for the recorded videos with the electric field appearing as video subtitles, synced in time with the video itself. The Python code is available in appendix A.2. Due to different clocks in the camera and the computer, and some lag in the Arduino and serial port monitor software, the subtitles were not perfectly in sync with the recorded action, but an accuracy of somewhere around 1 s to 2 s was reached. Due to these efforts, it was possible to see what the specific electric field was at any moment in the videos, with relatively little effort.

3.5 Producing and removing the droplets

The task of producing the droplets, and removing them after sintering, proved to be difficult. The emphasis was on producing similar sized droplets with similar particle concentrations, which proved to be challenging, due to the reasons discussed below. The droplet fluid was made by mixing the droplet oil together with a specific amount of particles. For a fully covered droplet with spherical

[1] `https://web.archive.org/web/20171113125718/http://www.mikmo.dk:80/gobetwinodownload.html`

particles, the mass ratio between added oil and particles is given by

$$\frac{M_{\text{oil}}}{M_{\text{particle}}} = \frac{1}{4\eta} \frac{\rho_{\text{oil}}}{\rho_{\text{particle}}} \frac{D_{\text{oil}}}{d_{\text{particle}}}, \tag{3.1}$$

where M_{oil} and M_{particle} are the total masses for added oil and particles respectively, with ρ being density, D is the droplet diameter and d the particle diameter, and η is the particle packing density (hexagonal packing of spheres in one layer yields $\eta = \frac{\pi}{2\sqrt{3}} \approx 0.9069$). But due to particle sedimentation, it was hard to get equal particle concentration for every new sample. This was partly solved by the Taylor-Melcher flow induced from the electric field (see section 2.5), ejecting excessive particles out from the droplet. But if the sedimentation and unevenness is compensated for by adding an excess of particles, the oil-particle mix easier sediments and clogs up stationary syringe pumps or similar drop size controllers. There was also some delay in turning on/off the syringe pump and getting out fluid in the other end of the pipe into the cell, reducing the amount of control over the droplet fabrication process.

It was also attempted to have a glass capillary tube into the cell which could inject fluid. But as previously noted, high particle concentrations clogged the pipe. Additionally, the ejected droplets attached themselves to the side of the capillary, failing to form free droplets in the fluid. Adding too much fluid would also produce too large droplets, without an easy way of reducing them afterwards. Due to the lag in the piping, this was often the case, as there was little control over the actual amount of fluid being ejected.

Thus, the easiest method was to use a simple Thermo Labsystems Finnpipette micropipette. A droplet with a diameter of 1.0 mm has a volume of 0.52 µL, so a very small volume must be injected. The smallest micropipettes available for this experiment was a 0.2 µL to 2 µL pipette. 2 µL gives a 0.7 mm droplet, so smaller droplets were produced by dragging the pipette tip around while injecting the oil-particle mix, as shown in the photos in figure 3.5.

As for removing the encapsulated droplets after sintering, simply pouring the contents of the cell into a Petri dish posed too great shear stresses for the capsules, often tearing them apart. Capsules in the cell corners also did not flow easily, due to the high viscosity used for the host fluid, and surface tension. Therefore, the capsules had to be removed carefully manually with a suctioning syringe pump. A syringe tip with an inner diameter of 1.6 mm was used, while injecting at a speed of 50 µL min^{-1}. After cleaning the sample cell for capsules, the encapsulated droplets were then injected into a Petri dish at the same tempo of 50 µL min^{-1}, and promptly stored for later use and observation.

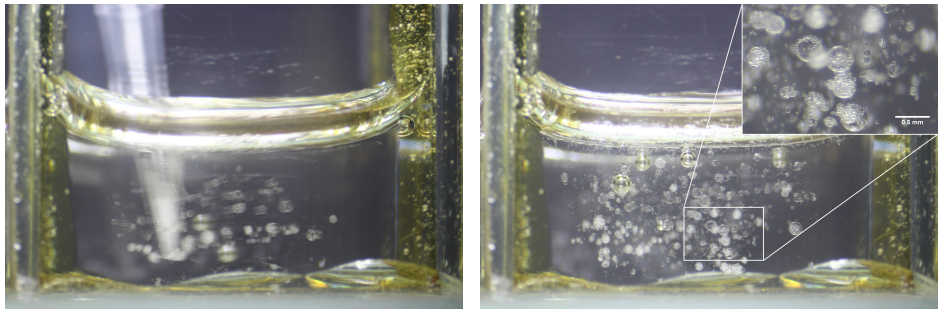

(a) (b)

Figure 3.5: Producing droplets in the 15 mm sample cell. Photos from stirring while injecting (a), and after (b). The droplets' sizes range from 150 µm to 500 µm, with 40 µm particles. The scale bar in the cut-out is 0.5 mm

3.6 Properties of the oils used

There are some restrictions for what fluids to use in the droplet and host medium. An important restriction is that the fluids must be non-miscible. For visual observation, they should also be close to transparent.

Further, the oil densities should be as similar as possible to get neutral buoyancy, to prevent strong sedimentation or floating of the droplets. As the droplet deformation is dependent on the interfacial tension ($D \sim \frac{E_0^2}{\gamma}$), while the drop flow velocity not ($v_{\max} \sim E_0^2$), it is preferable with an oil combination with moderate/high interfacial tension, so that the drop deformation is not exaggerated, risking that droplets burst if the electric field is too high. If the interfacial tension is too low, and one tries to compensate with reducing the applied E-field, the drop flow velocity is reduced, resulting in slower build-up of particles on the surface, and thus fluids with applicable interfacial tension should be used.

From equation 2.29, it is apparent that two fluids are wanted so that $\sigma_r - \epsilon_r = \frac{\sigma_{in}}{\sigma_{out}} - \frac{\epsilon_{in}}{\epsilon_{out}}$ is non-zero, or else there will be no flow. The conductivities and permittivities should further be chosen while considering the Maxwell-Wagner time, given by equation 2.32, denoting the time for the charge to build up on the interface. If this time is too large, the fluid flow takes a long time to initiate and push the particles to the surface, and therefore it is preferable that the fluid conductivities and permittivities are chosen accordingly.

Finally, a moderate/high viscosity is wanted to get a low Reynolds number, to minimise turbulence. This also makes it easier to observe the droplets, as mechanical vibrations are reduced.

The oils used in these experiments were silicone oil for the droplets (Dow Corning 200/100cSt, prod. 630074A), and castor oil as the host fluid (Alfa Aesar Castor Oil, L04224). They had both been used previously in the lab and were therefore quite old. It is unknown how this affects the oils, but as this project was more of a qualitatively than a quantitative study, this was not regarded as a problem. The interfacial surface tension between the two oils is $\gamma_{\mathrm{Si-Castor}} = 4.5\,\mathrm{mN\,m^{-1}}$ [40], which is relatively low compared to the surface tension between water and many oils, which is typically on an order of magnitude higher than the one between silicone oil and castor oil [42]. The other relevant parameters for the fluids are given in table 3.1. Note that the kinematic viscosity ν is listed, and it is defined as the ratio between the dynamic viscosity divided by the density, $\nu = \mu/\rho$. Also, it should be noted that the oil that were used were past their expiry dates, so the parameters could have changed, but as the results were qualitative, it was not bothered to buy new oils. No rancidity or other signs of reduced quality was noted, however.

Table 3.1: Table of the specifications of the two fluids used in these experiments. Data from [42]. Due to the nature of vegetable oils like castor, there is expected to be some variation in these values from different manufacturers and bottles.

	Castor oil	Silicone oil	Relative (in/out)
Permittivity, ϵ ($\mathrm{F\,m^{-1}}$)	4.2×10^{-11}	1.9×10^{-11}	0.45
Conductivity, σ ($\mathrm{S\,m^{-1}}$)	4.5×10^{-11}	4×10^{-12}	0.1
Kin. viscosity, ν ($\mathrm{m^2\,s^{-1}}$)	1.00×10^{-3}	1.00×10^{-4}	0.100
Density, ρ ($\mathrm{kg\,m^{-3}}$)	961	970	1.01

3.7 Capsule materials

If a droplet in an electric field is fully covered with a conductive material, the drop will be short circuited, suppressing the Taylor-Melcher flow [42]. In these experiments, the droplets were covered with different insulating materials, in different attempts of fabricating capsules. Several methods were attempted, consisting of either melting capsules around the drops, or sintering particles by using the glass phase transition.

3.7.1 Wax

The first experiments included use of wax as the capsule material, due to the low melting point of wax, and a very low conductivity. The wax that was used was Hampton Research Capillary Wax, which has a melting point of 79 °C. The

wax was attempted crushed to fine dust, but this was difficult due to the low melting point, as the wax easily melted while grinding, melting together to larger patches, inhibiting the whole purpose of the grinding. It was also attempted to use liquid nitrogen to cool the wax while grinding, while also making the wax more brittle, but it did not help significantly. Due to the manual grinding and previously mentioned difficulties, the wax particles had a wide range of sizes, as can be seen in figure 3.6a.

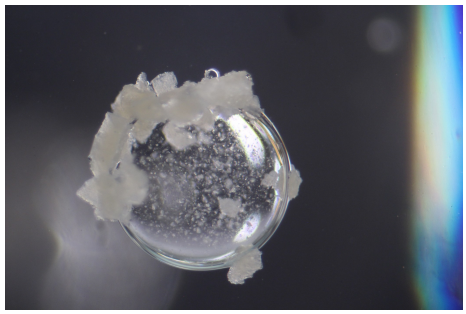

(a) Silicone oil droplet with wax particles. Droplet size is roughly 1 mm. Wax can be seen as both large particles on the interface, and much smaller particles inside the droplet.

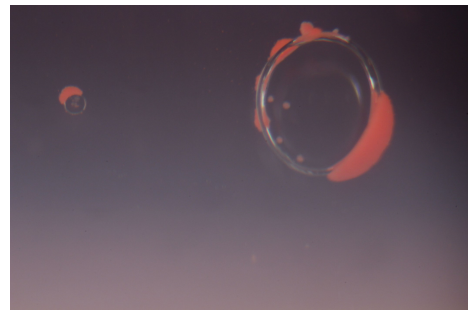

(b) Droplets of polyethylene (red) on the side of the silicone oil droplet. Droplet sizes are approximately 1 mm for the large droplet, and approximately 150 µm for the small droplet to the left.

Figure 3.6

When melted, the wax formed a thin layer around the droplet. But due to the thinness of the layer, and the general brittleness of wax, the capsule was far from strong enough to withstand any forces, and the idea of using wax was discarded.

3.7.2 Polyethylene

Further experiments involved the use of polymers. Polyethylene (PE) beads from Cospheric LLC (UVPMS-BR-1.050 45-53um) were used, with diameters ranging from 45 µm to 53 µm. PE has a melting temperature at 138 °C, and a glass transition temperature at −125 °C [50]. This turned out to be a problem, as no sintering of individual PE beads was observed until reaching the melting point.

It was further attempted to melt the PE as droplets encapsulating the silicone oil, but this was not possible, due to the interfacial tensions, as discussed in section 2.2. The polyethylene formed melted droplets on the side of the silicone oil droplet, as seen in figure 3.6b. Thus, the polyethylene beads could not be

used to fabricate capsules in these experiments.

3.7.3 Polystyrene

Dynoseeds TS polystyrene beads from Microbeads AS were used for the experiments including polystyrene as a particle material. Polystyrene is a great insulator, and therefore follows the Taylor-Melcher flow, without altering the polarisation of the droplet. The polystyrene beads had a density of $1.05\,\mathrm{g\,cm^{-3}}$, and were colourless, transparent, and without surfactants or other active surface coatings. Polystyrene has a glass transition temperature of approximately 110 °C, but contrary to polyethylene, polystyrene has a significantly higher melting point, at 240 °C [50]. This allows the glass transition to be exploited easily, without the risk of melting the particles themselves.

Three different particle sizes were used, with diameters of 10 µm (Dynoseeds TS10), 20 µm (Dynoseeds TS20), and 40 µm (Dynoseeds TS40). The different particle sizes were probed to determine the structural strengths of the various sizes, along with the difference in ease of fabricating the capsules.

The polystyrene beads turned out to be the best material for fabricating the capsules with the previously described experimental setup. A SEM image of some 40 µm polystyrene beads after being heated to the glass transition temperature is shown in figure 3.7.

3.8 Safety measures

As these experiments included high temperatures, high voltages, and flammable materials, some safety measures had to be performed.

The fluids and capsule materials have flash points, which are temperatures where the media can spontaneously ignite if in contact with air. It was ensured that the samples were not heated to those temperatures while in contact with air, which for the oils was well above 200 °C. The boiling points of the fluids were also considered when a heating temperature was set, but as this temperature was much higher than the highest used for the heating plate (160 °C), no boiling was encountered.

The entire sample cell was covered in an acrylic glass box, which protected against potential bursts of oil, contact with the high voltage electrodes, and

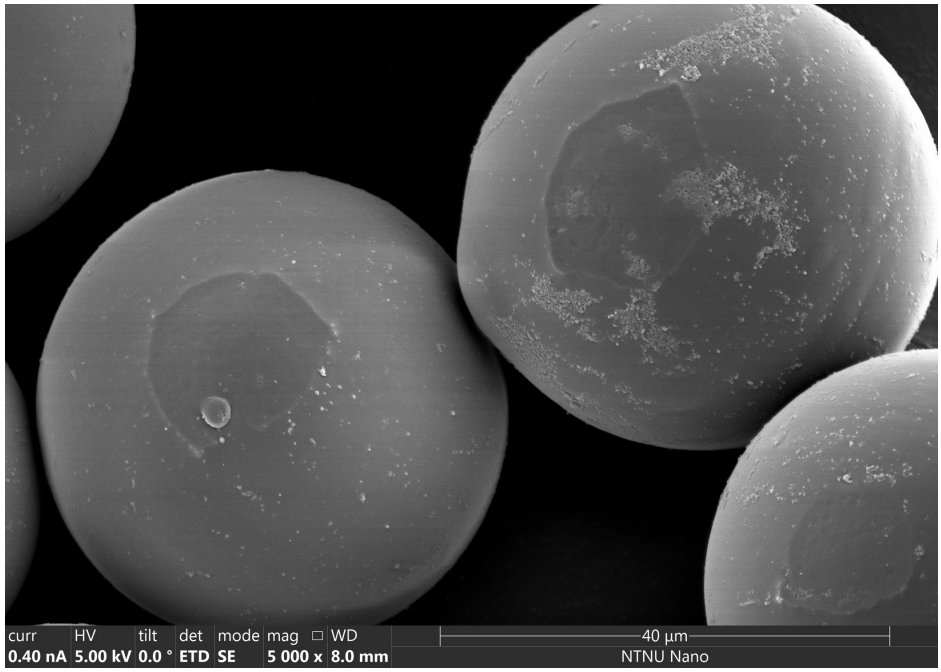

Figure 3.7: Closeup of polystyrene beads, after being heated to the glass transition temperature. While the beads were mostly highly spherical, some small surface bumps and size differences were observed. While the supplier lists the diameter as 40 µm, the spheres have diameters of 42.5 µm according to the SEM software.

general contact with the hot substances.

For further protection from currents through the body, the power source was connected to an electrical safety box, with a large off switch for easy access in case of emergency. The safety box also had a separate fuse against high currents. The entire setup for fabricating the capsules can be seen in the photo in figure 3.8.

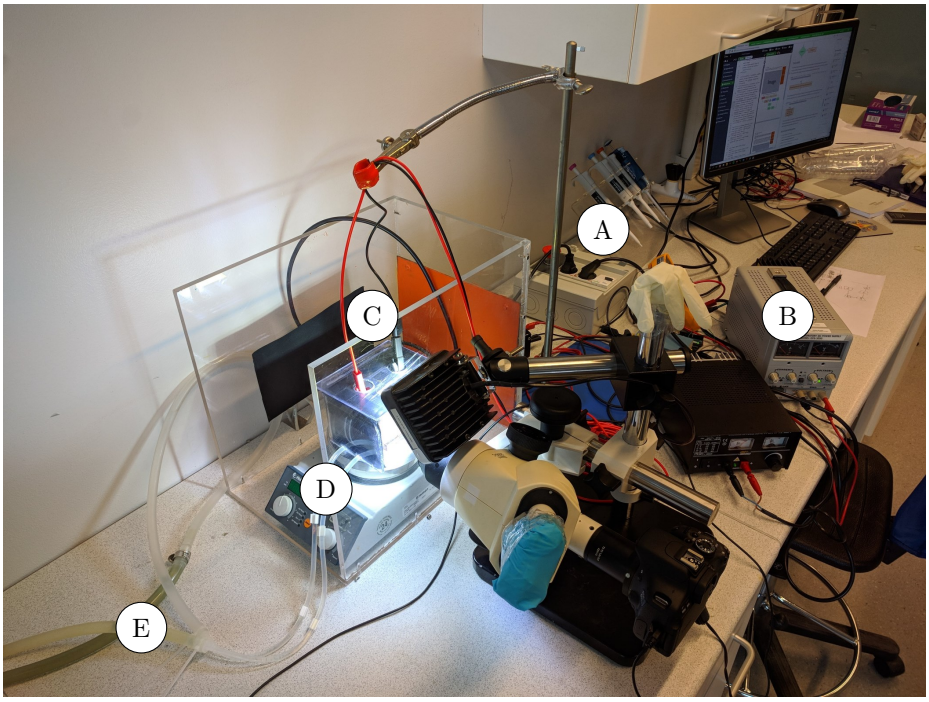

Figure 3.8: The setup on the lab used to fabricate the capsules at NTNU. The letters represent (A) the electric safety box, (B) the electric power source, (C) the crocodile clamps, (D) the heating plate, and (E) the tubing for the water-cooling system.

3.9 Experimental setup for analysing capsules

During two days in April 2019, experiments were conducted at Aalto University in Finland, where the goal was to examine the sintered capsules in greater detail than what was possible at NTNU in Trondheim.

3.9.1 Micropipette aspiration

The original experiment was to perform micropipette aspiration on the capsules to probe the structural integrity of the capsules my recording the deformations when a suctioning pressure is applied on the outer wall, as illustrated in figure 3.9. The capsules were in a Petri dish over an inverted optical microscope. The

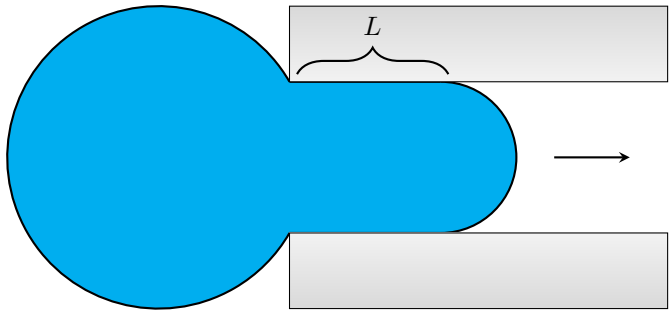

Figure 3.9: Illustration of micropipette aspiration, as performed at Aalto University in Finland. The droplet can either clear, covered by particles, or a gel or other soft material. The aspiration length L is measured visually as a function of time for a constant pressure difference.

Petri dish contained castor oil, which had been flushed through the tubing (left side of the figure).

Due to the very high viscosity of the castor oil, the pipe had a high fluid resistance, so that it took approximately 30 min to fill the entire pipe with castor oil even though the total volume of the piping was approximately 30 ml. The fluid resistance R_{F}, being the ratio between the applied pressure and the flow rate, was measured to be $R_{\mathrm{F}} = \frac{\Delta p}{Q} = 8.8 \times 10^5\,\mathrm{mbar\,s\,ml^{-1}}$ by finding the rate of change in the reciprocal of the flow rate as a function of applied pressure. Much lower ($\sim \frac{1}{1000}$) fluid resistance is possible if using less viscous host fluids, such as water, but this was not considered before leaving to Finland.

3.9.2 Mechanical testing

Another experimental setup was constructed while at Aalto University. A qualitative capsule crushing experiment was made, using tools at location, including glass plates, adhesive tape, plastic cuvettes, and a micrometer screw gauge. The setup, as illustrated in figure 3.10, was recorded by a microscopic camera connected to a computer. The micrometer screw gauge was lowered by 20 µm every 15 seconds.

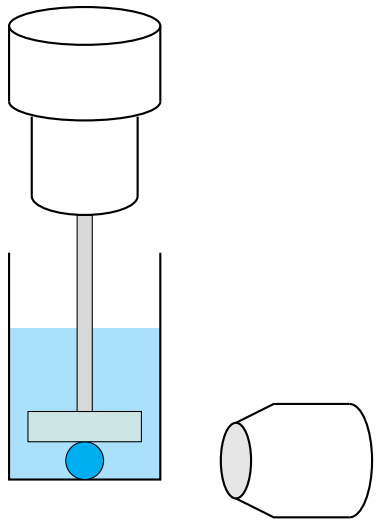

Figure 3.10: Illustration of capsule crushing experiment. The capsule is cyan, with the light teal plate being a glass plate, pushed down by the micrometer on the top. A microscope is positioned on the side. The plastic cuvette was filled with castor oil during the crushing experiment. This setup was constructed on location in Finland during the two day stay and was thus quite basic. While still giving consistent results and images, no quantitative data was recorded.

While the imaging data recorded was interesting, for similar studies in the future it is recommended to add a mass weight under the plastic cuvette, as this allows for the force exerted on the capsule to be measured, which vastly increases the usefulness of the data.

Chapter 4

Results

The results from this project can be summarised into several different parts, divided into four different sections in this chapter. These four sections are describing the different stages of the progression during the work performed over one year, each stage constituting a challenge that had to be overcome to progress to the next challenge. The first challenge was, and thus the first section, the production of droplets with particles. The second challenge was to find the correct material to fabricate a spherical rigid capsule. Third, when the capsule fabrication process was determined, the capsule properties were analysed. In addition, some results from an experiment on the side are included, as capsules with conducting beads were fabricated.

The first stage was completed relatively quickly, due to previous work presented in the doctoral thesis of Alexander Mikkelsen [26]. The next two stages took considerably more time, as new methods and setups had to be developed, and the results presented here are therefore more varied, with different approaches. When the correct material was found, the properties could be examined, but still with a sense of searching, as it was unknown how to perform the tasks.

A large portion of the results presented here are from two days of intensive work at the Department of Applied Physics at Aalto University, Finland in April 2019, where most of the material properties were investigated.

4.1 Fabricating arrested droplets

A droplet can be covered by particles, and when the droplet surface area is fully covered, we call the droplet "arrested", as the particles are fixed, unable to move

around on the surface.

By mixing the silicone oil with different fractions of particles, the particle coverage of a droplet was controlled. The mass ratio between silicone oil and the spherical particles was estimated with equation 3.1, but as mentioned in section 3.5, the actual ratio in the produced droplet was hard to control due to sedimentation and unevenness in the oil-particle sample holder. From equation 3.1, it is also apparent that the mass ratio is dependent on the intended droplet size, but as the droplet diameter was hard to control, this value was not fixed. To ensure a fully covered droplet, an excess of particles was added so that extra particles could be ejected from the Taylor-Melcher flow, although the host fluid itself consequently got more polluted by the ejected particles, inhibiting the view from the microscope. Droplets with different particle covering fractions can be seen in figure 4.1.

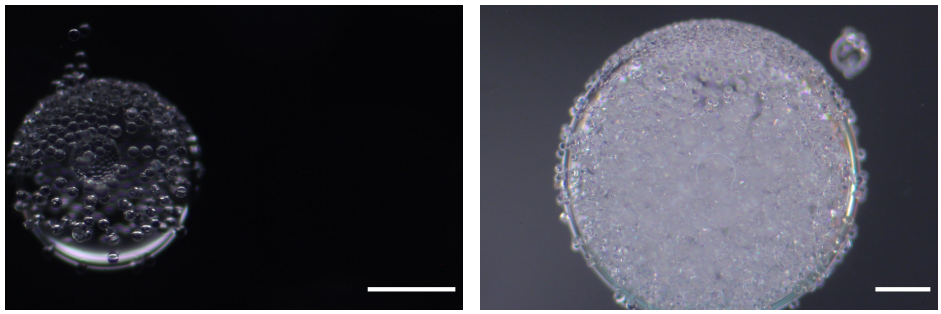

(a) (b)

Figure 4.1: Two droplets with different particle coverage. The left droplet (a) has a diameter of 0.6 mm, and the right droplet (b) has a diameter of 1.6 mm. The particles are polystyrene beads with a diameter of 40 µm, and the scale bars represent 300 µm for both photos.

Fully covered droplets were fabricated, with particle packing close to hexagonal (the densest sphere packing on a flat surface), as can be seen in figure 4.2. The cut-out in the figure shows that the packing is hexagonal locally, but with several dislocations and grain boundaries, as a perfect hexagonal packing is not possible on a curved surface, in addition to the particles not being perfectly isotropic.

When applying an electric field, Taylor-Melcher flow is induced, as shown in figure 4.3a. This flow is similar to the theoretical streamlines shown in figure 2.6, and as confirmed in previous experiments [32, 42]. The droplet deformation in the image is approximately $D \approx -0.020$, while the deformation calculated from equation 2.31 is $D = -0.0088$. This discrepancy will be discussed later in section 5.1.

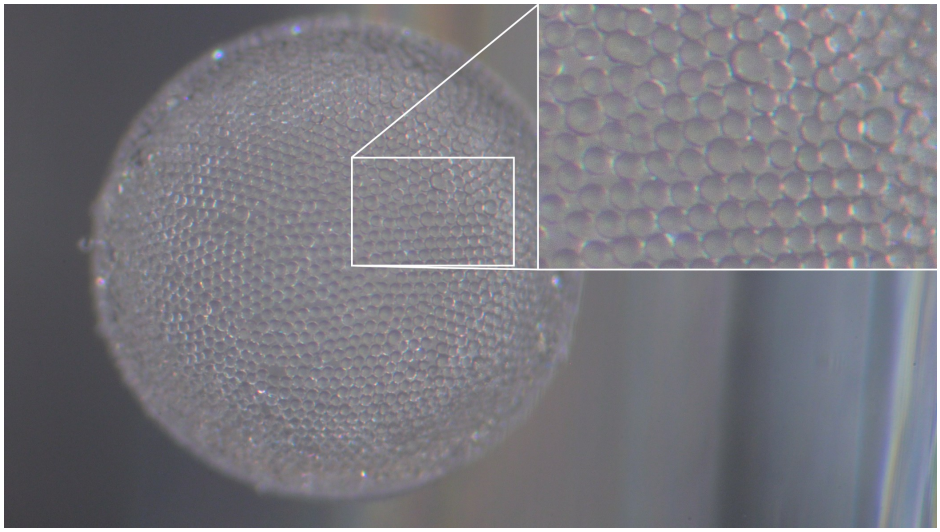

Figure 4.2: A photo of an unsintered droplet with a diameter of 1.6 mm. The drop surface is fully covered by 40 µm polystyrene beads. From the cut-out, it is apparent that the beads themselves are not completely monodisperse but vary somewhat in size. The packing is locally forming hexagonal packed patches, with dislocations in boundaries.

4.2 Sintering of wax and polyethylene

4.2.1 Properties of wax coated droplets

After producing the "soft", unsintered armoured drops, the next goal was to sinter the armour into rigid capsules. The first idea was to use an armour material with low melting point, so that the armour could be melted, form a capsule as a double emulsion, and then be cooled back down to form a solid capsule. These first experiments made use of Hampton Research Capillary Wax, which is listed with a melting point of 79 °C. The wax, which originally from the supplier was formed as sticks with a diameter of roughly 6 mm, was crushed with a stone grinder. It proved to be difficult to create equal sized particles, as previously shown in figure 3.6a. Nevertheless, oil-wax samples were created of different mass ratios, and droplets were produced. The electric field was switched on and left on for approximately 5 min to move the wax particles to the drop surface. When the droplet was visibly empty, and all the wax particles were at the surface, the electric field was switched off, and the heating plate was switched on to melt the wax particles into a layer.

Sedimentation of the droplets causes experimental problems. Many of the

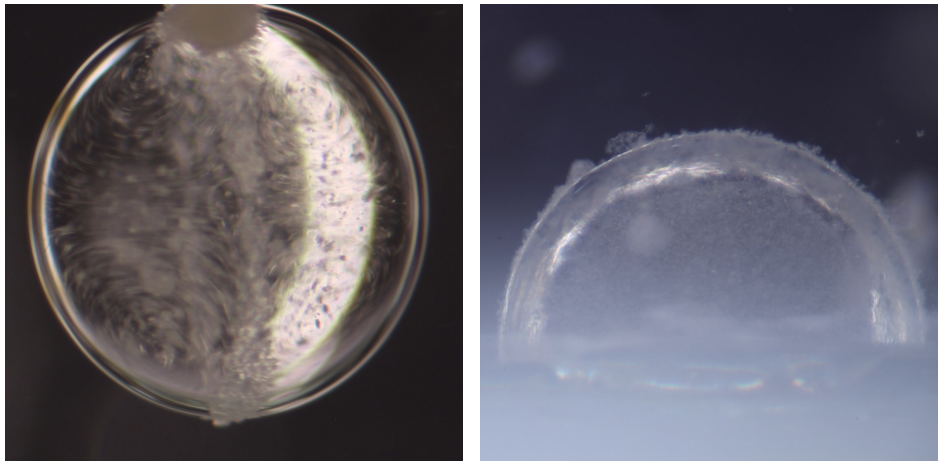

(a) (b)

Figure 4.3: Photos of droplets with wax. (a) shows a droplet of silicone oil containing wax particles. The relatively long camera exposure of 0.6 seconds reveals the Taylor-Melcher fluid motion inside the droplet, similar to the flow shown in figure 2.6. A vertical ribbon is building up on the surface of the droplet from particles being ejected to the surface and moved to the drop equator due to the fluid motion inside and outside the droplet. (b) shows a half-capsule coated with heat cured wax, at the bottom of the sample cell. Wax "hairs" can be observed at the rim of the capsule. The wax coating is approximated to be less than 50 µm and was too thin to provide any structural integrity when attempting to relocate the capsule.

droplets sediment during the experiments, and adhere to the bottom of the cell, forming half-spheres. Later, when the cell is heated, another portion of the droplets are destroyed or altered due to thermal convection in the sample cell, moving the droplets around chaotically. Of the surviving droplets after heat curing, most were half capsules covered with wax only on the top, as can be seen in figure 4.3b.

It was attempted to suck up the capsule with a pipette, which destroyed the capsule, as the solid wax capsule was too thin and weak to provide any substantial structural integrity to the oil droplet inside. As the wax was too weak, experiments were promptly changed to use polymer particles as coating.

4.2.2 Properties of polyethylene coated droplets

Using polyethylene (PE), the intention was to sinter the capsules from reaching the glass transition temperature (described in section 2.6). Both PE beads and

PS beads were available at the lab, but as the melting point of PE is listed as being 138 °C, compared to 240 °C for polystyrene (PS), the hope was that it would be easier to sinter PE beads than PS beads, using the glass transition temperature [50]. The glass transition temperature for PE is listed as being −125 °C in the same reference, which was deemed improbably low, as the general mechanical properties for the PE beads and PS beads seemed similar. This will be discussed later in section 5.2. Thus, it was assumed that the glass transition temperature of PE is substantially lower than that of PS, and therefore easier to fabricate capsules without creating as much heat convection as for PS.

The temperature behaviour of PE coating is radically different from the temperature behaviour of PS coating. It turned out that PE did not reach any glass transition before reaching the melting point, and the PE beads thus not sintering before melting into liquid PE. A photo of such melted polyethylene is shown in figure 3.6b. In most cases, the particle covered droplets either did not sinter (no change after heating), or melted completely, forming large blobs of melted PE, without substantially covering the droplet. Only in some cases, roughly 10 % of experiments, the heat was such that the particles only partly melted, forming a cover of the droplet. The temperature of the oil was difficult to control, as the heat from the heating plate had to transmit through both the copper plate and the sample cell with oil. Thus, the resulting state of the capsules was unpredictable.

One case of partly melting can be observed in figure 4.4. There, the beads have partly melted. The red beads are visible on the left side, and the rest of the droplet is covered by a thin layer of colourless translucent part of polyethylene melt.

Due to the inability to accurately control the melting process, failure to sinter the beads around an oil droplet, the polyethylene melt forming droplets instead of coating the oil as a double emulsion, the polyethylene experiments were halted. Some more polyethylene experiments were conducted with metal beads, which are described in section 4.4. After cooling the melted polyethylene back to room temperature, the melt was examined by applying mechanical force, and showed remarkable strength compared to wax, which was promising for further experiments with polymers.

4.3 Sintering polystyrene particles into capsules

As the polyethylene capsules did not successfully form spherical capsules, polystyrene was chosen as capsule material. Polystyrene has a well-defined glass transition temperature of approximately 100 °C, and a substantially higher

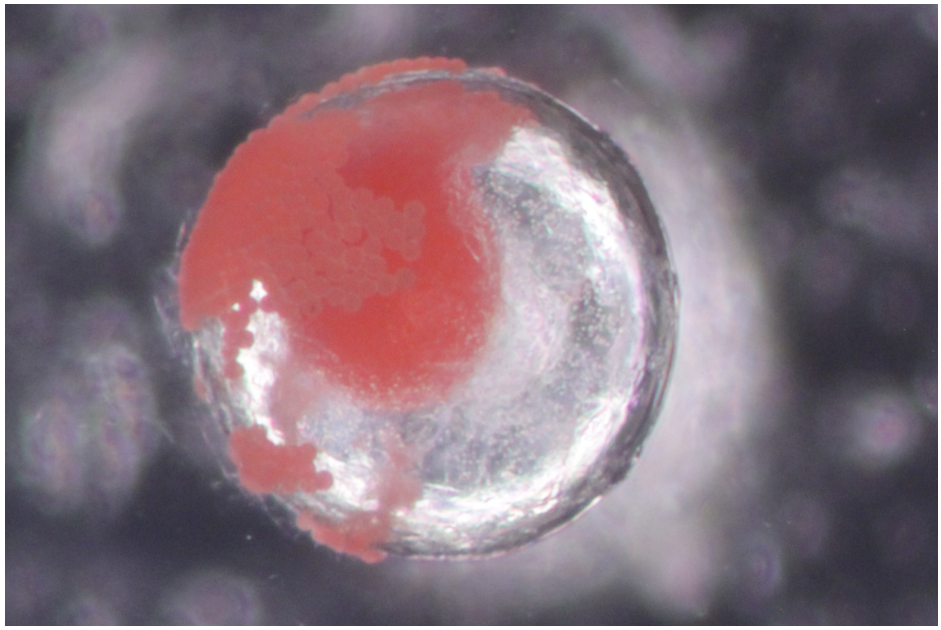

Figure 4.4: A droplet with polyethylene beads in red. The particles have partly melted, as they are formed into smaller sintered patches, and formed a thin transparent coating on the rest of the droplet. The droplet diameter is 1.3 mm, and the bead diameters are 90 % in the range 45 µm to 53 µm, according to the supplier.

melting point of 240 °C [50–52]. By making droplets of silicone oil mixed with polystyrene beads in the sample cell with castor oil, applying an electric field of 200 V mm^{-1} for approximately five minutes, heating to 100 °C, and cooling down, successful capsules of polystyrene beads were fabricated, covering the silicone oil. This process is illustrated in figure 4.5. A capsule from this process is presented in figure 4.6a, while a SEM image of a capsule fragment is presented in figure 4.6b. The number of capsules produced for each run of the process depends on the number of droplets injected into the castor oil, together with the ratio of destructed capsules from thermal convection and the random paths the droplet took during the convective flow. More than half of the produced droplets either attached to the cell walls, or lost particles when moving in the thermal convection flow. These factors together participated in either deforming the droplets or ejected particles from the surface, so that only parts of the droplets were coated in polystyrene. In addition, a small portion of droplets ruptured at the surface, destroying the droplet and its coating completely. A partial capsule has the same mechanical properties locally as a full capsule, so several results presented here will be from partial capsules.

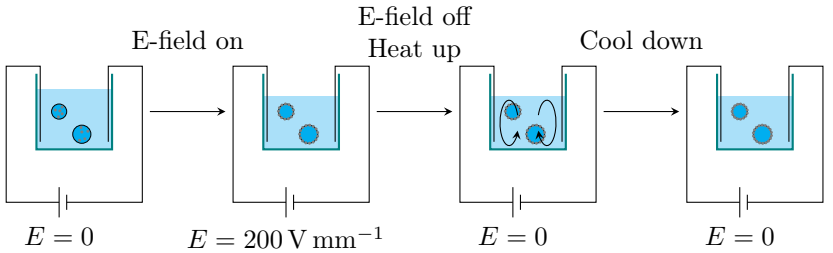

Figure 4.5: Illustration of procedure for fabricating capsules.

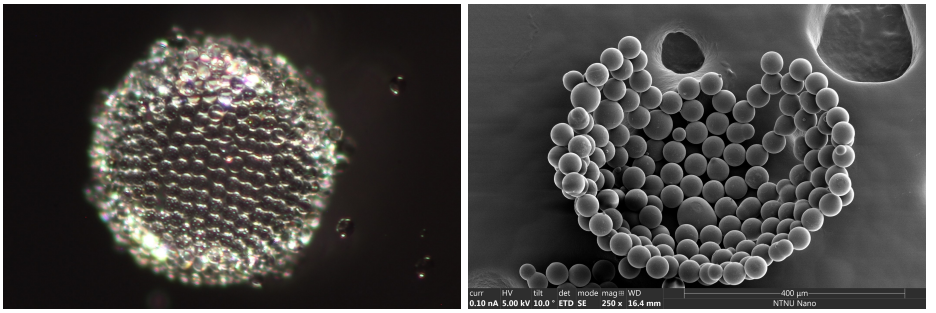

(a) (b)

Figure 4.6: (a) Silicone droplet fully covered by polystyrene beads. The beads are sintered by heating the droplet to approximately 100 °C, above the glass transition temperature of polystyrene. This capsule is approximately 650 µm in diameter.
(b) A fragment of a previously full capsule, observed in a SEM. The fragment width is approximately 550 µm.

4.3.1 Effects of different particle sizes

Polystyrene particle sizes of 10 µm, 20 µm, and 40 µm were used in these experiments to probe the mechanical properties of capsules with different sized polystyrene beads. Capsules of 40 µm beads were easily made, with a low grade of particles being ejected from the drop surface (figure 4.7a). Experiments with 20 µm beads were more prone to failure, as capillary binding is dependent on particle size, resulting in fewer covered droplets (figure 4.7b) [53]. Using 10 µm particles did not yield any complete capsules. All the droplets were depleted of beads by drag from the thermal convection. Only a thin sliver of beads were left on the side of the droplet not facing the convection fluid flow, as it is a stable stagnation point of the fluid flow, the low fluid velocity allowing the capillary binding to retain the particles on the oil-oil interface (figure 4.7c).

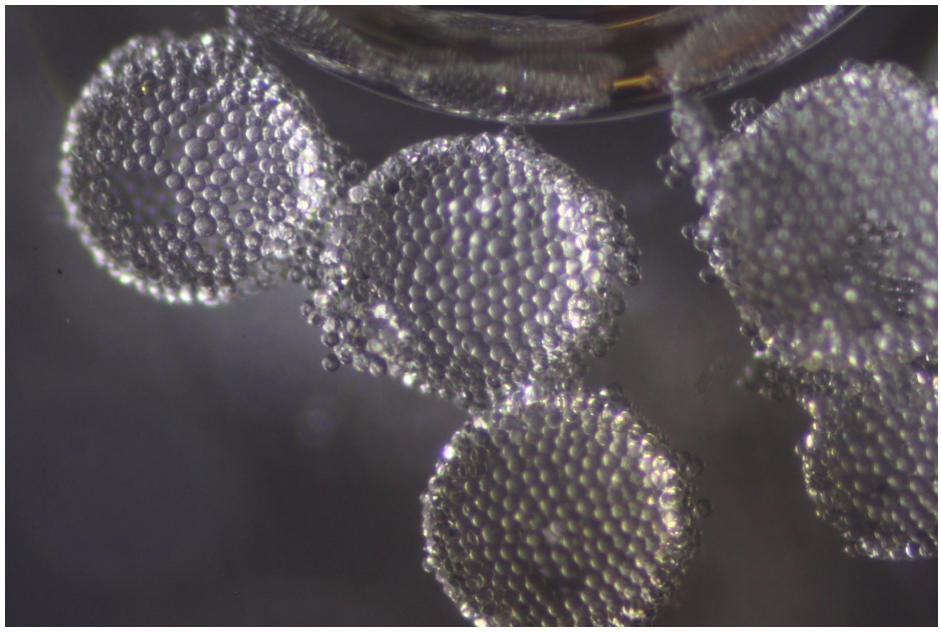

(a) 40 µm polystyrene beads. Capsule diameters are approximately 600 µm.

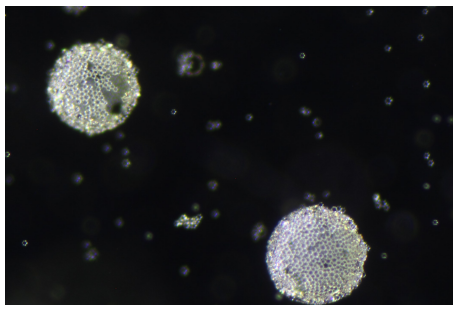

(b) 20 µm polystyrene beads. Capsule diameters are approximately 400 µm (left) and 450 µm (right).

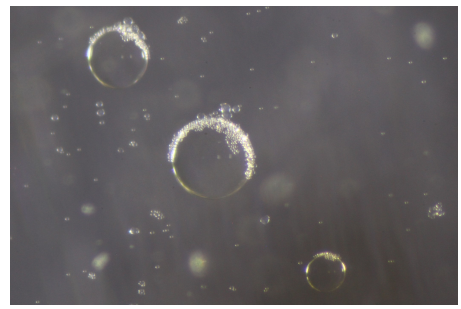

(c) 10 µm polystyrene beads. Droplet diameters are approximately 250 µm (top left), 350 µm, and 150 µm (bottom right).

Figure 4.7: Comparison of different polystyrene bead sizes, all photos after the sintering process. Image (a), with 40 µm beads, show generally clean capsules. Even though some holes appear (top left), it was generally easy to produce full capsules.
Image (b), with 20 µm beads, show more holes than for 40 µm beads. There are noticeably more beads ejected from the drop surface, and it was in general a lower rate of success for producing capsules with 20 µm beads than 40 µm beads.
Image (c), with 10 µm beads, show droplets with almost no beads on them, as they have almost completely been separated from the droplets. This is due to the convective flow, which has dragged the beads off the drop surface, leaving a small portion left on the side, where the droplet itself shielded from the flow.

In general, the 40 µm beads were the easiest to work with, and gave the cleanest results: The capsules were more successful, and the waste of beads was lower. The 40 µm bead capsules also showed the greatest strength.

Of the sintered structures using 20 µm over 0.5 mm in size that were brought to Aalto University, Finland, no complete capsules survived the journey, being brought in a cylindrical glass container, diameter 2.5 cm and height 4 cm, half full of castor oil. The largest surviving piece, and the only one to be probed at Aalto University, was a 900 µm by 500 µm chunk of sintered 20 µm beads. The chunk was not spherical, not hollow, and did not provide any relevant results for this thesis. Therefore, all remaining results are with 40 µm polystyrene beads.

4.3.2 Properties of capsules with 40 µm beads

When fabricating the capsules, the resulting properties of the capsules were strongly dependent on the distribution of the droplet in the sample cell. Both the silicone oil and the polystyrene beads had densities higher than the surrounding castor oil, and thus, some droplets quickly sedimented to the bottom of the cell and were attached to it due to surface tension. This permanently perturbed the shape of the capsule to a half-sphere, while also inhibiting the polystyrene beads from covering the downside of the droplet, as the particles had an affinity to the oil-oil interface. Smaller droplets were, however, easier suspended in the liquid, as the sedimentation rate is proportional to the radius of the droplet [54, 55]. This made it easier to work with smaller droplets (sub-millimetre diameter) than large droplets.

Engaging the electric field did not significantly induce a displacement of the droplets. The droplets do get electrically polarised, and the surrounding fluid is brought to motion, so that two droplets could attract each other. But this effect was weak, as the time for a uncoated drop pair to contact is proportional to the initial separation to the fifth power, and is well over 100 s for drops separated by 5 radii [56]. For coated droplets, the droplet surface fluid velocity is decreased, and thus the time to contact is further increased [57]. Therefore, the attraction was only noticeable for droplets less than a couple of droplet radii between each other for an electric field of $200\,\mathrm{V\,mm^{-1}}$.

The thermal convection together with the sedimentation had the greatest influence on the droplet motion. When heating without the electric field active, heat convection was induced, with hot fluid rising on the sides, and sinking in the centre, as shown in figure 4.8a. After approximately 5 minutes, when the temperature in the cell had stabilised, the flow patterns changed to a circular motion, with occasional vortexes in the corners of the cell, as shown in figure 4.8b. When the oil was hot, an applied electric field induced an unstable flow

in the fluid, as shown in the consecutive photos in figures 4.8c, 4.8d, and 4.8e. We can see that the vortexes are changing over the 20 seconds between the three photos, for example in the top centre of each of the three images. When the electric field was turned back off, the fluid motion settled back to a stable flow in a matter of seconds, as seen in figure 4.8f. This flow was again unchanged over time.

The unstable convective flow is assumed to be due to the viscosity of the fluids being reduced by the increase in temperature, increasing the electrohydrodynamic shear-stress interactions in the system, which are inversely proportional to the viscosity [33].

When attempting to sinter using heat while the electric field was active, the polarised droplets were pulled towards the cell sides of ITO, when they were close enough for the Coulomb forces to overcome the viscous forces caused by the convective flow. As the walls were then charged, and the droplets had opposite charge on the wall-facing side, the droplets sedimented at the side of the sample cell. The additional vortexes, as can be seen for example in the bottom left of figure 4.8d, probably also contributed to a reduced drag on the capsules, as the flow velocity in that corner is reduced. The polarisation of the capsules, and the high concentration of capsules at the ITO walls, made the capsules fuse together into larger clusters, as seen in figure 4.9. These clusters were not easily separated, and such attempts most often ended in rupturing the capsules and leaving fractures of other capsules on the sides of isolated samples (as is visible e.g. in figure 4.15). This problem was easily omitted by turning off the electric field while heating.

After sintering, the capsules with droplets inside were extracted using a suctioning syringe pump. A metal syringe of inner diameter 1.5 mm was manually directed towards the capsules to let them be extracted. The flow rate of the syringe pump was varied, and values up to $100\,\mu L\,min^{-1}$ were used. After removing all the capsules, the syringe pump was switched from infusing to injecting mode, with the same flow rate, only in opposite direction. During this process, no capsule deformation was observed. The capsules could then be deposited into empty Petri dishes, or into a fluid like ethanol or water.

When depositing, there was always some castor oil adhering to the capsules. This castor oil was attempted removed, both by suctioning with a finer tip, and by cleaning with ethanol. As the castor oil according to the supplier had a boiling point of 313 °C, it was not feasible to let it evaporate. The oil was thus best removed by first removing as much as possible of the oil with the syringe pump, and then by cleaning the rest with ethanol, as castor oil is completely soluble in ethanol [58], and polystyrene is insoluble in ethanol [59–61].

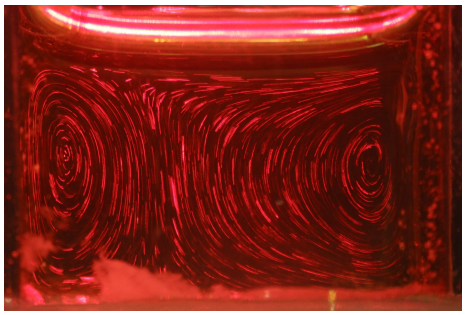

(a) $E = 0\,\mathrm{V\,mm^{-1}}$. $T \approx 80\,^{\circ}\mathrm{C}$.

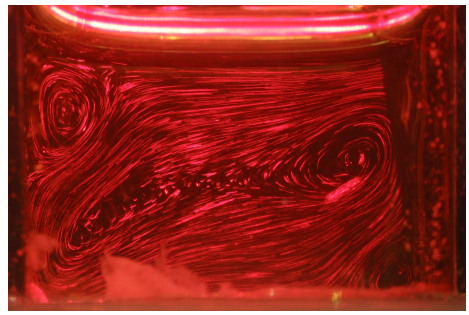

(b) $E = 0\,\mathrm{V\,mm^{-1}}$. $T \approx 95\,^{\circ}\mathrm{C}$.

(c) $E = 200\,\mathrm{V\,mm^{-1}}$, 15 s after initiation. $T \approx 95\,^{\circ}\mathrm{C}$.

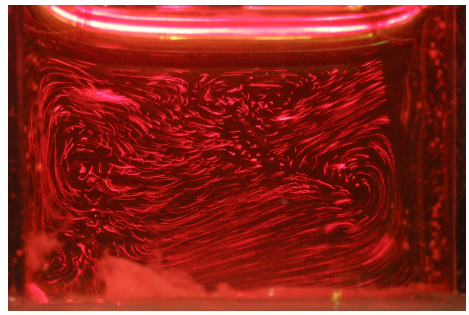

(d) $E = 200\,\mathrm{V\,mm^{-1}}$, 25 s after initiation. $T \approx 95\,^{\circ}\mathrm{C}$.

(e) $E = 200\,\mathrm{V\,mm^{-1}}$, 35 s after initiation. $T \approx 95\,^{\circ}\mathrm{C}$.

(f) $E = 0\,\mathrm{V\,mm^{-1}}$, 15 s after being turned off, and 30 s after (e). $T \approx 95\,^{\circ}\mathrm{C}$.

Figure 4.8: Comparison of convection with and without an electric field. The electric field was turned on after image (b) and turned off after image (e). The electric field is applied from left to right, across the 15 mm sample cell. The containing oil is castor oil, and the tracer particles are the 40 µm polystyrene beads. Image sequence captured by illuminating with a laser sheet, scattering off the polystyrene beads. All images are 4 second exposures.

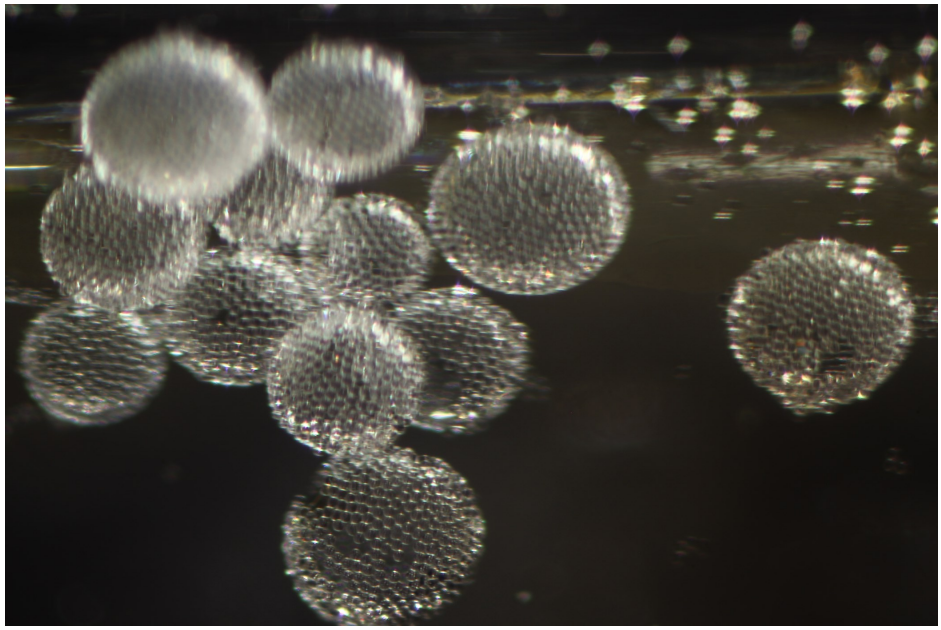

Figure 4.9: Cluster of capsules fused together, as a result of sintering with heat while the electric field was on. These clusters could not be separated into individual capsules without rupturing the wall of the capsules. Capsule diameters range from 0.5 mm to 0.7 mm. The image is distorted by the host oil meniscus, as the capsules are at the side of the sample cell.

4.3.3 Packing density

The amount of particles on the droplet surface was dependent on the initial number of particles inside the droplet when creating it inside the castor oil. The electrohydrodynamic flow propelled the polystyrene beads toward the surface of the droplet, where they were trapped by the interfacial tension. If the number of particles inside the droplet was too low to cover the surface, as governed by equation 3.1, no measure could be taken to increase the number of particles inside/on the droplet. If the number of particles was too high, the excess particles were ejected from the droplet, resulting in the right amount of particles to fully cover the droplet surface. Typically, when the droplet was moved around in the sample cell from thermal convective flow, a small number of particles would be ejected from drag. Thus, the sintered capsules typically had a lower packing density than their pre-sintered ancestors.

For the unsintered droplet in figure 4.2, the packing density is high, and is close to a perfect hexagonal circular packing fraction in many areas, i.e. close to $\frac{\pi\sqrt{3}}{6} \approx 0.907$ in some regions. For the sintered capsules, however, the packing

density for small cut-outs ranged from approximately 0.78 to 0.88. Small patches were still close to hexagonal packed, as can be seen in figure 4.10, but the dislocation rate was higher for sintered capsules than their unsintered counterparts. The capsules also often had empty patches, reducing the total packing density,

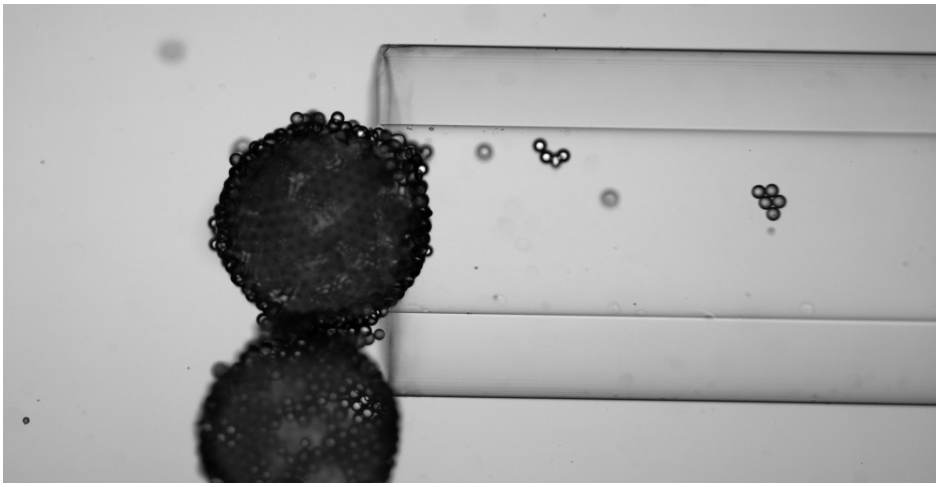

Figure 4.10: Local hexagonal packing can be observed in the rightmost fragment inside the tube. Empty patches up to 100 µm without particles are visible on the capsules. The inner diameter of the tube is 580 µm, the particle size is 40 µm, and the capsules have diameters of 670 µm (top) and 620 µm (bottom).

as is visible in figure 4.11.

The walls of the capsules consisted mostly of a monolayer of particles, as can be seen in the previous pictures in this chapter (figures 4.6, 4.7a, 4.7b, 4.9, 4.10, 4.11). Some particles are clearly displaced from the droplet interface but are still attached to the capsule. These outer particles are mostly residues from capsules that had been fused to the capsule, and broken apart, leaving some particles behind.

4.3.4 Emptying the capsules

When forming the capsules on the silicone oil droplet, the finished sintered capsules consequently enclosed the oil droplet. For incomplete capsules, it was easy to separate the capsule material and the oil droplet. But for complete capsules, due to the small gaps between the sintered beads, mostly smaller than 0.1 mm, it was not feasible to use a syringe to suck out the oil from capsule. Attempts at

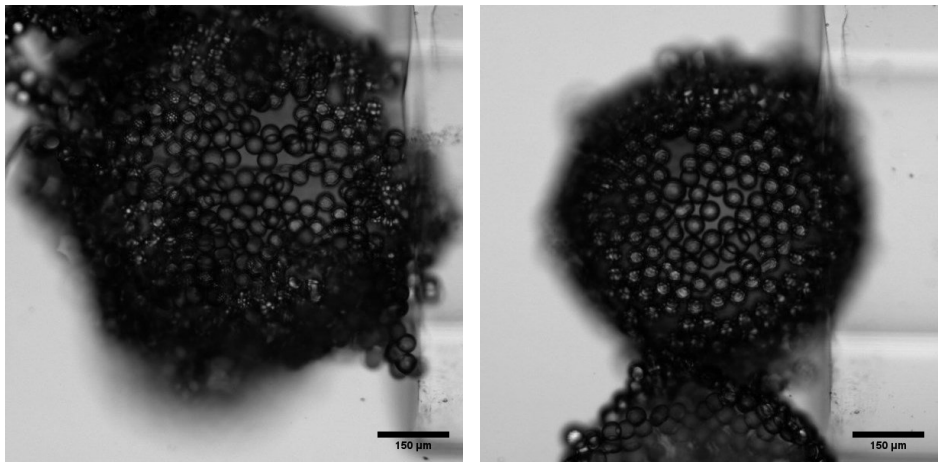

(a) (b)

Figure 4.11: Closeups of two sintered capsules. (a) shows several spots without beads, indicating inefficient packing. This photo is after capsule evacuation and fracturing from pressure driven flow, but this only affected the side facing the tube. (b) shows a denser packed capsule, with close to hexagonal packing on the upper right part of the capsule. Capsule diameters are approximately (a) 750 µm and (b) 630 µm. The particles are 40 µm polystyrene beads for both capsules.

dissolving the silicone oil were unsuccessful, as there was not any available solvent that could dissolve the silicone oil, without harming the polystyrene bindings in the process. Adding the droplets in water did not improve the situation, as some enclosing castor oil would follow, and was impossible to fully remove due to surface tension.

The best way to remove the inner droplet, isolating the capsule itself, was found by an accident, while withdrawing oil with a syringe pump, where the syringe tip inner diameter was smaller than the droplet. Using a low rate of withdrawal, the capsule with the droplet inside was pulled to the tip, where it was stopped by tip diameter being too small. When the withdrawal rate was low enough to not break the capsule, the droplet inside was sucked through the capsule wall, isolating the capsule itself with castor oil both inside and outside the capsule. This method was further inspected in micropipette aspiration experiments at Aalto University in Finland.

Using this method, the droplet inside was found to escape for flow rates of roughly $0.05\,\mathrm{mm^3\,s^{-1}}$ and higher. This value is strongly dependent on the size of the droplet enclosed, as the host fluid flow must be able to pass around and into the micropipette, and as the Laplace pressure increases inversely proportional to the droplet radius. But the first capsule fracturing occurred from flow rates of $0.20\,\mathrm{mm^3\,s^{-1}}$ and higher, so there was no difficulty in getting the capsule drop securely ejected without breaking the capsule itself in the process. One such instance of capsule depletion is shown in figure 4.12. A video of the entire depletion is available online at the web address `http://folk.ntnu.no/fossumj/asbjorn/CapsuleDepletion.avi`, and the sequence is also displayed in appendix B.

The emptied capsule could then be either moved to a different phase or isolated completely. Empty capsules were transferred to ethanol, where residue castor oil could be dissolved. Then, the capsule could be further transferred to water, or air, as ethanol both is soluble in water, and evaporates quickly. This allowed for example the fragments to be examined in SEM, as is shown in section 4.3.6.

4.3.5 Mechanical properties of the capsules

The strength of the sintered capsules was found to depend on several factors. One of the factors determining capsule strength was the effectiveness of packing. Higher packing density implies more particles per interface area, a higher number of contact points between the polystyrene beads, and thus a higher mechanical strength.

The packing density thus also influenced how well the capsules resisted pressure

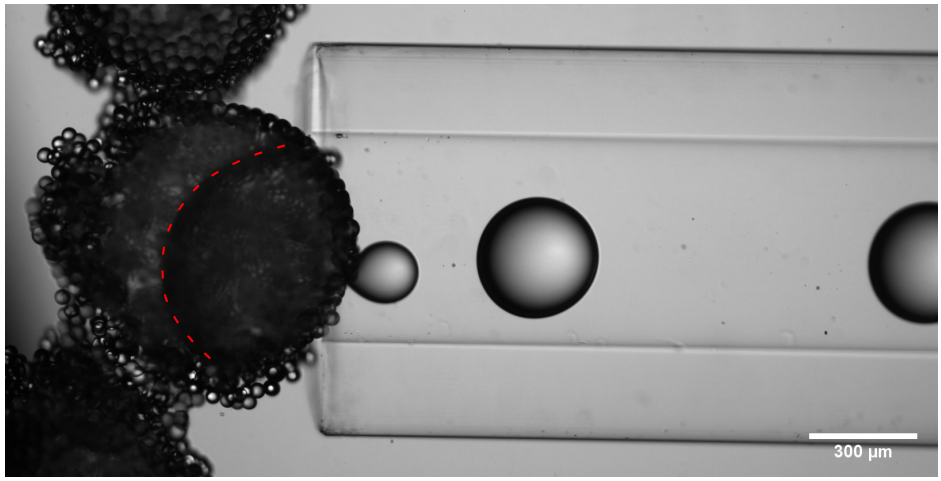

Figure 4.12: Depletion of enclosed oil for a sintered capsule. The resulting droplets were highly monodisperse in the beginning, but fluctuated more when the encapsulated oil reservoir was closer depletion. The encapsulated droplet itself is visible inside the capsule, and the edge is highlighted with a red dashed line. Capsule diameter is 825 µm, and droplet diameters for the two free droplets are both 330 µm.

driven flow. The setup for micropipette aspiration experiments at Aalto University in Finland relied on a flow from pressure difference, from having a lower pressure in the end of the tube compared to the opening in the Petri dish with capsules. Originally intended for soft droplets, the setup was for measuring the aspiration length as a function of time with constant pressure, which could then have been used for calculating Young's modulus for the material [62]. But due to the gaps in between the polystyrene beads, the pressure induced flow was let straight through the capsule. This fluid flow was then instead used to get a measure of the strength of the capsule. Slowly increasing the pressure difference, the response of the capsule was recorded.

The capsules did not deform elastically to any noticeable extent, as they were too rigid, and too brittle for that to happen. The capsules themselves did not show any response to increased fluid flow, until they suddenly fragmented, where patches fell off. The fracture events are listed in the scatter plot in figure 4.13. As can be seen in the scatter plot, the capsules never fractured or deformed below $0.22\,\mathrm{mm^3\,s^{-1}}$. For these measurements, the pressure difference (and as a result, the fluid flow) was slowly decreased. The pressure was adjusted from ambient (1 bar) down to 0 bar (vacuum), with steps of 1 mbar. Typically, the pressure was slowly increased in the beginning of each experiment, and as the experiment proceeded, without any visible change in the capsule, the pressure increase was turned up with higher intervals.

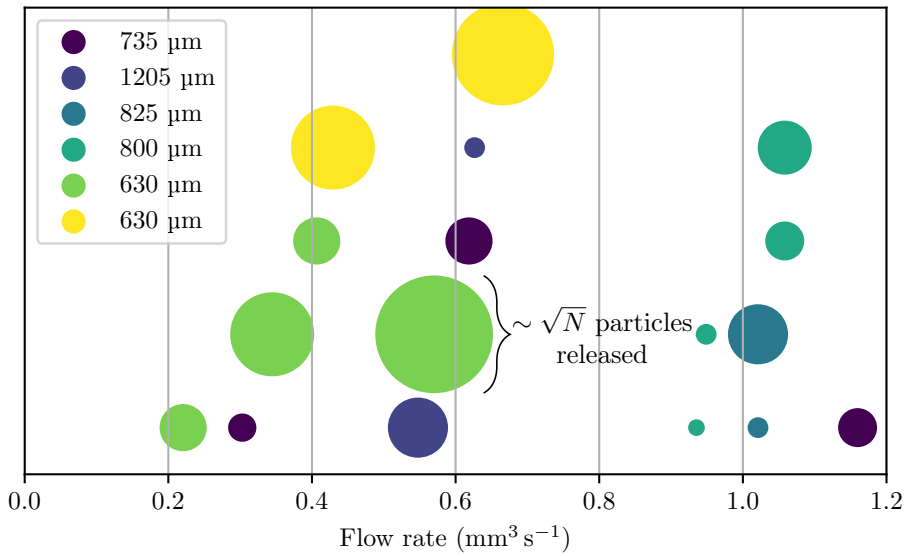

Figure 4.13: Scatter plot of fracture events, with the pipe castor oil flow rate shown on the x-axis. This is thus the amount of fluid being suctioned through the capsule. Each separate colour is a separate capsule, as can be seen in the figure legend, showing the capsule diameters for the specific capsules. The circle sizes indicate the estimated number of polystyrene beads being torn away of the capsule for each event, with the smallest circles being < 10 particles, and the largest being up to 200 particles. Polystyrene beads of size 40 µm were used for all these capsules.

An example of this was for the 825 µm capsule, which gives an estimated enclosing volume of 0.29 mm^3. The capsule was first emptied of silicone oil by setting the pressure to -40 mbar, which created a fluid flow of approximately 0.05 mm^3 s^{-1}. When the capsule was empty, the pressure was set back to ambient (0 mbar, and then suddenly down to -900 mbar, or a fluid flow of 1.06 mm^3 s^{-1}. This led to the capsule fracturing into several pieces, as two still frames from the event shows in figure 4.14.

Although this was a limited number of data points, it shows that the sintered polystyrene bead capsules can withstand some fluid flow passing through them, and that they do not deform in the process. The minimum fluid velocity required in these limited experiments was 0.22 mm^3 s^{-1}. All capsules in these experiments had varied sizes and packing, so while the tests are inconclusive, they show the possible great strength of the capsules.

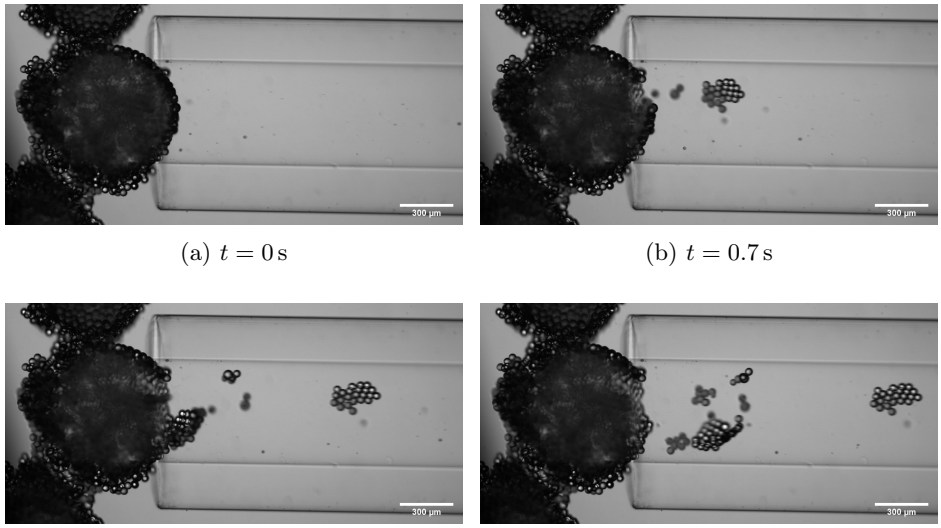

(a) $t = 0\,\mathrm{s}$ (b) $t = 0.7\,\mathrm{s}$

(c) $t = 1.6\,\mathrm{s}$ (d) $t = 2.1\,\mathrm{s}$

Figure 4.14: Capsule fracturing event, where a capsule ruptured due to a sudden pressure change, from 0 mbar to −900 mbar, inducing a fluid flow change from $0\,\mathrm{mm^3\,s^{-1}}$ to $1.05\,\mathrm{mm^3\,s^{-1}}$. The four pictures show before and after the rupture, 2.1 s apart. This is the same capsule as in figure 4.12. The capsule was fused together with one other capsule on each side, but this is not believed to have had an impact on the local fracturing itself.

The influence of an encapsulated droplet

As described in section 4.3.4, it was possible to remove the droplet inside the capsule. This droplet removal had great impact on the strength of the capsule, as the surface tension of the droplet inside contributed in resisting mechanical deformations. Also, the droplet helped the particles stay spherically shaped by trapping the particles on the oil-oil interface even after the capsule itself got crushed to pieces, returning the sintered capsule to a soft armoured droplet. This armoured droplet had some mechanical strength entirely from droplet surface tension, compared to no structural integrity for a completely crushed empty capsule, which would collapse if crushed under a too high force.

The capsule, either with a droplet inside or without, was placed in a 1 cm square cuvette (see figure 3.10), filled with the same host medium as in the capsule fabrication process: castor oil. A small glass plate was attached to a micrometer screw, which was lowered 20 µm every 15 s. After deforming the capsule, the

glass plate was lifted.

For a capsule without a droplet encapsulated, it was crushed from the top down, with the top being destroyed, while the bottom was still intact. When the glass plate was lowered far enough down, the capsule split into fragments, folding outward. When the plate was lifted afterwards, the capsule was stretched, due to the viscous forces in the host fluid. The separate fragments were still sintered, but loose from each other. This is all shown in figure 4.15.

Conversely, a capsule with an encapsulated droplet fragmented all over immediately as the droplet inside would deform equally on the top and on the bottom. When the plate was lifted, the capsule still appeared intact, even though the fragments were loosely attached to the surface of the droplet. To severely detach fragments from the droplet, the capsule-droplet combination had to be compressed down to approximately 1/3 of the original height. This is shown in figure 4.16.

From the images in figure 4.15 and 4.16 it is clear that the capsules are brittle, no matter if the capsules are encapsulating droplets or not. But for the ones encapsulating droplets, the capsules are almost always returned to an apparent original state, unless the capsule is heavily compressed, so that the capsule is beyond repair of the supporting droplet Laplace pressure. This means that if an object is put inside the capsule, a capsule with a droplet would sustain much more injury than a capsule without a droplet. It should still be noted that the colloidal armour from the fractured capsule is still significant in aiding the structural integrity of the capsule-droplet combination, as has been shown in other experiments where droplets with unsintered colloidal armour can resist two coalesced droplets from fusing to one spherical droplet, but instead form an asymmetric arrested capsule [8, 63].

4.3.6 The sintering process

The glass transition temperature is commonly defined as the temperature where the dynamic viscosity of a material crosses $10^{12}\,\mathrm{Pa\,s}$ (see section 2.6 for more detail). Rising the temperature over the glass transition temperature reduces the viscosity, and vice versa. Thus, to define a point where two polymer beads will sinter, is difficult. Previous experiments show that heating polystyrene to the glass transition temperature gradually fuse the particles together, depending on how long the heating is retained [64].

With this knowledge, and a glass transition temperature of estimated 100 °C for polystyrene [50], the heating plate was set to 150 °C, typically resulting in a measured temperature in the sample cell in the range of 90 °C to 100 °C. The heating

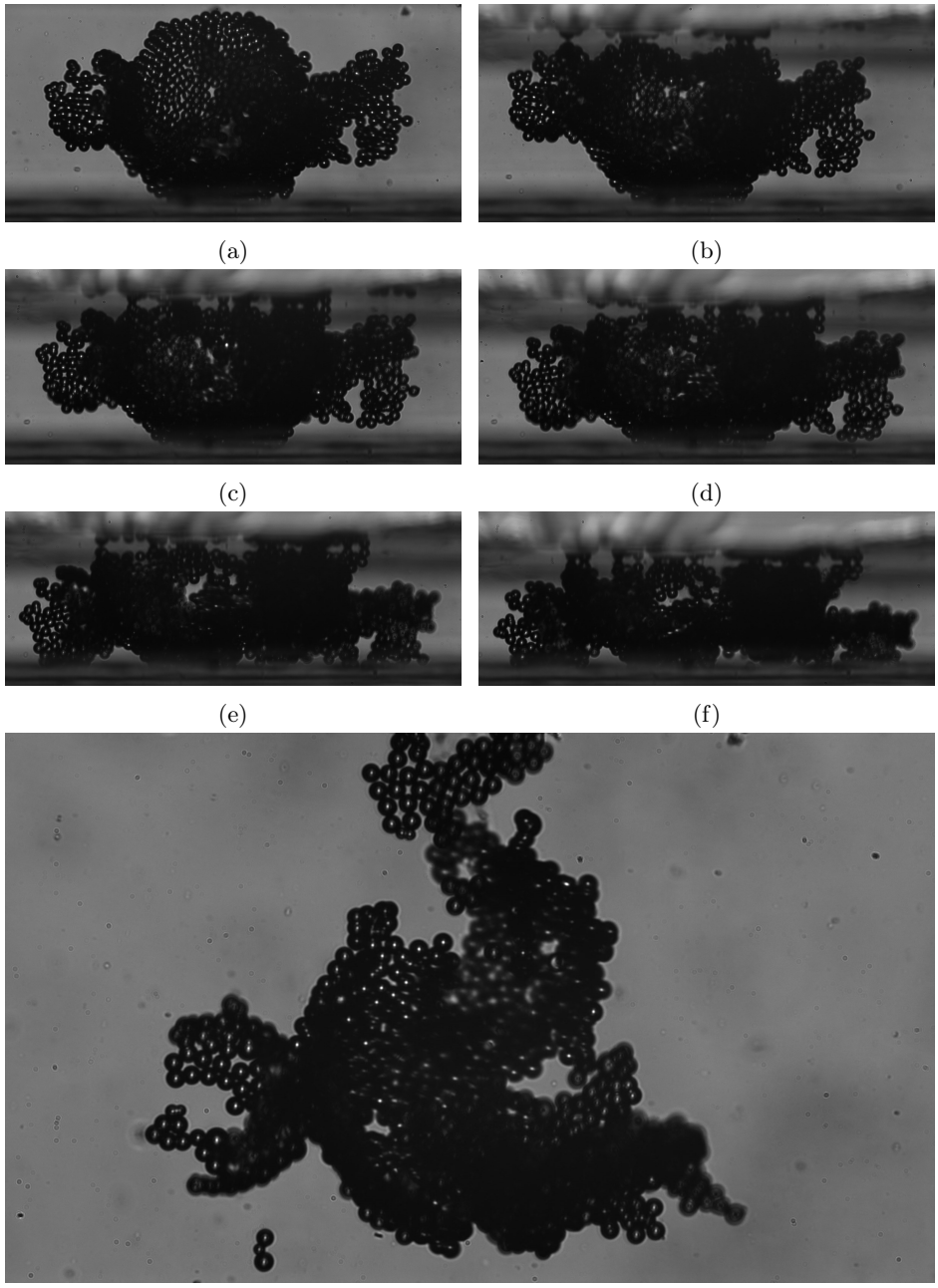

(a) (b) (c) (d) (e) (f) (g)

Figure 4.15: Image sequence of capsule crushing with no droplet inside. Original capsule diameter was 800 µm. Polystyrene bead size was 40 µm.

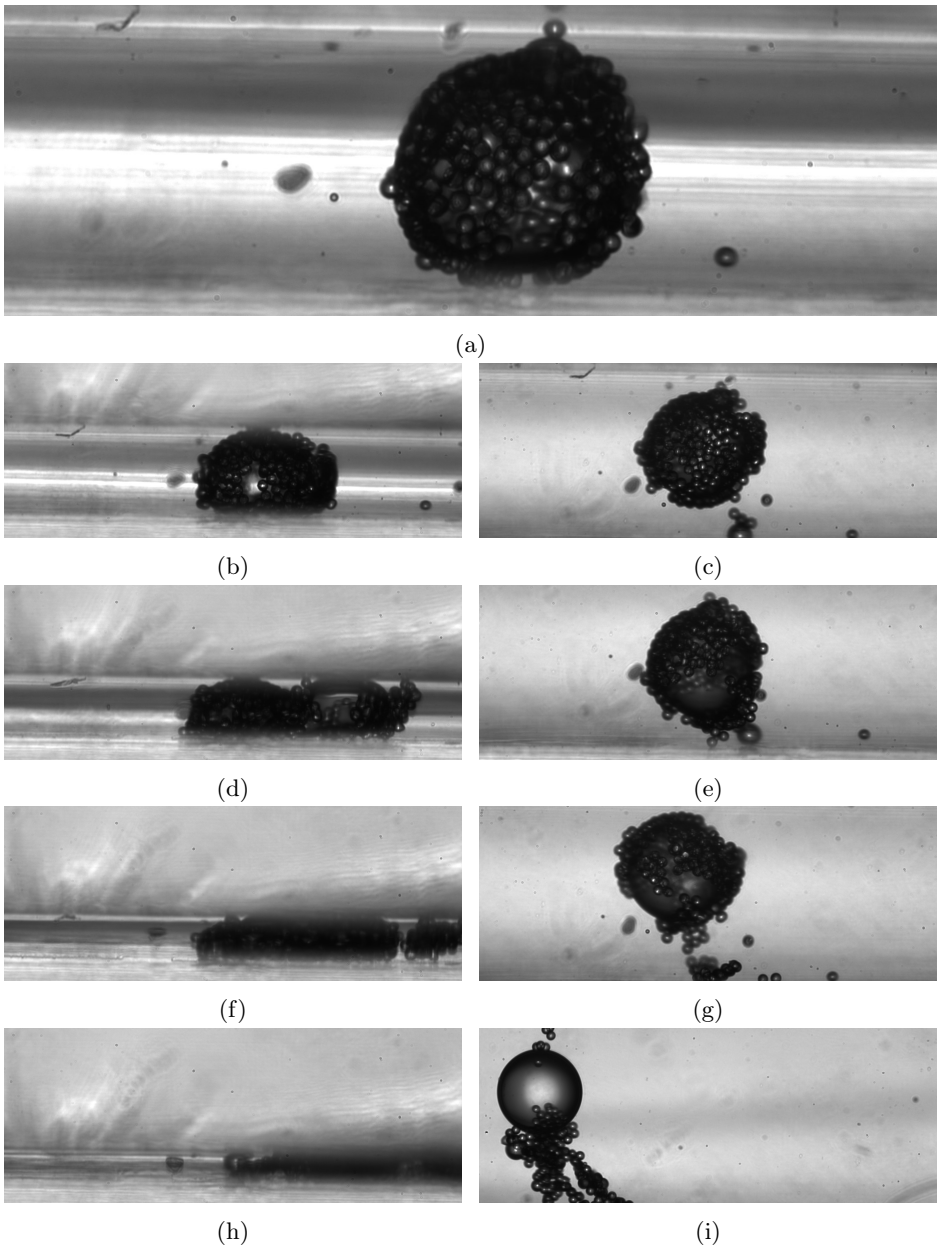

Figure 4.16: Image sequence of capsule crushing with a droplet inside. Original capsule diameter was 500 µm. Polystyrene bead size was 40 µm.

was typically kept for 15–20 minutes, ensuring a proper sintering of minimum 5 min at the glass transition temperature. Some sintered capsule fragments were examined with a scanning electron microscope (SEM), allowing much higher resolution than the previous optical examinations. The capsule fragments were sputter coated with an approximate 20 nm gold layer.

The SEM showed a wide range of different melts in the joints between the individual microspheres, even though the fragments were from the same production process, in other words produced in the same sample cell simultaneously, thus experiencing the same conditions, assuming no significant local variations in the sample cell. From the same production process, there were some fragments with thick melt around the joints, and some fragments with only small areas of contact, with several holes in the joints. The angular portion of the melt was observed to be distributed in the range of 20° to 50°, resulting in neck cross-sections in the range from 7 µm to 19 µm. For sintered microspheres forming triangles, the melt was sometimes coalesced, as shown in figure 4.17. Wrinkles in the melt were also observed in some of the joints.

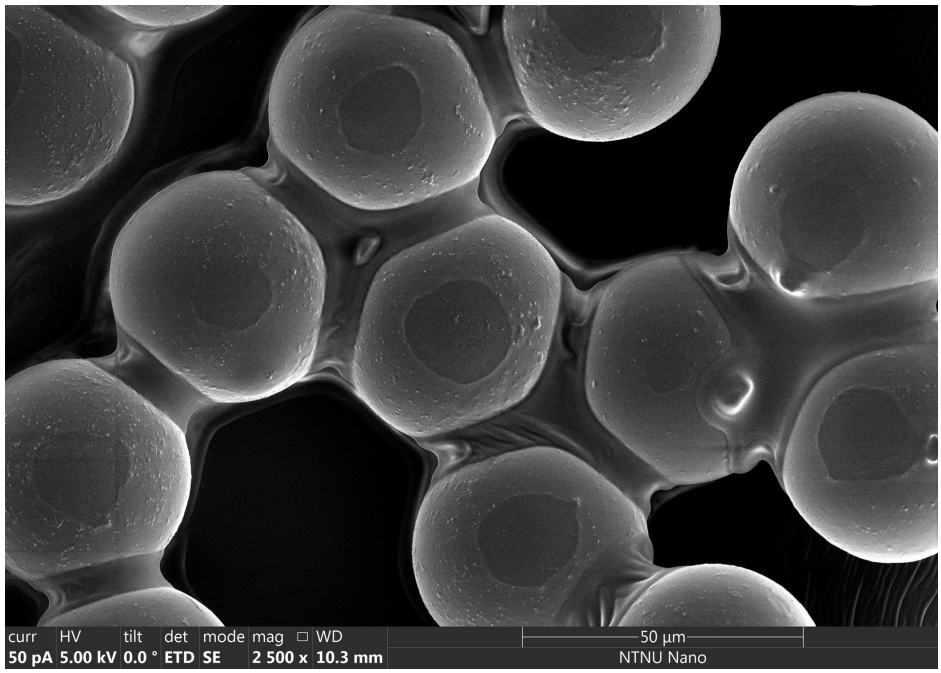

Figure 4.17: SEM image of sintered beads with excessive melt in the joints. Wrinkles in the melt can be observed in the lower right part of the image.

A comparison of different degrees of sintering are shown in figure 4.18.

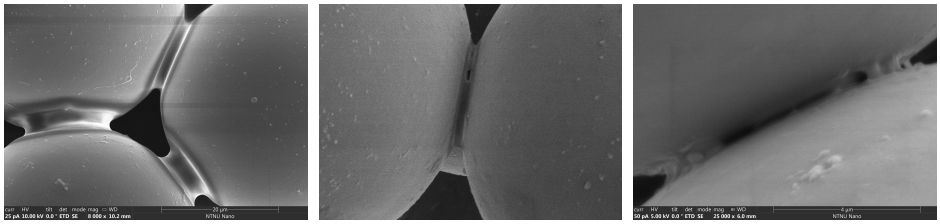

(a) (b) (c)

Figure 4.18: Comparison of degrees of sintering. All different fragments were from the same production process, extracted, emptied, cleaned with ethanol, and sputter coated with 20 nm gold.

As no different conditions were used for the different fragments in figures 4.18a, 4.18b, and 4.18c, it is difficult explain the differences observed. The fragments were rinsed in ethanol. The fragment in figure 4.17 was rinsed in ethanol for several hours, while the three fragments in figure 4.18 only were rinsed for approximately ten minutes each. No correlation between rinsing and amount of melt was observed, and polystyrene is also not soluble in ethanol [60], so it is not believed to have an impact on the amount of sintering melt.

4.3.7 Estimating the effect of electric field

There were attempts at producing capsules with no electric field during the entire creation procedure, to see whether there was any use of the Taylor-Melcher flow, or if the capsules could just as well be made without any electric field.

The electric field was originally used to propel the particles inside to the droplet interface, as described in section 2.5. With no electric field on, the particles would have to diffuse to the oil-oil interface by themselves, either by thermal diffusion, by the convection while sintering, or by sedimentation, as they had higher density than the oil ($1050\,\mathrm{kg\,m^{-3}}$ versus $970\,\mathrm{kg\,m^{-3}}$).

Experiments without any electric field showed that all particles indeed were transported to the droplet interface, but they only partly covered the droplet surface, creating thick layers, 3–5 particles in thickness, and were highly uneven.

Thus, it was concluded that the use of an electric field and the Taylor-Melcher effect was highly necessary for the results.

4.4 Sintered capsules with added metal beads

Previous experiments with soft unsintered capsules on droplets have shown that metal and plastic beads can be mixed, to produce a binary composite structure on a droplet, of a conductive armour forming longitude grid lines with poles toward the electrodes, and an insulating armour forming the equator, normal on the conductive armour [42]. The amount of particles in the droplet can be adjusted to fully cover it by a mixture of conducting and insulating particles.

This was performed with mixtures of either polyethylene or polystyrene particles, coupled with silver coated glass beads. Using Cospheric SLGMS-AG-2.55 45-53um silver-coated glass beads, mixed with one of the two polymers, droplets with both insulating polymer and conductive silver-glass beads could be produced. It was attempted to fabricate droplets with a controllable ratio of polymer beads to silver-glass beads, but it was hard to mix a homogeneous sample of oil, polymer, and silver-glass, due to the strong sedimentation of the heavier silver-glass beads (densities of $2.55\,\mathrm{g\,cm^{-3}}$ for the silver-glass beads, $1.05\,\mathrm{g\,cm^{-3}}$ for both the polyethylene and polystyrene beads, and $0.970\,\mathrm{g\,cm^{-3}}$ for the silicone oil inside the droplets).

Soft unsintered capsules fully covered by polyethylene and silver-glass beads were successfully fabricated, as can be seen in figure 4.19a. Due to the low melting point of polyethylene and lack of a significant glass transition temperature, when heated, the polyethylene melted into blobs. If the ratio of silver-glass beads was significant enough, the blobs did not coalesce, but stayed separated by the silver-glass beads, as can be seen in figure 4.19b. This droplet was then still soft, as the silver-glass beads first start to soften at temperatures above 650 °C, according to the supplier.

However, with polystyrene, the polymer beads successfully sintered at the glass transition temperature, trapping the silver-glass beads on the surface, as can be seen in figure 4.19c.

In figure 4.19c, the metal beads do not follow the same nice grid line pattern as on the droplet in figure 4.19a. Some reasons for this are the heat convection, tumbling the droplet over its own axis, not allowing the conductive beads to settle in a stable electrical pole-to-pole arrangement on the drop. Another reason is the dense packing on the droplet surface, being so dense that the beads are arrested, unable to move, even under the influence of the electric field.

Due to these reasons, together with a desire to focus on the main task of pure polystyrene covered droplets, no further experiments were done with the conductive silver coated glass beads.

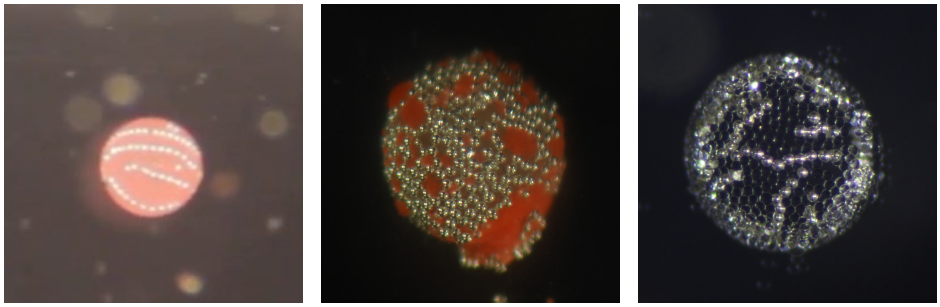

(a) (b) (c)

Figure 4.19: Polymer capsules with interlaced silver-glass beads. (a) depicts a soft polyethylene capsule before being heated. (b) shows another polyethylene capsule, but after reaching the melting point of the polymer. The capsule is still soft, as the polymer melt blobs are not connected. (c) shows a sintered polystyrene capsule. The silver-glass beads are the grey particles in all three images. Capsule diameters are (a) 740 µm, (b) 810 µm, and (c) 820 µm.

Chapter 5

Discussion

In this thesis, capsules have been produced by the sintering of polymer beads. While the title of this project has no common previous sibling in literature, it certainly has ancestors, as the techniques and processes outlined in this thesis all are built up from previous scientific work. I will here discuss the results and refer to previous work that, while not being entirely similar, is at least relevant to this work.

5.1 Droplet deformations

As outlined in the theory chapter, the research of droplet deformations in electric fields stretches at least back to 1953, with O'Konski and Thacher's paper on "The distortion of aerosol droplets by an electric field" [27]. But the field did not mature until 1966, when the work of Geoffrey Taylor was published, considering the viscous forces in the droplets, giving rise to the circulating flow inside the droplets, as shown theoretically in figure 2.6 [32]. The same circulating flow has been observed experimentally, here in figure 4.3a, in Taylor's publication itself, in addition to several other publications [33, 38, 42, 65]. Furthermore, the circulating flow has recently been verified numerically [66–70]. Although the theoretical data qualitatively matches the experimental observations (such as the pattern of streamlines and predicting prolate versus oblate deformations), there is still significant mismatch on a quantitative level between the values predicted by theory and the ones measured in experiments.

In the end of section 4.1, it was mentioned that the experimentally measured droplet deformation was not in accordance with the theoretical value (measured $D \approx -0.020$, compared to calculated value of $D = -0.0088$). While this is not a

major result in this thesis, it is important to note that this discrepancy is widely acknowledged. Torza *et al.* did an extensive study on droplet deformations, both for DC and 60 Hz AC fields, and found that while the Taylor-Melcher theory did correctly predict whether the deformation was oblate or prolate, the measured deformation was always greater than the one predicted by theory, the measurement typically being more than a factor two off the theoretic value [34, 38]. This seems to support the recorded value in the measured deformation presented in the results-chapter (see section 4.1). Several attempts have been made to fix the Taylor-Melcher theory, but so far without complete success [71, 72].

In addition, the Taylor-Melcher theory is for unladen droplets (droplets without any surface coating). Adding particles to the oil will change the response to the electric field, either by adding conducting particles that effectively short-circuiting the droplet, or by adding a mechanical armour around the droplet, resisting deformations [8, 42, 57, 73].

The calculation for the deformation is found in equation 2.31. It should be noticed that in addition to the surface tension γ of the interface, also the conductivity ratio σ_r and the viscosity ratio μ_r affect the deformation of the droplet. These values can be difficult to measure precisely, especially the conductivities, as the oils are such good insulators that they almost do not conduct any electricity. The values used in the calculations, shown in table 3.1, were from previous experiments on the same oils, but these values themselves were uncertain, as the oils in some cases were past their expiration dates. But as these experiments were qualitative, the previously obtained values were considered good enough.

5.2 The glass transition of polyethylene

The glass transition temperature T_g has several definitions without a proper rigorous background, as already mentioned in the theory chapter (see section 2.6 for more detail). Some sources define the T_g as the temperature where the viscosity of the polymer crosses 10^{12} Pa s [48], while other sources define it as the temperature where a polymer melt solidifies without crystallising or changing volume, but where the specific heat is discontinuous [74].

Polyethylene beads were used in some experience, as outlined in sections 4.2.2 and 4.4. Even though T_g for PE is reported to be $-125\,^\circ$C [50], the PE beads did not show any signs of sintering until reaching their melting point at approximately 105 °C. Due to the lack of sintering, a calorimetry measurement was carried out on the PE microspheres, as show in figure 5.1. In total, the polyethylene sample was measured from $-50\,^\circ$C to 219 °C, and the data did not show any other peaks

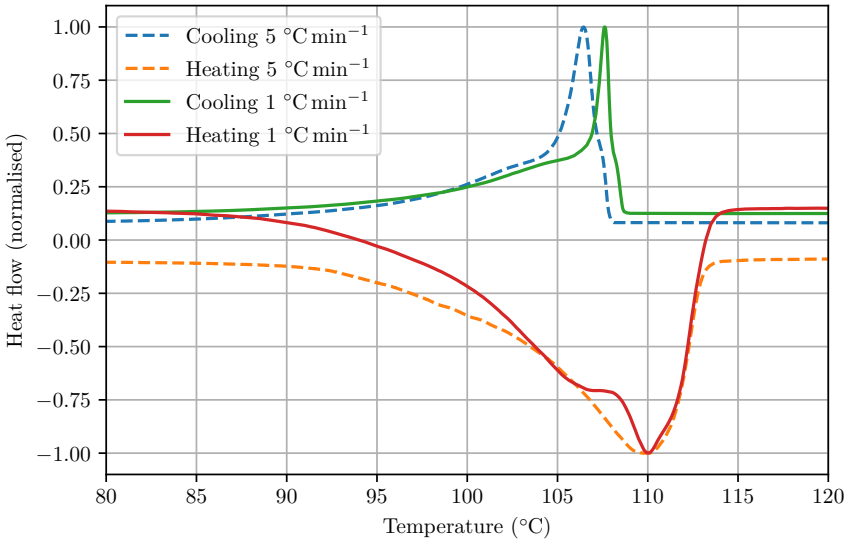

Figure 5.1: Calorimetry results, analysing Cospheric UVPMS-BR-1.050 45-53 µm beads. Both cooling and heating was performed, with a temperature gradient of both $\pm 1\,^{\circ}\mathrm{C\,min^{-1}}$ (solid lines) and $\pm 5\,^{\circ}\mathrm{C\,min^{-1}}$ (dashed lines). The melting point appears as a peak, which for the different coolings/heatings is at the temperatures from 106 °C to 110 °C. Measurements performed at Institute for Energy Technology (IFE), Kjeller by Geir Helgesen.

or transitions than those shown from the temperature range of 80 °C to 120 °C. The figure shows a big spike for the melting in the range 106 °C to 110 °C, but no glass transition, as this happens at much lower temperatures.

The melting temperature observed in figure 5.1 is quite far from the literature value of 138 °C [50]. This is likely due to the quality of the polymers themselves, as the melting point is dependent on the degree of polymerisation, which can vary for different polyethylene products [49, 75]. This is especially true for the glass transition temperature, which for polyethylene has been calculated to temperatures ranging from −135 °C to −10 °C, with one publication even stating that their "method of detecting a glass transition ... is relatively freer of subjective judgement than most" [76–78].

The reason for the wide span in the measured glass transition temperature of polyethylene, can be found in how polyethylene crystallises. It crystallises very

easily, making it unable to form a glass transition, as it requires an amorphous state below the melting temperature [77].

While polyethylene is highly crystalline, polystyrene is completely amorphous, allowing a properly defined glass transition, reported in the range of 100 °C to 105 °C [50, 51, 74, 78]. Therefore, polystyrene is in a rigid glassy state at temperatures well below the glass transition temperature T_g. When polystyrene is heated up to its glass transition temperature, it behaves like a rubber with high internal friction. Polystyrene at its T_g, unlike rubber, has no chemical cross-links, but rather molecular entanglements, giving rise to a quasi-rubber-elastic behaviour [79]. Reaching the melting point at approximately 240 °C, it melts to form a Newtonian liquid. For the experiments in this thesis, the polystyrene beads were heated to the glass transition temperature, and successful sintering was observed.

5.3 The strength of the capsules

The strength of the capsule is hypothesised to be partly dependent on the degree of sintering, i.e. the amount on melt combining the polymer beads. In figures 4.18 and 4.17, several capsule fragments are shown, all from the same fabrication process, from the same sample cell, at the same time, thus experiencing equal temperatures. Nevertheless, the amount of melt in the figures is widely varying, from an angle of 20° for the fragment depicted in 4.18c, to connected melt between the different particles in 4.17.

This large difference in melt for fragments that should have experienced the same conditions was perplexing. This could be explained by a net electrostatic charge on the beads, indicated by the wrinkles in figure 4.17 (excluding oil remains), and the consistent amount of melt on all beads in the fragment (excluding polymer anisotropy). The electrostatic charge can force the beads tighter together for some fragments more than other, and thus increase the ability for sintering of the viscoelastic polystyrene at the glass transition temperature.

It is further shown in section 4.3.5 that the enclosed droplet has a great impact on the overall rigidity and strength of the capsule. It is noted that the capsule with a droplet enclosed could resist compression down to 1/3 of its original size without being fatally destroyed. This is consistent with previous results with liquid marbles (aqueous liquid droplets coated with a hydrophobic powder), which have been shown to be able to sustain reversible deformations of 30 % of their original size [80]. Although the measurements for the liquid marbles are conducted for water droplets in air, with much higher surface tension than for the oil emulsions presented in this thesis; the similar result give support to the hypoth-

esis that the enclosed droplet has a great influence on the strength of the capsules.

Further, the packing density and size of the capsules are thought to influence the strength of the capsule. Higher packing density increases the bead count on the capsule, increasing the number of melted joints between the beads. A smaller capsule will have higher Laplace pressure, given by

$$\Delta p = \frac{2\gamma_{\mathrm{Si-Castor}}}{R} \tag{5.1}$$

for spherical droplets. Thus, the rigidity of the droplet will increase for higher curvatures $H = 1/R$, as the internal pressure rises. As smaller droplets have smaller surface area, with less space for beads, it's difficult to assess whether a capsule would fare better for smaller capsule diameters. It was attempted to reduce the size of the capsules during fabrication, but it was not feasible by producing the droplets manually using a 2 µL micropipette. A finer micropipette, or an alternative method for droplet production, such as a microfluidic chip is required for further reduction in droplet size.

5.4 The fabrication, and further possibilities

The methods for fabricating the capsules is described in chapter 3. However, this is not the only way of fabricating sintered capsules. Experimental research on micro- and nanocapsules is a field of particular interest at the current time, with much work being done on soft matter since the turn of the current millennium. Much work is especially being done on colloid-based capsules of sizes 100 µm and down to 100 nm, using techniques including UV-curing [9, 81], van der Waals forces [11], glass transition [16, 51], gels [82], or polymerisation with [83, 84] and without [85–87] organic polymers.

However, most of the experiments mentioned result in completely covered capsules, which in some cases can lead to bursting of the capsules [16]. Using the method presented in this thesis, i.e. sintering by utilising the glass transition of polystyrene, the coating is made porous, allowing mass transfer and emptying through the walls, although the pores can optionally be removed by sintering over a longer time [64].

The diameters of the capsules fabricated in this master project ranged from 0.4 mm to 1.2 mm. This is a territory mostly unexplored by other experiments. A reason is possibly the method of assembling the particle layer on the interface, which for many experiments involve spontaneous particle adsorption from the outer fluid by Brownian motion. This leads to the particles being trapped by

the difference in surface energies, which favours adsorption if the surface tension between the inner and outer fluids is greater than the difference between the surface tensions for the particle and each of the fluids [5, 51, 53]. While the diffusion rate for sub-micrometre particles is relatively fast, mere minutes for diffusing a couple of micrometres in low viscosity oils ($\sim 10^{-2}\,\mathrm{Pa\,s}$), the diffusion rate for a 40 µm particle in a 1 mm silicon oil droplet can be many years [42]. Therefore, for this experiment to work, external guiding was needed, in the form of the electrohydrodynamic flow from the external electric field.

Especially for the small particle sizes (10 µm and 20 µm), particles were ejected from the interface when heated. The interfacial surface energy binding the 40 µm particles to the oil-oil interface is characterised by [53]

$$\Delta E \approx \pi r^2 \gamma_{\mathrm{Si-Castor}} \approx 6 \times 10^{-12}\,\mathrm{J}. \tag{5.2}$$

This binding energy even for the smallest particle size is more than 10^7 times greater than the thermal energy, so it should be a stable system even at high temperatures. But due to the thermal convection in the host fluid, the particles experience a Stokes drag doing a work on the same scale as the binding energy, giving the thermal convection the ability to carry the particles away from the oil-oil interface.

This can thus be counteracted by increasing the binding energy or reducing the drag on the particles. While it is not trivial to change the particle sizes or fluids entirely to maximise the binding energy, an easier solution could simply have been to swap the inner and outer fluids, while still having the particles inside the droplet, which would in this case be castor oil. This way, while insufficient particle numbers now form pole patches instead of a equatorial ribbon [88], the outer fluid would have a greatly reduced viscosity, compared to the droplet, reducing the Stokes drag. Furthermore, particles had an affinity to the castor oil, as shown in figure 5.2. By swapping the oils, the particles would be mostly inside the droplet, shielded from much of the convective flow. The oils were never swapped in these experiments.

Further improvement for smaller particle sizes could possibly have been achieved by reducing the thermal convection. Especially promising is the possibility of creating a microfluidic chip for the fabrication of the capsules. It has already been shown that it is possible to fabricate monodisperse droplets with a controllable amount of particles using a microfluidic chip [17]. Although this entirely new setup most certainly introduced new challenges, the possibility of precisely controlling the capsule production is for sure intriguing. Using a microfluidic chip, the thermal convection could be greatly reduced, as the droplets are more tightly confined, and the heating could be more directly applied on the soft capsules, also reducing the time from heating up the entire sample cell. For further work with Janus capsules, a microfluidic chip also seems like a better

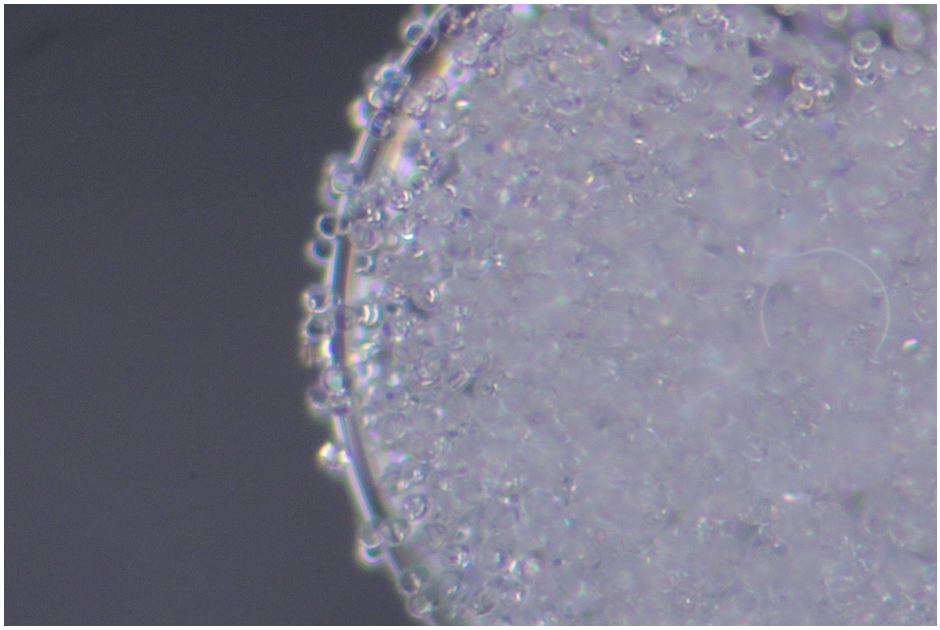

Figure 5.2: Polystyrene particles showing affinity to the outer fluid, with the outer fluid being castor oil, and the inner fluid being silicone oil. This is a cut-out of the photo in figure 4.1b.

setup than the one used in the experiments for this thesis, as the positions of the droplets can be more precisely controlled upon coalescence.

As for other future work, several possible improvements can be proposed. These experiments were mostly qualitative, and the results are based on visual observations and photos through optical microscopy, in addition to a SEM. The physics behind the fabrication of the capsules is diverse and interesting. Here follows some possible improvements and more exact studies on different aspects encountered during the year these experiments were conducted.

The crushing of the capsules, as presented in figures 4.15 and 4.16, could have been quantitatively recorded by using a mass weight under the cell containing the capsule [80]. This way, the rigidity of the capsules could have been measured, giving more rigorous data on the differences by having an enclosed droplet or not.

The images from the SEM are interesting, especially considering the various degrees of melt on fragments of capsules from the same sintering process, as shown in figure 4.18. An entire project could have been done on this alone, analysing the differences in amount of melt, possibly finding correlations with the sintering

time and temperature, and capsule size. Also finding the correlation on amount of melt and capsule strength would be interesting to have. While no complete capsule could be analysed in a SEM for this thesis, more work on the process of removing oil could possibly allow complete capsules to survive until a SEM analysis.

An important part of utilising these capsules involves the removal of the enclosed droplet. Due to the high viscosity of the outer fluid, the fluid resistance was very high, making it difficult to precisely control the fluid flow in the micropipette aspiration experiments. With more capsules, lower fluid viscosity, more controlled fluid flow, and more consistent capsules, a more rigorous statement could have been drawn from the results than was possible with the six capsules analysed here.

In general, with more data comes better results, so for further work, more capsules, and more consistent capsules, the physics of these capsules could be better understood.

5.5 The use of microspheres

The experiments in this thesis show a wide use of microbeads of either polyethylene or polystyrene, ranging in diameters from 10 µm to 50 µm. The microbeads were used as the capsule materials for the capsules presented throughout the thesis, and as tracer particles in figure 4.8. Although only a few grams of microbeads were used in total during the year of this master project, the use is contributing to the increasing problem of microplastics. The term *microplastic* is usually defined as the plastic debris smaller than 5 mm, with no lower bound of size [89]. The lack of a lower bound is due to the inability to capture and detect particle sizes smaller than 20 µm, although it is likely that even smaller particles of plastic debris exists in the environment.

The field of microplastics has seen a large rise in publications in recent years [89], and is a global problem, with plastic pollution being found in nature, especially marine environments [90, 91]. Microplastic has been found to affect the marine life, as animals digests the micrometre sized particles [90, 92–96]. These microparticles have been shown to have negative consequences [97, 98]. Although some species can survive high concentrations of polystyrene microspheres, the chronic and long-term effects for the ecosystem are still not known [96, 97].

Due to the rise of microplastic levels in the ocean, much focus has been put on how to reduce the pollution, in addition to bans on some products containing microbeads in several countries recently [99]. Although the use of plastics in

society has brought many benefits, the problem seems to be the large number of emissions of plastics into the ocean [89, 100].

The emission of microparticles can be counteracted with waste reduction and better recycling routines. As a possible use for capsules in the micrometre to millimetre range could be in medicine, stable insoluble polystyrene capsules are not a good fit for the task. For further research, a more biodegradable material would be preferable if the capsules were to be used outside of a lab. Polystyrene capsules can have their relevant fields of use, and the results from the experiments performed in this thesis are indeed promising.

Chapter 6

Conclusion

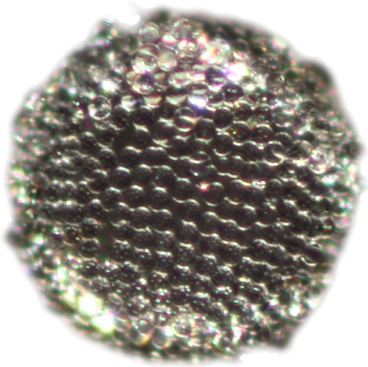

Figure 6.1: An example of a highly spherical capsule fabricated from sintering 40 µm polystyrene beads on a silicone oil droplet, after assembling the particle layer on the oil-oil interface by utilising electrohydrodynamics. The capsule has an approximate diameter of 600 µm.

Summarising. in this thesis we have examined the fabrication of capsules from the sintering of polymer beads. Such a capsule is shown in figure 6.1.

Silicone oil droplets with particles inside were made with a micropipette in a rectangular sample cell containing castor oil, making droplets ranging from 100 µm to 2000 µm. The particles, which in this thesis consisted of either wax, polyethylene, or polystyrene, were propelled to the surface of the droplets by fluid flow induced by applying an electric field of $200\,\mathrm{V\,mm^{-1}}$, as described by the Taylor-Melcher leaky dielectric model. By covering the entire droplet in particles, a soft arrested droplet was produced.

It was attempted to fabricate capsules of droplets covered in melted wax, but due to the melted layer of wax being too weak and brittle, no structural support was gained by the droplet.

Attempts to fabricate capsules of polyethylene were also unsuccessful, as polyethylene does not experience a glass transition, as it is highly crystalline. Also, the interfacial tensions for melted polyethylene in silicone oil and castor oil favours partly engulfed drop pairs, as opposed to double emulsions.

Using beads of polystyrene, which is amorphous, spherical capsules were fabricated by sintering the beads at the glass transition temperature, which is at approximately 100 °C. Capsules were fabricated for bead diameters of 20 µm and 40 µm, but the smaller sizes of beads were weaker attached to the oil-oil interface due to the reduced surface energy. This reduced surface energy resulted in beads being ejected from the drop surface, inhibiting the production of well-covered capsules. Thus, only the 40 µm capsules were further analysed.

The capsules were analysed using optical microscopy and scanning electron microscopy, in addition to probing using an experimental setup for micropipette aspiration. The capsules showed packing densities ranging from 0.78 to 0.88, although some capsules had larger patches without particles, while other parts were close to the theoretical maximum of hexagonal packing. Different portions of melt were observed between the sintered polystyrene particles, ranging from 20° to 50°, to melt from different joints coalescing. The variation in melt is attributed to variations in net electrostatic charge for different capsule fragments.

The capsules could be emptied of the encapsulated oil by attaching the capsules to a syringe tip with a smaller tip diameter than the capsule itself and sucking the inside oil out. These emptied capsules could then further be transferred to other media, such as water or ethanol, and could also be dried. Dried capsules mostly collapsed, and it was found that the encapsulated droplet had great influence on the strength of the capsule. The encapsulated droplet also allowed more mechanical deformation, as the surface energy of the inner oil droplet allowed the layer of beads to recover to a spherical shape, even though the effect of sintering itself was cancelled.

Finally, capsules with added metal-coated glass beads were briefly examined. Capsules with binary composite structure were successfully fabricated, where the insulating polystyrene beads trapped the conductive beads by sintering at the glass transition temperature.

For future work, more quantitative analysis is recommended, and with more

capsules, as the limited scope of this project did not allow analysis of a large data set. While this thesis shows much of the possibilities for the capsules, it also shows many directions further studies could go. Some of the aspects of this thesis that could be further investigated include the variations in melt from sintering, measures of the mechanical strength of the capsules, varying sizes of beads, varying sizes of droplets, and other capsule materials. Especially biodegradable materials would be interesting to use, as the current polystyrene capsules are not degradable in nature.

As a conclusion, these experiments show just some of the great versatility of sintered capsules, indicating great promise for future studies on the subject.

Appendix A

Source code

Some computer code was written during the work on this masters project to reduce the workload while in the lab (in the case of the two first scripts), and to make nice figures (the last two scripts). That code is shared here, so that anyone who does something similar in the future will not have to spend as much time as I have in the effort of creating nice looking figures.

A.1 Arduino UNO code

A.1.1 Voltage monitoring

Here follows code in C used to get an Arduino UNO to record the current applied voltage. To save the voltages to a text file on the computer, the GoBetweino[1] software was used.

```
1  void setup() {
2    // Set up data rate of 9600 bps
3    Serial.begin(9600);
4  }
5
6  int sensorValue = 0;
7  int count = 0;
8  int clickSpeed = 10;
9  int clicks = 5;
10 int refreshSpeed = 1000; // 500 is too small, as GoBetwino gets too much
       information
11
12 void loop() {
13   while (count < clicks)
14   {
15     sensorValue += analogRead(A0);
16     count++;
17     delay(clickSpeed);
```

[1] https://web.archive.org/web/20171113125718/http://www.mikmo.dk:80/gobetwinodownload.html

```
18    }
19    // Get the voltage at analog input 0
20    float voltage = (float)sensorValue / (float)clicks * 5.0 / 1023.0;
21    //                                 / count*maxV/ resolution
22    sensorValue = 0;
23    count = 0;
24
25    char buffer[50];
26    Serial.print("#S|VOLTREAD|[");
27    Serial.print(itoa((voltage*1000), buffer, 10));
28    Serial.println("]#");
29
30    delay(refreshSpeed - clicks*clickSpeed);
31  }
```

A.2 Python code

A.2.1 Electric field subtitle on recorded videos

The following Python code was used to save the voltages recorded from the Arduino code in section A.1 to a video `.srt` subtitle file.

```
# -*- coding: utf-8 -*-
"""
Created on Mon Jun 18 09:49:16 2018

@author: asbjortk

Create subtitle in .srt format from voltage readout from GoBetwino (Arudino
data extractor).
Takes in video length and start time, and then for each voltage line finds
video play time, and extracts voltage.

.srt format information from https://en.wikipedia.org/wiki/SubRip

VoltageReading.txt output format: "18.06.2018 09:34:44;663", for 663 mV

IMPORTANT: This script won't work if the film is over one hour in duration!

This is an edited script, where we create .srt's for all videos in the folder
of the current day
"""

from datetime import datetime, timedelta # read time from string
import numpy as np
import os

def timeStr (now):
    string = str(now)
    if len(string) == 1:
        string = '0' + string
        return string
    else:
        return string

today = datetime.now()
parentDir = ('C:\\Users\\asbjortk\\Pictures\\' + timeStr(today.year) +
             '_' + timeStr(today.month) + '_' + timeStr(today.day) + '\\')

videoLength = 12 * 60 # Max videolength tends to be 12 min, as MOV's exceed 4
    GB
cellWidth = 15.0 # millimeter
logInterval = 1.0 # writes every x seconds

for file in os.listdir(parentDir):
    if file.lower().endswith(".mov") or file.lower().endswith(".mp4") or file.
    lower().endswith(".m4v"):
        srtName = parentDir + file[0 : len(file) - 4] + '.srt'
        srtID = open(srtName, 'w')

        videoStartStamp = srtName[38 : srtName.find('-No')]
        videoStartTime = datetime.strptime(videoStartStamp, '%Y_%m_%d-%H_%M_%S
    ')

        with open('Z:\Arduino Sketches\Voltage_measurement\VoltageReading.txt'
    ) as f:
            lines = f.readlines()

        prevTime = datetime(1,1,1,1,1,1) # beginning of time
        line = 0
```

```
55
56          for i in range(len(lines)):
57              semicolon = lines[i].find(';')
58              timestring = lines[i][0 : semicolon]
59              linebreak = lines[i].find('\n')
60              voltageString = float(lines[i][semicolon + 1 : linebreak])
61
62              timestamp = datetime.strptime(timestring, '%d.%m.%Y %H:%M:%S')
63
64              frameStart = timestamp - videoStartTime
65              frameEnd = timestamp - videoStartTime + timedelta(seconds =
    logInterval - 1)
66              if frameStart.days >= 0 and frameStart.seconds < videoLength: # -1
     if in the past
67                  line += 1
68                  srtID.write('%i\n' % line)
69                  srtID.write('00:%i:%i,000 --> 00:%i:%i,999\n' % (
70                      np.floor(frameStart.seconds / 60),
71                      frameStart.seconds - np.floor(frameStart.seconds / 60) *
    60,
72                      np.floor(frameEnd.seconds / 60),
73                      frameEnd.seconds - np.floor(frameEnd.seconds / 60) * 60))
74                  srtID.write('%.0f V/mm\n' % (float(voltageString) / cellWidth)
    )
75                  srtID.write('\n') # end of subtitle
76
77              prevTime = timestamp
78
79          srtID.close()
```

A.2.2 Plot of dielectric sphere field lines

To plot the figures 2.4 and 2.6, Python and the matplotlib package was used. To recreate the figures, simply run the two scripts.

```
# -*- coding: utf-8 -*-
"""
Created on Mon Mar  4 10:13:25 2019

Plot dielectric sphere

@author: Asbjørn Torsvik Krüger
"""

import numpy as np
import matplotlib.pyplot as plt
import copy

res = 1001
R = 1
border = 2
ein = 3
eout = 1
er = ein / eout

def Exy(x, y, E0x, E0y):
    E0 = np.sqrt(E0x**2 + E0y**2)
    r = np.sqrt(x**2 + y**2)

    Ex = np.zeros((res, res))
    Ey = np.zeros((res, res))
    Er = np.zeros((res, res))
    Etheta = np.zeros((res, res))
    theta = np.zeros((res, res))

    for i in range(len(Ex)):
        for j in range(len(Ey)):
            theta[i,j] = np.arctan2(y[i,j], x[i,j])
            if r[i,j] < R:
                Ex[i,j] = 3 * E0x / (er + 2)
                Ey[i,j] = 3 * E0y / (er + 2)
            else:
                Er[i,j] = E0 * np.cos(theta[i,j]) + 2 * (er - 1)/(er + 2) * R**3 * E0 * np.cos(theta[i,j]) / r[i,j]**3
                Etheta[i,j] = -E0 * np.sin(theta[i,j]) + (er - 1)/(er + 2) * R**3 * E0 * np.sin(theta[i,j]) / r[i,j]**3

                Ex[i,j] = Er[i,j] * np.cos(theta[i,j]) - Etheta[i,j] * np.sin(theta[i,j])
                Ey[i,j] = Er[i,j] * np.sin(theta[i,j]) + Etheta[i,j] * np.cos(theta[i,j])
    return Ex, Ey, r

plt.close("all") # close current open figures

fig = plt.figure()
ax = fig.gca()
xField, yField = np.meshgrid(np.linspace(-border, border, res), np.linspace(-border, border, res))
E0x = 1
E0y = 0

Ex, Ey,r = Exy(xField, yField, E0x, E0y)
Ex2 = copy.deepcopy(Ex)
Ey2 = copy.deepcopy(Ey)
Ex2[r > R] = np.nan
Ey2[r > R] = np.nan
```

```
58
59 stream_points = np.zeros((15,2))
60 stream_points2 = np.zeros((int(np.round(len(stream_points)/(border * 2) * (R *
       2) * 3/(er + 2))),2))
61 for i in range(len(stream_points)):
62     stream_points[i, 1] = i * (border * 2) / (len(stream_points) - 1) - border
63     stream_points[i, 0] = -border
64 if len(stream_points2) % 2: # odd
65     for j in range(int(len(stream_points2) / 2)):
66         stream_points2[j, 1] = (-j - 1) * (2 + er) / 3 * (border * 2) / (len(
       stream_points) - 1)
67         stream_points2[j + int(len(stream_points2) / 2), 1] = (j + 1) * (2 +
       er) / 3 * (border * 2) / (len(stream_points) - 1)
68 else: # even
69     for j in range(int(len(stream_points2) / 2)):
70         stream_points2[j, 1] = (-j - 1/2) * (2 + er) / 3 * (border * 2) / (len
       (stream_points) - 1)
71         stream_points2[j + int(len(stream_points2) / 2), 1] = (j + 1/2) * (2 +
        er) / 3 * (border * 2) / (len(stream_points) - 1)
72
73 plt.streamplot(xField, yField, Ex, Ey, color='k', start_points=stream_points,
       zorder=1)
74 ax.add_patch(plt.Circle((0,0), radius=R, color='w', zorder=2))
75 plt.streamplot(xField, yField, Ex2, Ey2, color='k', start_points=
       stream_points2, zorder=3)
76 circ = plt.Circle((0, 0), R, color='k', fill=False, zorder=4)
77 ax.add_artist(circ)
78 plt.axis('off')
79 ax.set_aspect('equal')
80
81 fig.savefig("Res%iR%iB%iEr%i.pdf" % (res, R, border, er), dpi = 300)
82 fig.savefig("Res%iR%iB%iEr%i.png" % (res, R, border, er), dpi = 300)
83
84 plt.show()
```

A.2.3 Plot of Taylor-Melcher flow

Note that the `rasterize_and_save` file linked to in the preamble must be run before this script for Python to recognise the function. Also, a working LaTeX environment must be installed.

```
# -*- coding: utf-8 -*-
"""
Created on Sun Mar 17 18:10:05 2019

Plot droplet Taylor streamlines
The rasterize_and_save function requires this file: https://gist.github.com/hugke729/78655b82b885cde79e270f1c30da0b5f
It rasterizes the contour plot, so that the plot can be saved in a small PDF, while having vector text

The lines 20 to 24 require a working LaTeX installation on your computer.
Optionally, the lines can be removed, and Python will use regular sans-serif font instead

@author: Asbjørn Torsvik Krüger
"""

import matplotlib as mpl
import matplotlib.pyplot as plt
import numpy as np

# Use the LaTeX font for the sweet consistency
mpl.use("pgf")
plt.rc('text', usetex=True)
plt.rc('font', family='serif')
plt.rc('pgf', texsystem='lualatex')
plt.rc('pgf', preamble=r'\usepackage{siunitx}')

plot = True

res = 500
R = 1
border = 2

E0 = 200 * 1000
ein = 2.1*8.85e-12
eout = 4.7*8.85e-12
er = ein / eout
condin = 4e-12
condout = 45e-12
condr = condin / condout
viscin = 1e-4*970
viscout = 1e-3*961

A = -9 * E0**2 * R * ein / (8 * np.pi * (2 + condr)**2) * (condr / er - 1) / (5 * (viscout + viscin))
B = -A
C = A
D = -A

plt.close("all") # close current open figures

Psi = np.zeros((res, res))
u = np.zeros((res, res))
v = np.zeros((res, res))
V = np.zeros((res, res))
x, y = np.meshgrid(np.linspace(-border, border, res), np.linspace(-border, border, res))

for i in range(res):
```

```
  for j in range(res):
    theta = np.arctan2(y[i,j], x[i,j])
    r = np.sqrt(x[i,j]**2 + y[i,j]**2)

    if r < R:
      u[i,j] = (C * r / R + D * r**3 / R**3) * (2 * np.cos(theta)**2 - np.sin(theta)**2)
      v[i,j] = (-3 * C * r / R - 5 * D * r**3 / R**3) * np.sin(theta) * np.cos(theta)
      Psi[i,j] = (C * r / R + D * r**3 / R**3) * np.sin(theta)**2 * np.cos(theta)
    else:
      u[i,j] = (A * R**4 / r**4 + B * R**2 / r**2) * (2 * np.cos(theta)**2 - np.sin(theta)**2)
      v[i,j] = (2 * A * R**4 / r**4) * np.sin(theta) * np.cos(theta)
      Psi[i,j] = (A * R**4 / r**4 + B * R**2 / r**2) * np.sin(theta)**2 * np.cos(theta)

    rr = u[i,j]
    tt = v[i,j]
    u[i,j] = rr * np.cos(theta) - tt * np.sin(theta)
    v[i,j] = rr * np.sin(theta) + tt * np.cos(theta)
    V[i,j] = np.sqrt(rr**2 + tt**2)

V = V / np.amax(V)

fig = plt.figure()
ax = fig.gca()
seed_outx = np.array([2.0, 2.0, 2.0, 2.0])
seed_outy = np.array([0.25, 0.75, 1.25, 1.75])
seed_inx = np.array([0.15, 0.3, 0.45])
seed_iny = np.array([0.15, 0.3, 0.45])
seed_pointsx = np.concatenate([seed_outx, seed_outx, -seed_outx, -seed_outx, seed_inx, seed_inx, -seed_inx, -seed_inx])
seed_pointsy = np.concatenate([seed_outy, -seed_outy, -seed_outy, seed_outy, seed_inx, -seed_inx, -seed_inx, seed_inx])
seed_points = np.array([seed_pointsx, seed_pointsy])
plt.streamplot(x, y, u, v, zorder=1, color='#000000', linewidth=1, start_points=seed_points.T, density=10)
circ = plt.Circle((0, 0), R, color='k', fill=False, zorder=2)
field = plt.contourf(x,y, V, 256, zorder=0, cmap='plasma_r')
ax.add_artist(circ)
ax.set_aspect('equal')
ax.axis('off')
plt.colorbar(ticks=(0.0, 0.2, 0.4, 0.6, 0.8, 1))
fig.savefig("BothRes%iR%iB%i.png" % (res, R, border), dpi=300, bbox_inches='tight')
rasterize_and_save("BothRes%iR%iB%i.pdf" % (res, R, border), field, dpi=300, savefig_kw=dict(bbox_inches='tight'))
```

Appendix B

Capsule depletion image sequence

The following image sequence shows a capsule being depleted. It is the same capsule as in figures 4.12 and 4.14, and the diameter is still 825 µm. There is 0.6 seconds between each picture, so the entire sequence spans over 36 seconds.

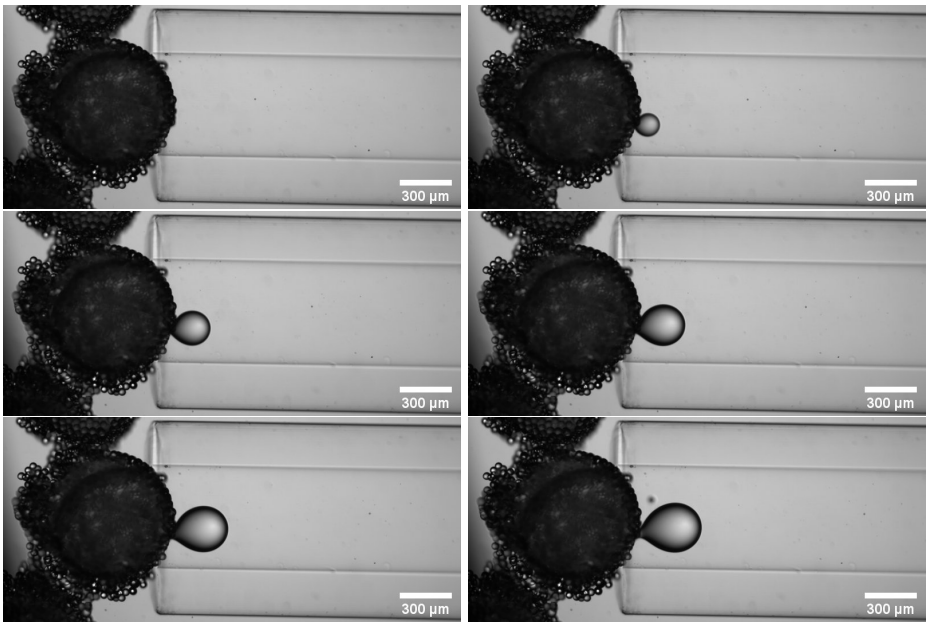

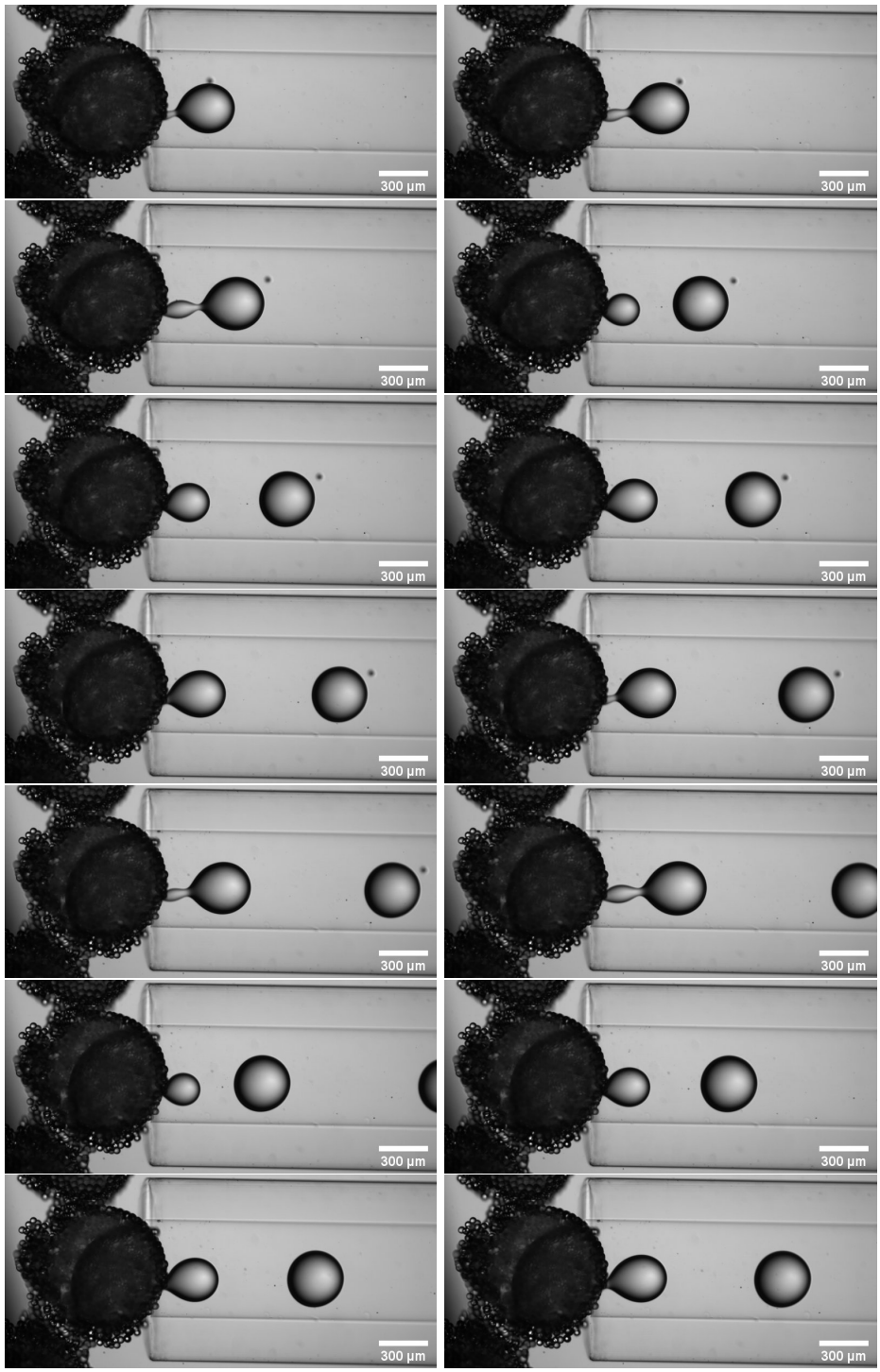
300 µm

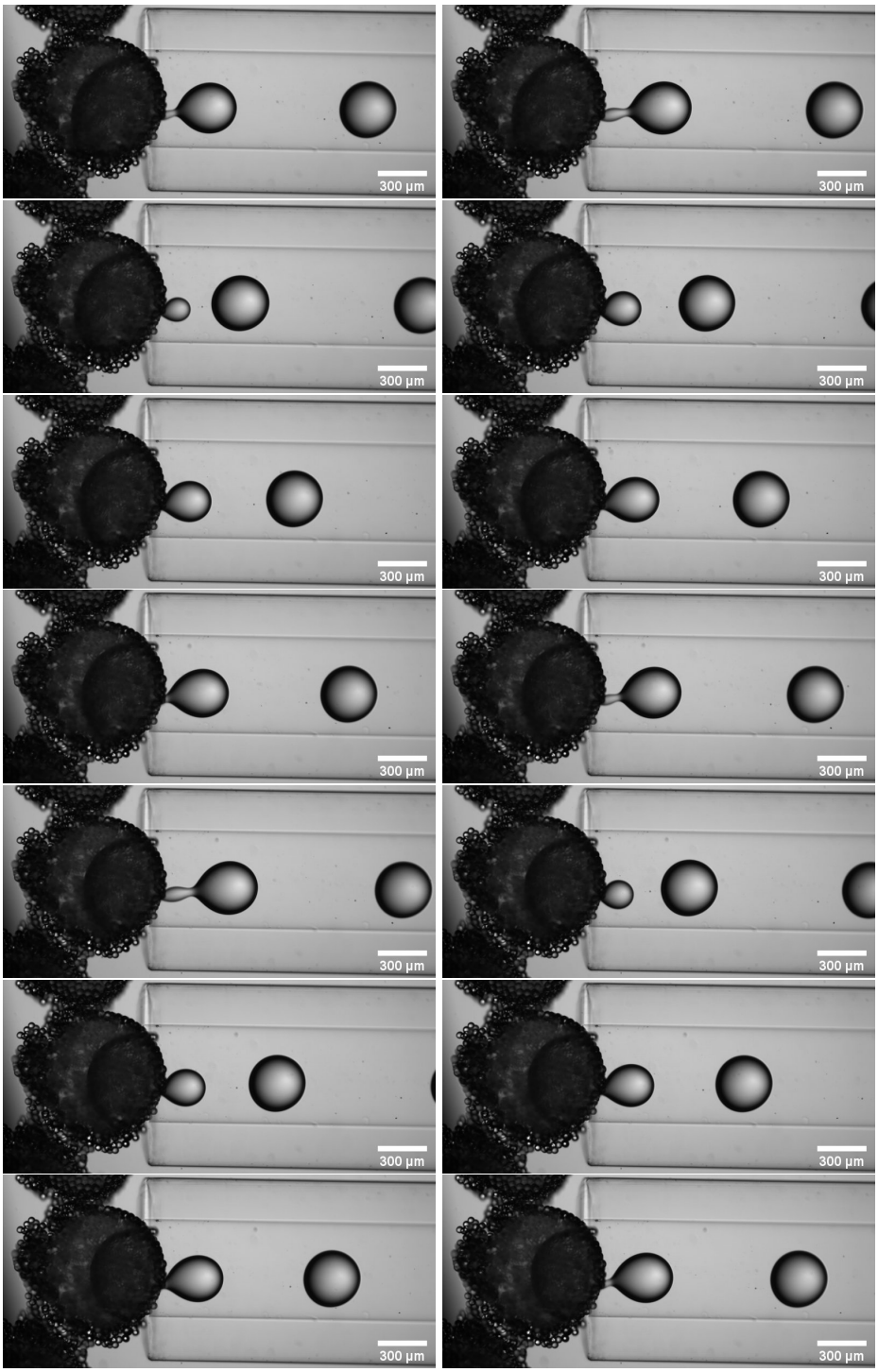
300 µm

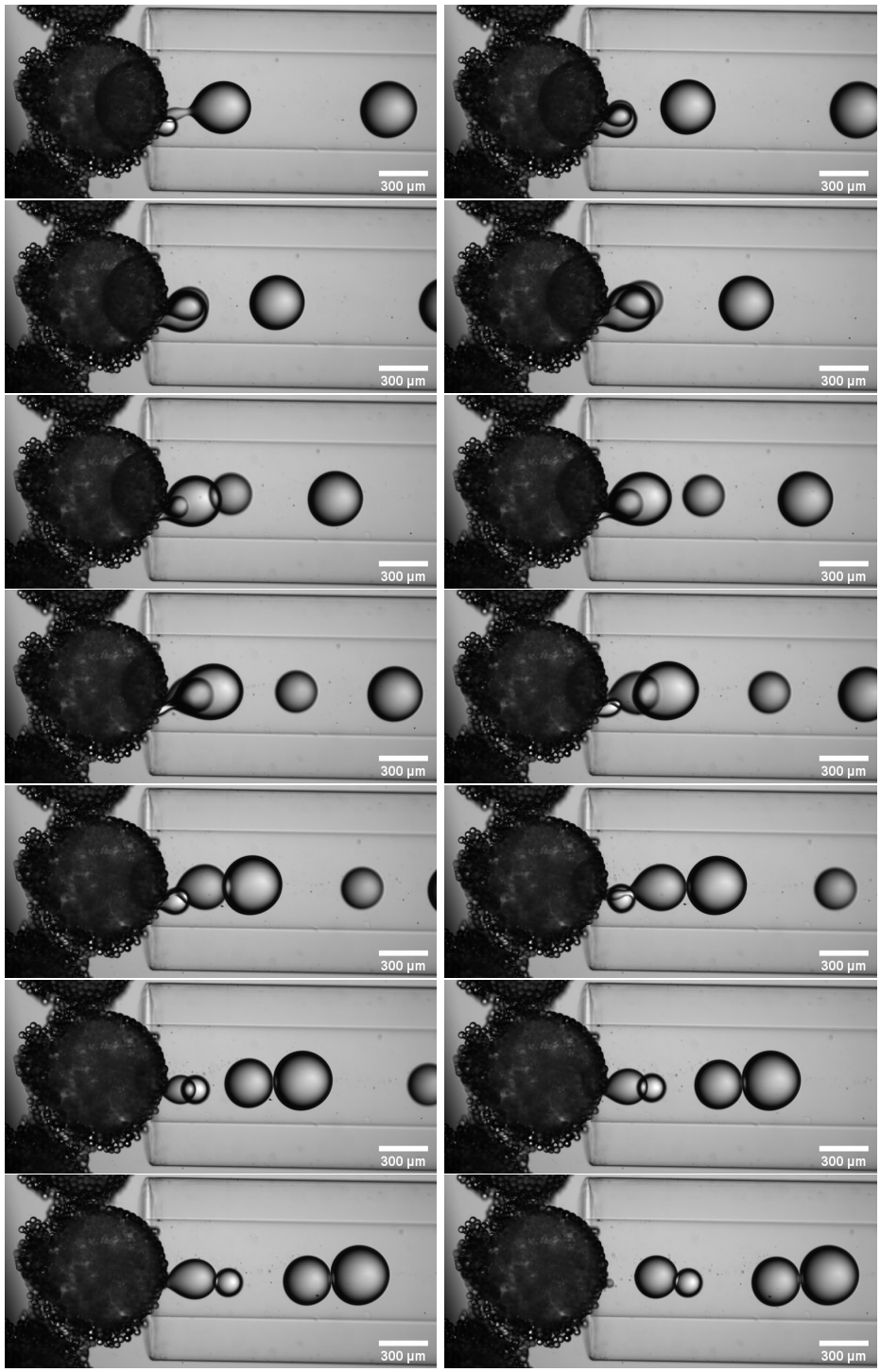
300 µm

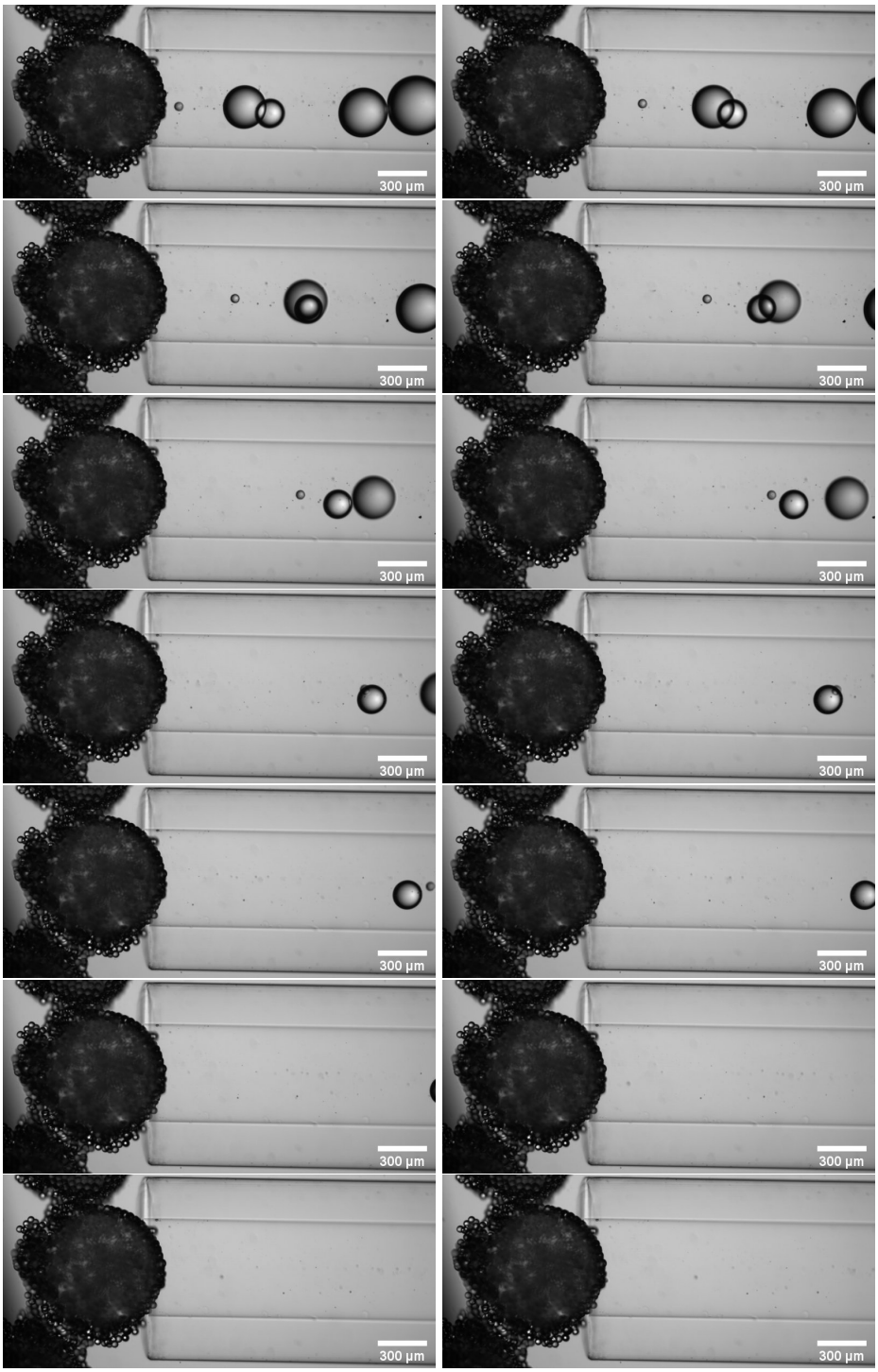
300 µm

Bibliography

[1] M. Kléman, *Soft matter physics : an introduction*, New York, 2003.

[2] A. Fernandez-Nieves and A. M. Puertas, eds., *Fluids, Colloids and Soft Materials: An Introduction to Soft Matter Physics* (John Wiley & Sons, Inc, Hoboken, NJ, USA, Apr. 2016), ISBN: 9781119220510.

[3] J. Pelesko, *Self assembly : the science of things that put themselves together* (Taylor & Francis, Boca Raton, 2007), ISBN: 1584886870.

[4] M. Doi, *Soft Matter Physics* (Oxford University Press, Oxford, June 2013), ISBN: 9780199652952.

[5] T. Bollhorst, K. Rezwan, and M. Maas, "Colloidal capsules: nano- and microcapsules with colloidal particle shells", Chem. Soc. Rev. **46**, 2091–2126 (2017).

[6] M. S. Abbasi, R. Song, H. Kim, and J. Lee, "Multimodal breakup of a double emulsion droplet under an electric field", Soft Matter **15**, 2292–2300, ISSN: 1744-683X (2019).

[7] S. Biggs and O. Cayre, "CHAPTER 9 Particle-Stabilized Emulsions as Templates for Hollow Spheres and Microcapsules", in *Particle-stabilized emulsions and colloids: formation and applications* (The Royal Society of Chemistry, 2015), pp. 228–246, ISBN: 978-1-84973-881-1.

[8] Z. Rozynek, A. Mikkelsen, P. Dommersnes, and J. O. Fossum, "Electroformation of janus and patchy capsules", Nature Communications **5**, 3945, ISSN: 20411723 (2014).

[9] P. van Rijn, N. C. Mougin, D. Franke, H. Park, and A. Böker, "Pickering emulsion templated soft capsules by self-assembling cross-linkable ferritin–polymer conjugates", Chem. Commun. **47**, 8376–8378 (2011).

[10] A. S. Utada, E. Lorenceau, D. R. Link, P. D. Kaplan, H. A. Stone, and D. A. Weitz, "Monodisperse double emulsions generated from a microcapillary device", English, Science **308**, 537–541, ISSN: 00368075 (2005).

[11] V. N. Manoharan, "Colloidal spheres confined by liquid droplets: Geometry, physics, and physical chemistry", Solid State Communications **139**, 557–561, ISSN: 00381098 (2006).

[12] S. Laïb and A. F. Routh, "Fabrication of colloidosomes at low temperature for the encapsulation of thermally sensitive compounds", Journal of Colloid and Interface Science **317**, 121–129, ISSN: 00219797 (2008).

[13] S. Seiffert, J. Thiele, A. R. Abate, and D. A. Weitz, "Smart Microgel Capsules from Macromolecular Precursors", Journal of the American Chemical Society **132**, 6606–6609, ISSN: 0002-7863 (2010).

[14] D. Lin, M. Shi, X. Wei, B. Liu, J. Cao, and C. Peng, "Development of an innovative capsule with three-dimension honeycomb architecture via one-step titration-gel method for the removal of methylene blue", International Journal of Biological Macromolecules **128**, 911–922, ISSN: 0141-8130 (2019).

[15] Q. Sun and A. F. Routh, "Aqueous core colloidosomes with a metal shell", European Polymer Journal **77**, 155–163, ISSN: 00143057 (2016).

[16] Q. Yuan, O. J. Cayre, S. Fujii, S. P. Armes, R. A. Williams, and S. Biggs, "Responsive core-shell latex particles as colloidosome microcapsule membranes", Langmuir **26**, 18408–18414, ISSN: 07437463 (2010).

[17] Z. Rozynek and A. Józefczak, "Patchy colloidosomes – an emerging class of structures", The European Physical Journal Special Topics **225**, 741–756, ISSN: 1951-6401 (2016).

[18] F. White, *Fluid mechanics* (McGraw Hill, New York, N.Y, 2011), ISBN: 9780071311212.

[19] P. Tabeling, *Introduction to Microfluidics*, English (OUP Oxford, Oxford, U.K., 2005), ISBN: 9780198568643.

[20] P. G. de Gennes, F. Brochard-Wyart, and D. Quere, *Capillarity and Wetting Phenomena: Drops, Bubbles, Pearls, Waves* (Springer New York, 2003), ISBN: 9780387005928.

[21] M. T. Sprackling, *Liquids and solids* (Routledge & K. Paul, London Boston, 1985), ISBN: 0710204841.

[22] V. I. Kalikmanov, *Statistical physics of fluids : basic concepts and applications* (Springer, Berlin New York, 2001), ISBN: 3540417478.

[23] J. Guzowski, P. M. Korczyk, S. Jakiela, and P. Garstecki, "The structure and stability of multiple micro-droplets", Soft Matter **8**, 7269–7278, ISSN: 1744-683X (2012).

[24] D. Bonn, J. Eggers, J. Indekeu, J. Meunier, and E. Rolley, "Wetting and spreading", Reviews of Modern Physics **81**, 739–805 (2009).

[25] D. J. Griffiths, *Introduction to Electrodynamics*, 4th ed., Vol. 73 (Cambridge University Press, 2017), p. 620, ISBN: 9781108420419.

[26] A. Mikkelsen, "Particle assembly guided by electrohydrodynamics and dielectrophoresis", PhD thesis (NTNU, May 2016).

[27] C. T. O'Konski and H. C. Thacher, "The Distortion of Aerosol Droplets by an Electric Field", The Journal of Physical Chemistry **57**, 955–958, ISSN: 0022-3654 (1953).

[28] C. T. O'Konski and R. L. Gunther, "Verification of the free energy equation for electrically polarized droplets", English, Journal of Colloid Science **10**, 563–570, ISSN: 00958522 (1955).

[29] E. H. Büchner and A. H. H. van Royen, "Bewegung von Flüssigkeitsstrahlen und Tropfen in einem elektrischen Felde", Kolloid-Zeitschrift **49**, 249–253, ISSN: 1435-1536 (1929).

[30] C. T. O'Konski and F. E. Harris, "Electric free energy and the deformation of droplets in electrically conducting systems", English, Journal of Physical Chemistry **61**, 1172–1174, ISSN: 00223654 (1957).

[31] R. S. Allan and S. G. Mason, "Particle behaviour in shear and electric fields I. Deformation and burst of fluid drops", Proceedings of the Royal Society of London. Series A. Mathematical and Physical Sciences **267**, 45–61, ISSN: 2053-9169 (1962).

[32] G. Taylor, "Studies in electrohydrodynamics. I. The circulation produced in a drop by an electric field", Proceedings of the Royal Society of London. Series A. Mathematical and Physical Sciences **291**, 159–166, ISSN: 2053-9169 (1966).

[33] J. R. Melcher and G. I. Taylor, "Electrohydrodynamics: A Review of the Role of Interfacial Shear Stresses", Annual Review of Fluid Mechanics **1**, 111–146, ISSN: 0066-4189 (1969).

[34] D. A. Saville, "ELECTROHYDRODYNAMICS:The Taylor-Melcher Leaky Dielectric Model", Annual Review of Fluid Mechanics **29**, 27–64 (1997).

[35] S. Goldstein and Great Britain Aeronautical Research Committee Fluid Motion Panel, *Modern Developments in fluid dynamics an account of theory and experiment relating to boundary layers, turbulent motion and wakes in two volumes*, Oxford engineering science series (The Clarendon Press, 1965), 2 vols.

[36] J. C. Baygents, N. J. Rivette, and H. A. Stone, "Electrohydrodynamic deformation and interaction of drop pairs", English, Journal of Fluid Mechanics **368**, 359–375, ISSN: 00221120 (1998).

[37] M. Ouriemi and P. M. Vlahovska, "Electrohydrodynamic Deformation and Rotation of a Particle-Coated Drop", Langmuir **31**, 6298–6305, ISSN: 0743-7463 (2015).

[38] T. S., C. R. G., M. S. G., and T. G. Ingram, "Electrohydrodynamic deformation and bursts of liquid drops", Philosophical Transactions of the Royal Society of London. Series A, Mathematical and Physical Sciences **269**, 295–319 (1971).

[39] P. M. Vlahovska, "Electrohydrodynamics of Drops and Vesicles", Annual Review of Fluid Mechanics **51**, 305–330, ISSN: 0066-4189 (2019).

[40] P. F. Salipante and P. M. Vlahovska, "Electrohydrodynamics of drops in strong uniform dc electric fields", Physics of Fluids **22**, 112110, ISSN: 1070-6631 (2010).

[41] H. He, P. F. Salipante, and P. M. Vlahovska, "Electrorotation of a viscous droplet in a uniform direct current electric field", Physics of Fluids **25**, 32106, ISSN: 1070-6631 (2013).

[42] P. Dommersnes, Z. Rozynek, A. Mikkelsen, R. Castberg, K. Kjerstad, K. Hersvik, and J. O. Fossum, "Active structuring of colloidal armour on liquid drops", Nature Communications **4**, 2066, ISSN: 2041-1723 (2013).

[43] D. Das and D. Saintillan, "Electrohydrodynamics of viscous drops in strong electric fields: numerical simulations", Journal of Fluid Mechanics **829**, 127–152, ISSN: 0022-1120 (2017).

[44] P. Dommersnes, A. Mikkelsen, and J. O. Fossum, "Electro-hydrodynamic propulsion of counter-rotating Pickering drops", The European Physical Journal Special Topics **225**, 699–706, ISSN: 1951-6401 (2016).

[45] D. Das and D. Saintillan, "Electrohydrodynamic interaction of spherical particles under Quincke rotation", Physical Review E **87**, 43014 (2013).

[46] G. R. Strobl, "The Constitution and Architecture of Chains", in *The physics of polymers* (Springer Berlin Heidelberg, Berlin, Heidelberg, 2013), pp. 1–11, ISBN: 978-3-540-68411-4.

[47] G. R. Strobl, "Mechanical and Dielectric Response", in *The physics of polymers* (Springer Berlin Heidelberg, Berlin, Heidelberg, 2013), pp. 191–256, ISBN: 978-3-540-68411-4.

[48] J. V. Selinger, "Solids: Crystals and Glasses", in *Introduction to the theory of soft matter: from ideal gases to liquid crystals* (Springer International Publishing, Cham, 2016), pp. 91–110, ISBN: 978-3-319-21054-4.

[49] J. Jackle, "Models of the glass transition", Reports on Progress in Physics **49**, 171–231 (1986).

[50] W. A. Lee and G. J. Knight, "Ratio of the glass transition temperature to the melting point in polymers", British Polymer Journal **2**, 73–80 (1970).

[51] A. D. Dinsmore, M. F. Hsu, M. G. Nikolaides, M. Marquez, A. R. Bausch, and D. A. Weitz, "Colloidosomes: Selectively permeable capsules composed of colloidal particles", English, Science **298**, 1006–1009, ISSN: 00368075 (2002).

[52] W. Wiegand, "Density fluctuations and the state of order of amorphous polymers", in Anwendungsbezogene physikalische charakterisierung von polymeren, insbesondere im festen zustand, edited by E. W. Fischer, F. H. Müller, and R. Bonart (2008), pp. 355–366, ISBN: 978-3-7985-1811-7.

[53] P. Pieranski, "Two-Dimensional Interfacial Colloidal Crystals", Phys. Rev. Lett. **45**, 569–572 (1980).

[54] T. D. Taylor and A. Acrivos, "On the deformation and drag of a falling viscous drop at low Reynolds number", Journal of Fluid Mechanics **18**, 466–476, ISSN: 14697645 (1964).

[55] J. F. Harper, "The Motion of Bubbles and Drops Through Liquids", in *Advances in applied mechanics*, Vol. 12, edited by C.-S. Yih, Advances in Applied Mechanics (Elsevier, 1972), pp. 59–129.

[56] S. Mhatre, S. Deshmukh, and R. M. Thaokar, "Electrocoalescence of a drop pair", Physics of Fluids **27**, 92106 (2015).

[57] A. Mikkelsen, K. Khobaib, F. K. Eriksen, K. J. Måløy, and Z. Rozynek, "Particle-covered drops in electric fields: drop deformation and surface particle organization", Soft Matter **14**, 5442–5451, ISSN: 1744-683X (2018).

[58] H. P. Trevithick and M. F. Lauro, "Solubility tests of castor oil", Oil and Fat Industries **6**, 27–29 (1929).

[59] C. Hansen, *Hansen solubility parameters: a user's handbook*, 2nd, Vol. 37 (CRC Press, Boca Raton, 2007), p. 544, ISBN: 9780849372483.

[60] A. F. M. Barton, "Solubility parameters", Chemical Reviews **75**, 731–753, ISSN: 0009-2665 (1975).

[61] J. Brandrup, *Polymer handbook* (Wiley, New York, 1999), p. 2317, ISBN: 978-0-471-47936-9.

[62] P. Mohammadi, G. Beaune, B. T. Stokke, J. V. I. Timonen, and M. B. Linder, "Self-Coacervation of a Silk-Like Protein and Its Use As an Adhesive for Cellulosic Materials", ACS Macro Letters **7**, 1120–1125 (2018).

[63] A. B. Pawar, M. Caggioni, R. Ergun, R. W. Hartel, and P. T. Spicer, "Arrested coalescence in Pickering emulsions", Soft Matter **7**, 7710–7716 (2011).

[64] M. F. Hsu, M. G. Nikolaides, A. D. Dinsmore, A. R. Bausch, V. D. Gordon, X. Chen, J. W. Hutchinson, D. A. Weitz, and M. Marquez, "Self-assembled Shells Composed of Colloidal Particles: Fabrication and Characterization", Langmuir **21**, 2963–2970, ISSN: 0743-7463 (2005).

[65] T. Tsukada, T. Katayama, Y. Ito, and M. Hozawa, "Theoretical and Experimental Studies of Circulations Inside and Outside a Deformed Drop under a Uniform Electric Field", JOURNAL OF CHEMICAL ENGINEERING OF JAPAN **26**, 698–703 (1993).

[66] M. A. Halim and A. Esmaeeli, "Computational studies on the transient electrohydrodynamics of a liquid drop", English, Fluid Dynamics and Materials Processing **9**, 435–460, ISSN: 1555256X (2013).

[67] Q. Dong and A. Sau, "Electrohydrodynamic interaction, deformation, and coalescence of suspended drop pairs at varied angle of incidence", Physical Review Fluids **3**, 73701 (2018).

[68] Z.-T. LI, G.-J. LI, H.-B. HUANG, and X.-Y. LU, "Lattice Boltzmann Study of Electrohydrodynamic Drop Deformation With Large Density Ratio", International Journal of Modern Physics C **22**, 729–744, ISSN: 0129-1831 (2011).

[69] R. Singh, S. S. Bahga, and A. Gupta, "Electrohydrodynamics in leaky dielectric fluids using lattice Boltzmann method", European Journal of Mechanics, B/Fluids **74**, 167–179, ISSN: 09977546 (2019).

[70] N. C. Lima and M. A. d'Ávila, "Numerical simulation of electrohydrodynamic flows of Newtonian and viscoelastic droplets", Journal of Non-Newtonian Fluid Mechanics **213**, 1–14, ISSN: 03770257 (2014).

[71] A. O. O. and C. T. George, "A note on Taylor's electrohydrodynamic theory", Proceedings of the Royal Society of London. A. Mathematical and Physical Sciences **364**, 499–507 (1978).

[72] J. C. Baygents and D. A. Saville, "The circulation produced in a drop by an electric field: A high field strength electrokinetic model", AIP Conference Proceedings **197**, 7–17, ISSN: 0094-243X (1990).

[73] A. Mikkelsen, J. Wojciechowski, M. Rajňák, J. Kurimský, K. Khobaib, A. Kertmen, and Z. Rozynek, "Electric Field-Driven Assembly of Sulfonated Polystyrene Microspheres", Materials **10**, ISSN: 1996-1944 (2017) 10.3390/ma10040329.

[74] P. C. Painter, *Fundamentals of polymer science : an introductory text*, 2nd ed. (Technomic, Lancaster, Pa, 1997), ISBN: 1566765595.

[75] G. R. Strobl, "The Semicrystalline State", in *The physics of polymers* (Springer Berlin Heidelberg, Berlin, Heidelberg, 2007), pp. 165–222, ISBN: 978-3-540-68411-4.

[76] U. Gaur and B. Wunderlich, "The Glass Transition Temperature of Polyethylene", Macromolecules **13**, 445–446, ISSN: 15205835 (1980).

[77] S. Fakirov and B. Krasteva, "On the glass transition temperature of polyethylene as revealed by microhardness measurements", Journal of Macromolecular Science - Physics **39**, 297–301, ISSN: 00222348 (2000).

[78] G. T. Davis and R. K. Eby, "Glass transition of polyethylene: Volume relaxation", Journal of Applied Physics **44**, 4274–4281 (1973).

[79] G. Strobl, "Moduli, Viscosities and Susceptibilities", in *Condensed matter physics: crystals, liquids, liquid crystals, and polymers* (Springer Berlin Heidelberg, Berlin, Heidelberg, 2004), pp. 69–126, ISBN: 978-3-642-18558-8.

[80] S. Asare-Asher, J. N. Connor, and R. Sedev, "Elasticity of liquid marbles", Journal of Colloid and Interface Science **449**, 341–346, ISSN: 10957103 (2015).

[81] L. P. B. Guerzoni, J. Bohl, A. Jans, J. C. Rose, J. Koehler, A. J. C. Kuehne, and L. De Laporte, "Microfluidic fabrication of polyethylene glycol microgel capsules with tailored properties for the delivery of biomolecules", Biomater. Sci. **5**, 1549–1557 (2017).

[82] O. J. Cayre, P. F. Noble, and V. N. Paunov, "Fabrication of novel colloidosome microcapsules with gelled aqueous cores", Journal of Materials Chemistry **14**, 3351–3355, ISSN: 0959-9428 (2004).

[83] J. W. O. Salari, J. van Heck, and B. Klumperman, "Steric Stabilization of Pickering Emulsions for the Efficient Synthesis of Polymeric Microcapsules", Langmuir **26**, 14929–14936, ISSN: 0743-7463 (2010).

[84] Y. Yang, Z. Wei, C. Wang, and Z. Tong, "Versatile Fabrication of Nanocomposite Microcapsules with Controlled Shell Thickness and Low Permeability", ACS Applied Materials & Interfaces **5**, 2495–2502, ISSN: 1944-8244 (2013).

[85] J. Zhang, Z. Chen, Z. Wang, W. Zhang, and N. Ming, "Preparation of monodisperse polystyrene spheres in aqueous alcohol system", Materials Letters **57**, 4466–4470, ISSN: 0167577X (2003).

[86] J. van Wijk, T. Heunis, E. Harmzen, L. M. T. Dicks, J. Meuldijk, and B. Klumperman, "Compartmentalization of bacteria in microcapsules", Chem. Commun. **50**, 15427–15430 (2014).

[87] Z. Ao, Z. Yang, J. Wang, G. Zhang, and T. Ngai, "Emulsion-templated liquid core - Polymer shell microcapsule formation", Langmuir **25**, 2572–2574, ISSN: 07437463 (2009).

[88] S. Nudurupati, M. Janjua, N. Aubry, and P. Singh, "Concentrating particles on drop surfaces using external electric fields", ELECTROPHORESIS **29**, 1164–1172 (2008).

[89] R. C. Thompson, "Sources, Distribution, and Fate of Microscopic Plastics in Marine Environments", in *Hazardous chemicals associated with plastics*

in the marine environment, edited by H. Takada and H. K. Karapanagioti (Springer International Publishing, Cham, 2019), pp. 121–133, ISBN: 978-3-319-95568-1.

[90] F. Faure, C. Demars, O. Wieser, M. Kunz, and L. F. de Alencastro, "Plastic pollution in Swiss surface waters: nature and concentrations, interaction with pollutants", Environmental Chemistry **12**, 582, ISSN: 1448-2517 (2015).

[91] T. Mani, P. Blarer, F. R. Storck, M. Pittroff, T. Wernicke, and P. Burkhardt-Holm, "Repeated detection of polystyrene microbeads in the lower Rhine River", Environmental Pollution **245**, 634–641, ISSN: 18736424 (2019).

[92] J. Leung and K. Y. K. Chan, "Microplastics reduced posterior segment regeneration rate of the polychaete Perinereis aibuhitensis", Marine Pollution Bulletin **129**, 782–786, ISSN: 18793363 (2018).

[93] T. R. Gaspar, R. J. Chi, M. W. Parrow, and A. H. Ringwood, "Cellular Bioreactivity of Micro- and Nano-Plastic Particles in Oysters", Frontiers in Marine Science **5**, 345, ISSN: 2296-7745 (2018).

[94] A. J. R. Watts, M. A. Urbina, R. Goodhead, J. Moger, C. Lewis, and T. S. Galloway, "Effect of Microplastic on the Gills of the Shore Crab Carcinus maenas", Environmental Science & Technology **50**, 5364–5369, ISSN: 0013-936X (2016).

[95] K.-W. Lee, W. J. Shim, O. Y. Kwon, and J.-H. Kang, "Size-Dependent Effects of Micro Polystyrene Particles in the Marine Copepod Tigriopus japonicus", Environmental Science & Technology **47**, 11278–11283, ISSN: 0013-936X (2013).

[96] C. Gambardella, S. Morgana, S. Ferrando, M. Bramini, V. Piazza, E. Costa, F. Garaventa, and M. Faimali, "Effects of polystyrene microbeads in marine planktonic crustaceans", Ecotoxicology and Environmental Safety **145**, 250–257, ISSN: 10902414 (2017).

[97] Y. Cong, F. Jin, M. Tian, J. Wang, H. Shi, Y. Wang, and J. Mu, "Ingestion, egestion and post-exposure effects of polystyrene microspheres on marine medaka (Oryzias melastigma)", Chemosphere **228**, 93–100, ISSN: 18791298 (2019).

[98] D. Brennecke, B. Duarte, F. Paiva, I. Caçador, and J. Canning-Clode, "Microplastics as vector for heavy metal contamination from the marine environment", Estuarine, Coastal and Shelf Science **178**, 189–195, ISSN: 02727714 (2016).

[99] P. Dauvergne, "The power of environmental norms: marine plastic pollution and the politics of microbeads", Environmental Politics **27**, 579–597 (2018).

[100] J. A. Ivar Do Sul and M. F. Costa, "The present and future of microplastic pollution in the marine environment", Environmental Pollution **185**, 352–364, ISSN: 02697491 (2014).

Asbjørn Torsvik Kruger

Electrohydrodynamics and particle sintering as methods for production of microporous capsules

NTNU
Norwegian University of
Science and Technology